HIGH FLUX DENSITY ROTATIONAL CORE LOSS MEASUREMENTS

John Gitonga Wanjiku

A Thesis
in
The Department
of
Electrical and Computer Engineering

Presented in Partial Fulfilment of the Requirements
For the Degree of
Doctor of Philosophy (Electrical and Computer Engineering) at
Concordia University
Montréal, Québec, Canada

November 2015

CONCORDIA UNIVERSITY

School of Graduate Studies

This is to certify that the thesis prepared

By: John Gitonga Wanjiku

Entitled: High Flux Density Rotational Core Loss Measurements

and submitted in partial fulfillment of the requirements for the degree of

Doctor of Philosophy (Electrical and Computer Engineering)

complies with the regulation of the University and meets the accepted standards with respect to originality and quality.

Signed by the final Examining Committee:

______________________________ Chair

Dr. Radu Zmeureanu

______________________________ External Examiner

Dr. Joseph O. Ojo

______________________________ Examiner

Dr. Christopher W. Trueman

______________________________ Examiner

Dr. Luiz A. C. Lopes

______________________________ Examiner

Dr. Rama B. Bhat

______________________________ Supervisor

Dr. Pragasen Pillay

Approved by ____

Chair of Department or Graduate Program Director

__________2015 ______________________________

Dean of Faculty

Abstract

Energy conversion processes involve losses. Specifically core losses, which are a result of the magnetization process in cored electrical energy conversion and storage devices. The cores are made of soft ferromagnetic materials that are easily magnetized and demagnetized. These soft magnetic cores, allow a reduction in size, higher energy storage density, and a reduction in magnetizing current, when compared to non-cored devices.

The characterization of soft ferromagnetic materials is traditionally done under unidirectional pulsating fields, which is sufficient for single-phase transformers and inductors, where the cores are under pulsating fields. However, T-joints of three phase transformers and teeth-roots of rotating machine stator cores are exposed to two-dimensional rotational fields of higher core loss. Pulsating measurements are therefore insufficient in the characterization of soft ferromagnetic materials used in rotating electrical machines or in three phase transformers. In two-dimensional fields, the magnetization direction changes with time, tracing a flux density locus. This requires the measurement of tangential magnetic field and flux density components, hence the associated loss.

This study proposes a two-dimensional rotational core loss tester for high flux density measurements up to about 2 T, at 60 Hz. Its frequency measurement range is from 60 Hz to 1 kHz. The initial sizing was done analytically, then implemented in three-dimensional finite element analysis, prototyped and experiments performed to verify its capability.

It was validated by testing two 0.35 mm and 0.65 mm thick samples. Very high flux densities in the range of 2 T at 60 Hz were achieved in both samples. For the thinner sample, flux densities of 1.8 T and 1.6 T were measured at 400 Hz and 1 kHz, respectively, while for the thicker one, the range reduced to 1.7 T and 1.4 T, at 400 Hz and 1 kHz, respectively. The magnetizer also reproduced non-sinusoidal flux density waveforms, for flux densities less than or equal to 1.0 T, without any waveform control.

The proposed rotational core loss setup will find application in the characterization of electrical steels, and generation of pulsating and rotational core loss data. This data can then be applied in core loss models, uprating of megawatt (MW) rated machines, transient and hotspots analysis, and in the design of higher power density machines, such as high-speed machines.

To my Uncle, Henry Ndiritu Wambugu

Acknowledgement

I thank the Almighty God for granting me good health this far. Am grateful to uncle Ndiritu and the memories of my mum, for their support, selflessness and kindness. I am indebted to the Kirichus, for providing a warm and hospitable home, far from home.

My sincere appreciation goes to my supervisor Prof. Pillay for his assistance and guidance throughout the process of this program. I cannot forget Dr. Natheer, Dr. Maged, Mr. Chirag, and Mr. Woods (Joe), for their assistance in the laboratory. Am also grateful to GMW Associates Inc. for donating the Hall sensors, which were invaluable in the local magnetic field measurements.

I recognize the sacrifice of Jemimah and Florence in finding time to go through each chapter of this thesis. Special thanks to Florence; were it not for you, skiing would still be a mystery.

I am grateful to mes amis, and the entire PEER family; Lesedi for being more than a brother, Kang Chang for his friendship, Sara and Nazli for the nuts, and Amir, Hussein, Masadeh, Akrem for the cookies, and Abhijit, Rajendra, Maninder; for the fun times in Montréal.

Am also grateful to my friends Jesse, Wambugu Wangui, Wambugu Maina, Muhia, Hezi, Roba, Waire, Mwenda, Olang', Lisa and Karanja Kabini.

Finally, I am thankful to NSERC-Canada, Hydro-Québec, ENCS and School of Graduate Studies, Concordia University, for their financial support.

Table of Contents

Abstract iii
Acknowledgement v
Table of Contents iv
List of Tables vii
List of Figures viii
List of Abbreviations xii
List of Symbols xvi
Chapter 1. Introduction 1
  1.1 Pulsating and Rotating Magnetization 5
  1.2 Problem Statement 10
  1.3 Motivation 11
  1.4 Review of Rotational Core Loss Measurements 12
    1.4.1 Measurement Methods 12
    1.4.2 Measurement Setups and Sample Shapes 14
    1.4.3 Measurement of the Magnetic Field 16
    1.4.4 Measurement of the Flux Density 19
    1.4.5 Standards and Comparison of Rotational Core Loss Measurements 22
  1.5 Objective 23
  1.6 Methodology 23
  1.7 Contribution 25
  1.8 Limitation 26
  1.9 Thesis Organisation 26
  1.10 Conclusion 27
Chapter 2. Design Considerations of Rotational Magnetizers for High Flux Density Measurements 28
  2.1 Numerical Analysis Methodology 30
  2.2 Square Magnetizer (SSST) 33
  2.3 Halbach Magnetizers (HaRSST) 34
    2.3.1 Number of Poles 35
    2.3.2 Sample Diameter 36
  2.4 Induction Machine Stator Yoke Magnetizers (IMRSST) 37
    2.4.1 Conventionally Wound-IMRSST (CW-IMRSST) 37
    2.4.2 Sinusoidally Wound-IMRSST (SW-IMRSST) 37
  2.5 Analysis of Numerical Results 39
    2.5.1 Flux Density Variation with Magnetization Direction 40

2.5.2 Impact of a Deep Yoke on the Flux Density Variation 44
2.6 The Proposed Rotational Magnetizer..46
2.7 Conclusion 49
Chapter 3. Instrumentation 51
3.1 Measurement of Flux Density...52
3.1.1 Location of B-Coils 52
3.1.2 Size of the B-holes...55
3.1.3 Sample Anisotropy 57
3.1.4 Length of B-coils 59
3.2 Measurement of Magnetic Field 61
3.2.1 H-coil Calibration...61
3.2.2 Size of H-coils 65
3.2.3 Location of H-coils...66
3.3 Comparison of Magnetizers in Core Loss Measurements 70
3.4 Conclusion 72
Chapter 4. Mitigation of the Magnetic Field Z-component...73
4.1 Numerical Analysis Methodology 76
4.2 Numerical Analysis of the Magnetic Field Z-component..76
4.2.1 Shielding Distance...77
4.2.2 Impact of Magnetizer Size and Yoke Depth on H_z...81
4.3 Experimental Analysis of the Magnetic Field Z-component 82
4.4 Contribution of Magnetic Properties to the Magnetic Field Z-component 84
4.5 Conclusion 87
Chapter 5. Core Loss Measurement Analysis..88
5.1 Measurement Methodology 89
5.2 Core Losses under Sinusoidal Excitation...90
5.3 Core Losses under Non-sinusoidal Excitation 95
5.4 Conclusion 96
Chapter 6. Measurement Errors and Uncertainty Analysis 97
6.1 Classification of Measurement Errors...97
6.2 Review of Uncertainty Estimation Methods 99
6.3 Quantifying Measurement Errors and Uncertainty 101
6.3.1 Absolute Constant Systematic Errors 103
6.3.2 Conditionally Constant Systematic Errors...103
6.3.3 Overall Random Error 105
6.3.4 Total Uncertainty...106
6.4 Estimation and Correction of Elementary Errors 107

6.4.1 Sampling Frequency Error 107
6.4.2 Number of Averaging Cycles Error 109
6.4.3 Analogue to Digital Converter (ADC) Error 110
6.4.4 Magnetic Field Measurement Errors 111
6.4.5 Flux Density Measurement Errors 118
6.4.6 Overall Random Error 123
6.5 Measurement Error Results Analysis 124
6.5.1 Absolute Constant Systematic Errors 124
6.5.2 Conditionally Constant Systematic Errors 126
6.5.3 Overall Random Error 127
6.5.4 Total Uncertainty 127
6.6 Conclusion 128
Chapter 7. Conclusion and Future Work 130
References 135

List of Tables

Table 1.1 A summary of the reviewed core loss measurement methods 21

Table 2.1 Parameters of the four rotational magnetizer topologies 39

Table 2.2 Variation of $|H_p|$ due to changes in $|B_p|$, and the impact of the yoke depth on uniformity .. 44

Table 3.1 Verification of the Hall sensors using Helmholtz coils, at 60 Hz 63

Table 3.2 Calibration of H-coils, at 60 Hz 64

Table 3.3 Airflux magnetic fields under pulsating measurements, at 60 Hz 68

Table 3.4 Phase difference under pulsating measurements, at 60 Hz 69

Table 4.1 Summary of numerical H_z, at 60 Hz 86

Table 4.2 Summary of experimental H_z, at 60 Hz 86

Table 5.1 Parameters of the two non-oriented electrical steels 90

Table 5.2 Measured core losses, at 1.0 T 93

Table 5.3 Non-sinusoidal measured core losses, at 60 Hz 95

Table 6.1 The impact of averaging and sampling frequency on the core losses, at 60 Hz 110

Table 6.2 The error limits of dSPACE ADCs used in data acquisition [102] 110

Table 6.3 Sample, H-coil and airflux peak fields, under pulsating measurements, at 60 Hz 112

List of Figures

Fig. 1.1 Typical distribution of induction machine losses (adapted from [1])....................................1

Fig. 1.2 A solenoid of N_m turns, carrying i_m current 2

Fig. 1.3 B-H curve and hysteresis loop 3

Fig. 1.4 B-loci at the tooth, tooth-root, back of the slot and back yoke, of a 19 MVA hydro generator [8]..6

Fig. 1.5 T-joint of a 3-phase transformer [20] 6

Fig. 1.6 Categorization of B-loci into pulsating, elliptical and rotating...7

Fig. 1.7 Distribution of pulsating and rotational zones in a 19 MVA hydro generator [8]..................7

Fig. 1.8 Domain configurations during magnetization (adapted from [5])..8

Fig. 1.9 Pulsating and rotating hysteresis loss 9

Fig. 1.10 Cross and strip samples 14

Fig. 1.11 Square, hexagonal and 3-D single sheet testers...15

Fig. 1.12 Round single sheet testers..16

Fig. 1.13 Hall element positioned to measure the magnetic field H...18

Fig. 1.14 Rogowski-Chattock coil 18

Fig. 1.15 Inductive H-coils 19

Fig. 1.16 Inductive B-coils and B-tips 20

Fig. 1.17 Surface B-H sensing system [38], [53] 20

Fig. 1.18 Magnetizer design procedure...24

Fig. 2.1 The analysed four rotational magnetizer topologies...29

Fig. 2.2 Meshing of a 3-D model..31

Fig. 2.3 Locations of lines for measuring H_z, H_y and B_y for numerical analysis, and Hall sensors for experimental measurements of H_z, and the non-uniform distribution of $|B|$ in tesla [T] 32

Fig. 2.4 Schematic of a quarter of a 12 pole Halbach magnetizer 34

Fig. 2.5 Effect of the number of poles on flux density and uniformity, for HaRSSTs 35

Fig. 2.6 Effect of sample diameter on flux density and uniformity, for HaRSSTs............................36

Fig. 2.7 Distribution of turns in slots 38

Fig. 2.8 Half of the winding diagrams 39

Fig. 2.9 MMF waveforms at different instantaneous currents, at 60 Hz and $I_{mx} = I_{my} = 1$ A.............39

Fig. 2.10 Variation in $|B|$ patterns in tesla [T] of the four models at 0 º (y-axis) and 45 º magnetization directions as indicated by the arrows 40

Fig. 2.11 Distribution of $|B|$ and eddy-currents in the SW-IMRSST, at 0 º (y-axis) magnetization direction 41

Fig. 2.12 Variation of the instantaneous $|B_p|$ with magnetization directions 42

Fig. 2.13 Variation in $|B_p|$ uniformity and average $|B_p|$ with change in magnetization direction 43

Fig. 2.14 Improvement of uniformity and magnetic loading with increasing yoke depth 45

Fig. 2.15 Increasing H range by varying the number of turns and sample/magnetizer size 47

Fig. 2.16 The proposed 24-slot-SW-IMRSST magnetizer 47

Fig. 2.17 Experimental validation of the proposed rotational magnetizer 48

Fig. 2.18 Circularity of B-loci with respect to the B-coil locations 49

Fig. 3.1 The possible locations of B-coils on a square sample 52

Fig. 3.2 Numerical results on the effect of the location of the B-coils, and the type of magnetizer, on B-loci 53

Fig. 3.3 B-coils wound on samples for analysing the effect of B-coil location 54

Fig. 3.4 Experimental results based on the type and location of B-coils, at 60 Hz 54

Fig. 3.5 Distribution of $|B|$ in tesla [T] around a B-hole 55

Fig. 3.6 Local increase in B and H caused by a B-hole 56

Fig. 3.7 Decrease in H_y deviation from the sample surface 56

Fig. 3.8 Increasing non-uniformity with the introduction of B-holes and sample anisotropy, in a square sample of an SSST 58

Fig. 3.9 Increasing non-uniformity with the introduction of B-holes and sample anisotropy, in a round sample of a sinusoidally wound-IMRSST 58

Fig. 3.10 Numerical results on the effect of anisotropy on the circularity of B-loci, and B waveforms 58

Fig. 3.11 Analysed B-coil lengths 59

Fig. 3.12 Effect of B-coil lengths on the measured core losses, at 60 Hz 60

Fig. 3.13 B-coil voltages at 0.5 T and 60 Hz 60

Fig. 3.14 The Helmholtz coils setup used to verify Hall sensors and calibrate H-coils 62

Fig. 3.15 Helmholtz coils field map generated at 0.5 A and 60 Hz 63

Fig. 3.16 Two H-coil sizes of 30 mm by 30 mm by 1.4 mm of 180 turns, and 53 mm by 44 mm by 1.6 mm of 220 turns 65

Fig. 3.17 Pulsating ($r = 0$) and rotating ($r = 1$) experimental core losses, at 60 Hz 65

Fig. 3.18 The location of H-coil with respect to B-coil and the sample, and the associated fields 66

Fig. 3.19 Hall sensor locations for measuring the tangential component of the air flux, H_x 67

Fig. 3.20 Measured airflux leakage field above the sample of the SW-IMRSST with a 10 mm yoke depth, under pulsating magnetizations, at 60 Hz 67

Fig. 3.21 Pulsating core losses at different Hall sensor locations above the sample, at 60 Hz...........69

Fig. 3.22 Magnetizers used in the analysis of the z-component and airflux leakage fields, and in the comparison of pulsating and rotating core losses, at 60 Hz 70

Fig. 3.23 Measured core losses using the three magnetizers 71

Fig. 3.24 Counter-clockwise H-loci under rotating fields, at 60 Hz 71

Fig. 4.1 Numerical H_z at the boundary of the sample and the air, at 0.54 T and 60 Hz, under rotating flux, for the unshielded SW-IMRSST 74

Fig. 4.2 Location of the shields, sample and H-coils...74

Fig. 4.3 Numerical H_z of the four models, at 10 A and 60 Hz 76

Fig. 4.4 The impact of the yoke depth on numerical H_z, at 10 A and 60 Hz 77

Fig. 4.5 Numerical H_z at different shield distances, at 60 Hz 78

Fig. 4.6 Half section numerical distribution of H_z, at 60 Hz...79

Fig. 4.7 Instantaneous numerical H_y at different shield distances, at 60 Hz 80

Fig. 4.8 Instantaneous numerical B_y at different shield distances, at 60 Hz 81

Fig. 4.9 Impact of diametrical size and yoke depth on numerical H_z, at 60 Hz.................................82

Fig. 4.10 Location of Hall sensors for measuring H_z 82

Fig. 4.11 Induced H_z by stray fields at 0.5 T, 1.5 T and 2.0 T, at 60 Hz 83

Fig. 4.12 Experimental H_z, at 60 Hz 83

Fig. 4.13 Experimental H_z of the 200 mm sample HaRSST magnetizer, at 60 Hz............................85

Fig. 5.1 Schematic of the rotational core loss measurement system...89

Fig. 5.2 The developed rotational core loss measurement test bench at Concordia University power engineering laboratory 89

Fig. 5.3 Measured core losses at 60 Hz..91

Fig. 5.4 Measured core losses at 400 Hz...92

Fig. 5.5 Measured core losses at 1 kHz..92

Fig. 5.6 Core loss ratios with respect to the pulsating core loss, at 1.0 T 93

Fig. 5.7 Measured aspect-ratios and form-factors of the M19G29 sample, at 60 Hz 94

Fig. 5.8 Measured and numerical B-loci, at 60 Hz 95

Fig. 6.1 Effect of sampling frequency on B-H curves and pulsating losses, at 60 Hz 108

Fig. 6.2 Effect of sampling frequency on pulsating core losses, at 1.8 T and 60 Hz 108

Fig. 6.3 Reconstructed magnetic fields at 0.2 T and 60 Hz 113

Fig. 6.4 Decomposition of H and B vectors, with angular misalignment in H-coils 114

Fig. 6.5 Measured noise under rotating fields, at 60 Hz 117

Fig. 6.6 B-coil arrangement showing the enclosed air by the B_y-coil (not drawn to scale) 120

Fig. 6.7 Angular misalignment of B-coils caused by B-holes (not drawn to scale) 121

Fig. 6.8 CW and CCW rotating core losses for 10 runs, at 60 Hz 124

Fig. 6.9 Averaging of CW and CCW core losses with error bars for 10 runs, at 60 Hz 124

Fig. 6.10 Absolute constant systematic errors for B and H arguments, at 60 Hz 125

Fig. 6.11 Conditionally constant systematic errors for B and H arguments, at 60 Hz 126

Fig. 6.12 Overall random error, at 60 Hz 127

Fig. 6.13 Absolute, combined and total uncertainty for rotational core losses, at 60 Hz 128

List of Abbreviations

2-D	Two-dimension
3-D	Three-dimension
a	Radius of a solenoid
$abs\_dev\ (x)$	Average absolute deviation
$A_{B,H}$	Enclosed area of the B and H-coils, respectively
A_{core}	Cross-sectional area of a transformer core
ADC	Analogue to digital converter
AC	Alternating Current – represents alternating quantities
ASTM	American society for testing materials
A_{turns}	Amplitude of the winding functions
B	Flux density
$\widetilde{B}_{x,y}$	Estimated flux densities by measurements
B_g	Airgap flux density
B_k	Flux density at the knee point
$B_{\max}$	Maximum radius of a B-locus
$B_{\min}$	Minimum radius of a B-locus
$B_{n,p}$	Normal and parallel flux densities with respect to the magnetization direction
B_{peak}	Peak flux density in a transformer core
$B_{px,py}$	Tangential peak flux densities
B_s	Saturated flux density
$B_{x,y,z}$	Flux densities in the x, y and z directions
$B_{x,y_{CW,CCW}}$	Tangential flux density components in the CW and CCW directions
CCW	Counter-Clockwise
C_p	Specific heat
cP_i	Center of the i^{th} pole of a Halbach ring
CW	Clockwise
CW-IMRSST	Conventionally wound induction machine round single sheet tester
d	Shield distance
d_h	Diameter of a B-hole
DC	Direct Current – represents constant quantities
$dev\ (x)$	Deviation of the maximum from the minimum, with respect to the average
D_g	Airgap diameter
d_y	Yoke depth
$e_{B,H,R}$	Induced output voltages of the sensors

f	Frequency
FEA	Finite Element Analysis
F_F	B-coil voltage form-factor
F_s	Sampling frequency
FSV	Full scale voltage
F_m	Torquemetric force
g	Airgap length
g_{int}	Interpolar clearance
g_t	Sample thickness
GUM	Guide to the Expression of Uncertainty in Measurement
GOS	Grain-oriented electrical steel
H	Magnetic field
H1,2,3,4,5	Hall sensor magnetic fields
H_a	Applied or external magnetic field
$H_{airflux}$	Airflux leakage magnetic field
H_{af}	Peak of the airflux leakage magnetic field
$H_{analy}.$	Analytical magnetic field at the center of the Helmholtz coils setup
$Hall_{1,2,3,4,5}$	Hall sensor magnetic fields
HaRSST	Halbach Round Single Sheet Tester
H_{coil}	H-coil magnetic field
H_c	Peak H-coil magnetic field
H_{demag}	Sample demagnetizing magnetic field
H_{FEA}	Numerical magnetic field for calibrating H-coils
HGOS	Highly grain-oriented electrical steels
$H_{measured}$	Measured magnetic field
H_k	Magnetic field at the knee point
$H_{n,p}$	Normal and parallel magnetic fields with respect to the magnetization direction
H_{sample}	Sample magnetic field
H_s	Peak sample magnetic field
$H_{sensors}$	Sensor magnetic field
HSST	Hexagonal Single Sheet Tester
$\widetilde{H}_{x,y}$	Estimated magnetic field by measurements
$H_{x,y,z}$	Magnetic fields in the x, y and z directions
$H'_{x,y_{CW,CCW}}$	Measured H components in the CW and CCW directions
Hz	Hertz; a SI unit for frequency
$H_{z\text{-max}}$	Maximum magnetic field z-component

$I_{B,H}$	Influence coefficient
I_H	Hall current
i_m	Magnetizing current
IMSST	Induction Machine Single Sheet Tester
$I_{mx,my}$	Peak x and y phase magnetizing currents
$K_{B,H,R}$	Sensor constant, or sensitivity
k_{cal}	Calibration constant
k_{hall}	Hall sensor calibration factor
$k_{h,e,ex}$	Hysteresis, eddy-current and excess core loss coefficient
kHz	Kilo Hertz
l_B	B-coil length
$L_{ac,B,eqn,H,Haf,j}$	Limits of the absolute systematic errors
L_e	Effective axial length
l_m	Length of a solenoid, or magnetic path length
L_s	Inductance
m	Number of cycles
M	Intrinsic magnetization
MCM	Monte Carlo method
MMF	Magneto motive force
M_s	Saturated intrinsic magnetization
MW	Megawatt
n	Number of repeated measurements
N	Input arguments
$N_{B,H}$	Number of turns for the B and H-coils, respectively
N_{coil}	Number of turns of a Helmholtz coil
N_m	Number of turns
NOS	Non-oriented electrical steel
N_s	Number of cycles
$N_{t\max}$	Maximum number of turns per slot
$N_{x,y}$	Turns per slot for the x and y-phases
P	Core loss (both pulsating and rotational); true core loss
$\widetilde{P}$	Estimated core loss by measurements
$\overline{P}$	Estimated mean core loss by measurements
PCM	Polynomial chaos method
PDF	Probability density function
P_e	Electrical power of a rotating conventional machine
$P_{H1, H2, H3, H4, H5}$	Core losses derived from five Hall sensor locations above the sample surface

P_{rot}	Rotational core loss
PUMA	Procedure for uncertainty management
$\overline{P}'_{x,y}$	Average core loss in the *x* and *y* directions
$P'_{x,y_{CW,CCW}}$	Measured core loss components in the CW and CCW directions
R	Radius of the Helmholtz coils
r	Aspect-ratio
RFVs	Random fuzzy variables
RD	Rolling Direction
r_i	Inner radius of the Halbach ring
r_{pcd}	Radius to the center of a Halbach pole, from the center of the Halbach ring
r_p	Halbach pole radius
rms	Root mean square
r_s	Sample radius
$S_{c,\upsilon,r}$	Combined, conditionally constant and random error standard deviation
SNR	Signal to noise ratio
SMC	Soft magnetic composites
SSST	Square Single Sheet Tester
SW-IMRSST	Sinusoidally wound induction machine round single sheet tester
T	Temperature of the sample; periodic time
TD	Transverse Direction
T_m	Torquemetric torque
$u_{c,t}$	Combined and total uncertainty
v_H	Output voltage of the Hall sensor
$v_{x,y}$	The *x* and *y* phase control and power signals
V_{vol}	Volume
W	Energy stored by an inductor
$z_{1,2,3}$	Helmholtz coil parameters

List of Symbols

μ_0	H/m	Permeability of free space
μ_r		Relative permeability
α		A hysteresis core loss coefficient; angle (radians) between Halbach poles
α		Probability confidence level
β_i	radians	Magnetization direction of the i^{th} Halbach pole with respect to the y-axis
γ		A coefficient used in fitting pulsating data to match rotational core loss data
$\delta_{x,y}$	degrees	Misalignment angles in the x and y directions respectively
δ_H	degrees	Misalignment angle caused by the location of B-coils
θ_α		Limits of the conditionally constant error
θ_s	degrees	Slot angle
ρ	kg/m^3	Density
σ	S/m	Conductivity; standard deviation
ϕ_H	degrees	Fundamental phase of the Hall sensors
ϕ_s	degrees	Fundamental phase of the sample magnetic field
$\phi_{x,y}$	radians	Loss angle between the B and H tangential component
$\mathit{\Delta}$		Absolute error
ε		Relative error
$\upsilon_{add,cc,j}$		Additional and conditionally constant systematic errors
ψ_j		Random error

Chapter 1. Introduction

Soft iron cored energy conversion devices such as transformers and rotating electrical machines, transform electrical energy to more useable forms of electrical or mechanical energy. Soft magnetic materials are easily magnetized and demagnetized, using a magnetizing current that is significantly lower than the load current. The energy conversion process is reversible and involves device dependent losses, which include conductor, friction, windage, vibrations, acoustic, core and stray load losses. Conductor losses depend on the conductor dimensions, temperature and frequency, while friction and windage losses depend on the machine rotor surface, rotational speed and type of bearings. Unbalanced magnetic and mechanical forces and the control scheme results in vibrations and acoustic noise. Core losses arise from the magnetization process of soft magnetic materials, while stray load losses are the remainder of the unaccounted losses.

The typical loss distribution (see Fig. 1.1) of induction machines, which are widely used in many applications owing to their ruggedness, is 25 - 40 % stator conductor losses, 15 - 25 % rotor conductor losses, 15 - 25 % core losses, 5 - 15 % friction and windage losses and 10 - 20 % stray load losses [1]. Therefore, core losses are a significant portion of the total loss. Moreover, they are among the highest in large MW rated machines, which use a large amount of electrical steels [2]. For instance, it is 45 % of the total loss in large synchronous motors used in cement and mining mills [3].

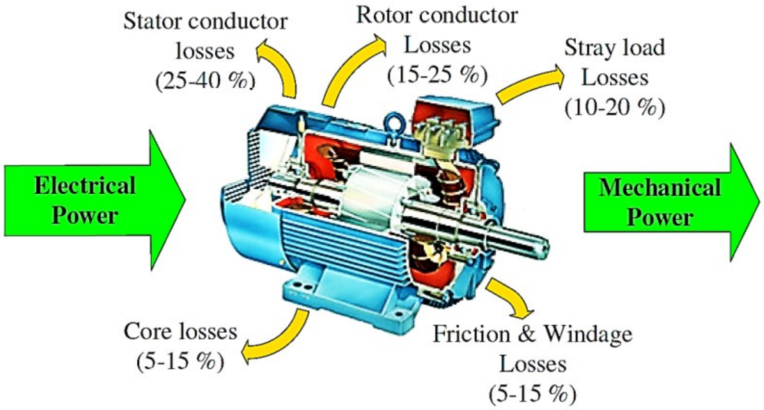

Fig. 1.1 Typical distribution of induction machine losses (adapted from [1])

One way of improving the energy conversion efficiency is by reducing the individual loss components. The emphasis of this study is on the development of a measurement tool for measuring core losses of electrical steels used in rotating electrical machine cores. The measured core loss data can then be used in the core selection for a specific application, resulting in more efficient use of the core material at a lower loss, hence improving the overall efficiency and sustainability.

Core losses are frequency and flux density dependent. As a result, they are important in the design of electrical machines for high frequency and high power density applications, such as in the aerospace and defence industries, where the operating frequency is in the range of 400 Hz to 1.5 kHz [4]. Other applications requiring high power density and variable operating points are in transportation applications, such as electric vehicles.

Soft magnetic materials results in a size reduction of energy conversion devices. This can be explained by use of the solenoid shown in Fig. 1.2 of N_m turns carrying a current i_m.

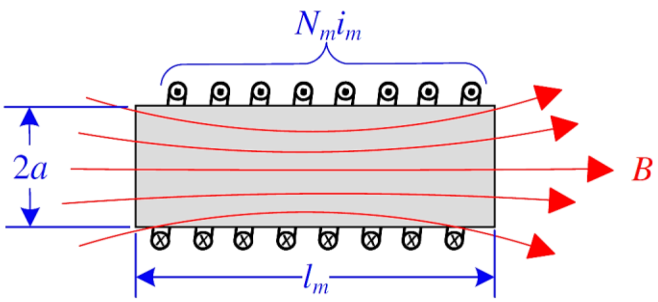

Fig. 1.2 A solenoid of N_m turns, carrying i_m current

The core has a radius a, length l_m and its relative permeability is μ_r. For a long solenoid ($l_m \gg a$), the axial magnetic flux density (B) is [5]:

$$B = \mu_r \mu_0 \frac{N_m i_m}{l_m}, \tag{1}$$

where μ_0 is the permeability of free space. The energy stored (W) by the solenoid is also proportional to the relative permeability through the inductance, L_s as:

$$W = \frac{1}{2} L_s i_m^2, \tag{2}$$

where,

$$L_s = \frac{N_m B \pi a^2}{l_m} = \mu_r \mu_0 \pi a^2 \frac{N_m}{l_m}. \tag{3}$$

These relationships show that in the design of energy conversion devices, the choice of the core material will affect their size and the magnetizing current (i_m) needed to set up the working field. To achieve the same flux density for non-magnetic core materials ($\mu_r = 1$), the number of turns and currents have to be increased, while the high relative permeability ($\mu_r \gg 1$) of the ferromagnetic core, allow a reduction of the device size. Consequently, significantly lower magnetizing currents establish the same flux density, at lower conductor losses.

The selection of a core material for a particular application is based on the *B-H* curve, which is illustrated in Fig. 1.3. The magnetic field (H) is proportional to the magnetizing current. The operating point of the core is usually selected below the knee of the curve (H_k, B_k), which is shown in Fig. 1.3. Any increase in B beyond the knee towards saturation (B_s) requires very high magnetizing currents. This is the case of transformers where the back-EMF (E) equation is proportional to the cross-sectional area of the core (A_{core}) and peak flux density ($B_{peak} \approx B_k$) as:

$$E = 4.44 \cdot f \cdot N \cdot A_{core} \cdot B_{peak}. \tag{4}$$

The slope of the *B-H* curve at the operating point gives the operating permeability of the core.

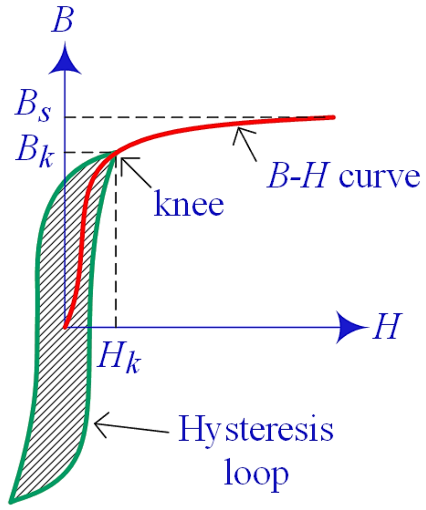

Fig. 1.3 *B-H* curve and hysteresis loop

After determining the operating point of the core, equivalent magnetic circuits are then used to size the components and determine other parameters such as the airgap flux density (B_g), based on the power requirements. The power (P_e) of a rotating conventional electrical machine is related to the core material via B_g and frequency f as:

$$P_e \,\alpha\, B_g \cdot f \cdot D_g^2 \cdot L_e, \tag{5}$$

where D_g is the airgap diameter, and torque is produced over the effective length, L_e of the machine.

B-H curves are derived from the peak of the hysteresis loops such as the one shown in Fig. 1.3, by applying a sinusoidal magnetic field of variable amplitude to the test sample. The area enclosed by the hysteresis loop gives the core loss. The cyclic field also induces eddy-currents in the core that oppose the applied field, resulting in the eddy-current core loss component that is reduced by laminating the core. Therefore, the total core loss (P) is [5], [6]:

$$P = k_h f B^{1.6} + k_e f^2 B^2, \tag{6}$$

which is the classical core loss equation, where k_h and k_e are hysteresis and eddy-current coefficients. The hysteresis term was proposed by Steinmetz and is valid for a maximum flux density range of 1.0 T, at low frequencies of less than or equal to 60 Hz [5], [6].

The classical core loss equation is often modified to extend its validity to higher flux densities and frequencies. In [7], an excess loss term is proposed to account for the difference between the classical and the measured core losses such that:

$$P = k_h f B^{\alpha} + k_e f^2 B^2 + k_{ex} f^{3/2} B^{3/2}, \tag{7}$$

where α is obtained from loss separation, and k_{ex} is the excess loss coefficient. This model is based on the assumption of a uniform field for thin laminations and low frequencies where skin effect is negligible. Therefore, by incorporating skin effect in the determination of eddy-current losses, the total core loss retains the form of the classical equation [6].

Variations to these two models have been proposed based on loss separation and curve fitting determination of the coefficients as functions of flux density and frequency [8]. The models are extensively used because of their low computational time and simplicity when compared to other physics and mathematical based methods, such as Jiles-Atherton, energetic and vector Preisach models [9], [10], [11], [12].

In most cases, rotational core losses (P_{rot}) are accounted for by use of the aspect-ratio (r) and additional factors in modifying pulsating data, as done in [13] and [14], such that:

$$P_{rot} = r\gamma\left(k_h f B^{\alpha} + k_e f^2 B^2 + k_{ex} f^{3/2} B^{3/2}\right), \qquad (8)$$

where γ is factor that depends on flux density and core material. In other cases, it is assumed that the core losses under rotational fields are the summation of the pulsating losses in the two directions [15]. In [16], a model that interpolates for the aspect-ratios between pulsating and purely rotational fields is suggested, while in [17], a rotational core loss diffusion model that accounts for skin effect, and uses the classical core loss separation method to determine the complex permeability, is validated.

The previous analysis shows that the core material affects the size of the energy conversion device, while the associated core loss depends on the operating frequency and flux density. Hence, for aerospace and defence applications where size, weight, safety and service life are critical, the core is of higher saturation, permeability and low loss, such as iron-cobalt alloys [18], [19]. These alloys can reach very high flux densities at high frequencies, for example 2.1 T at 5 kHz [17]. However, for general purpose applications, electrical silicon steels are widely used.

1.1 Pulsating and Rotating Magnetization

Soft magnetic materials are characterized by placing them in a magnetic field, where characteristics such as relative permeability and core losses are determined at a specific frequency and flux density. Magnetizer or testers are either pulsating or rotational. Pulsating magnetizers (Epstein frame, single sheet and toroid testers) generate unidirectional pulsating fields, similar to a transformer, and the sample is or forms part of the core. The magnetic field and flux density are then derived from the magnetizing current and the induced open circuit voltage of the secondary. The core loss is then determined by the wattmeter method, or from the B-H loop area.

In pulsating measurements, the direction of the B-vector is constant, but its magnitude is time varying. In rotating two-dimensional measurements, its magnitude remains constant, while its direction changes with time. Practical flux density loci are not purely pulsating or purely rotating, but are within these extremes. This is illustrated in Fig. 1.4, which shows the B-loci at the tooth, tooth-root, back of the slot, and back yoke of a 19 MVA hydro generator [8]. The figure also shows that the B-waveforms are nonsinusoidal.

Therefore, pulsating measurements may be sufficient for single-phase transformers and inductors, where the core is exposed to pulsating fields. Rotational two-dimensional fields exist in the teeth-roots of rotating electrical machines, and T-joints of three phase transformer cores as shown in Fig. 1.4 and Fig. 1.5, respectively. Furthermore, their flux density waveforms are non-sinusoidal, and may even contain DC components. This makes pulsating magnetization insufficient in the study of core losses under real machine operating conditions.

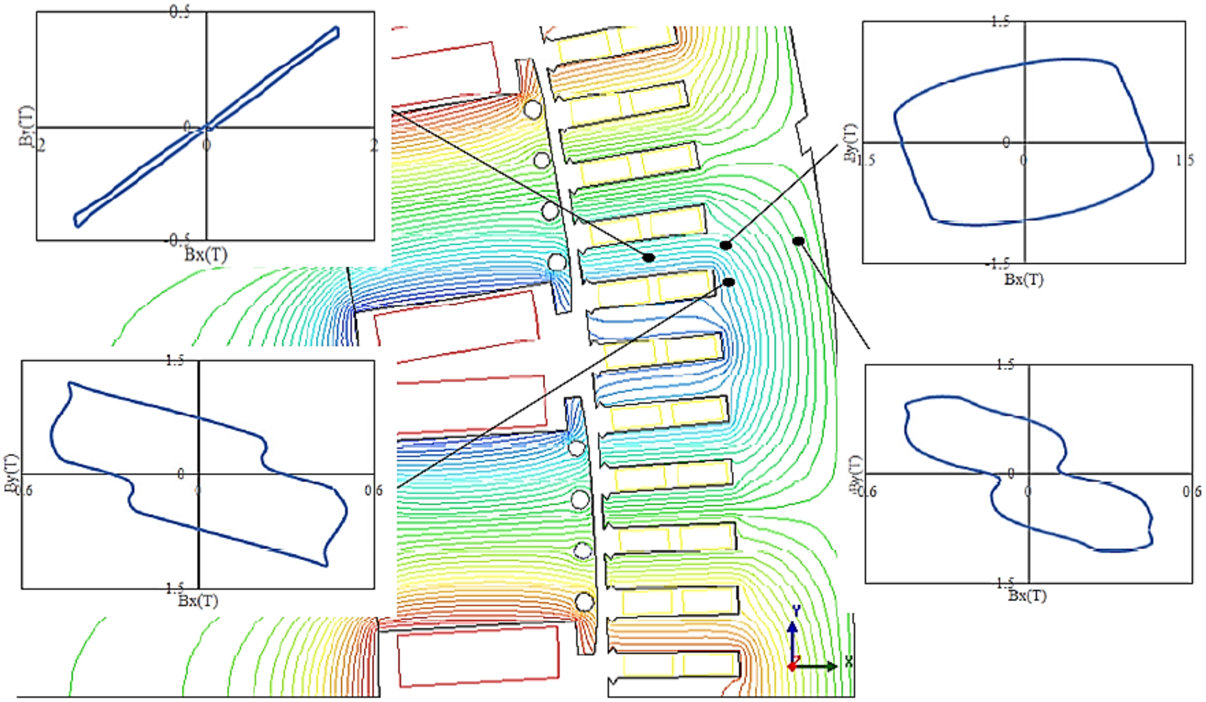

Fig. 1.4 *B*-loci at the tooth, tooth-root, back of the slot and back yoke, of a 19 MVA hydro generator [8]

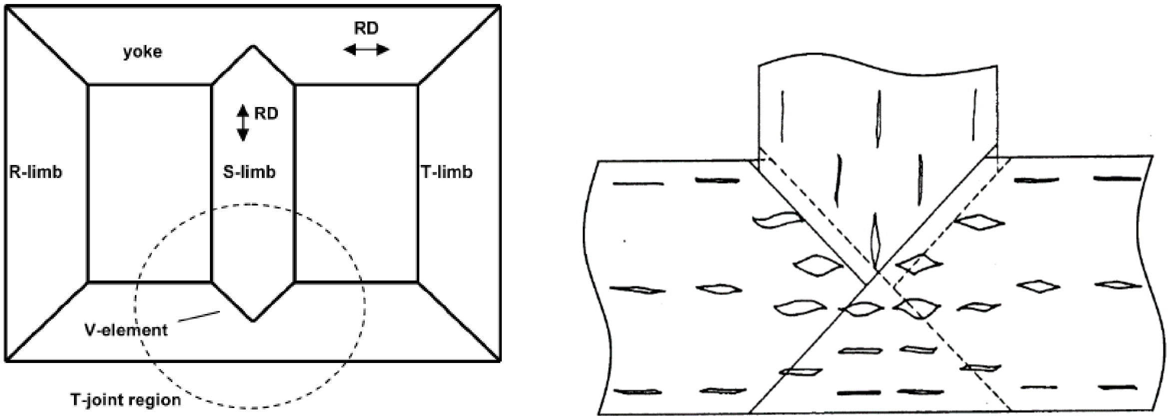

Fig. 1.5 T-joint of a 3-phase transformer [20]

An aspect-ratio of the minimum to maximum radii of a B-locus, i.e. $r = B_{\min} / B_{\max}$ categorizes a B-locus into pulsating ($r = 0$), elliptical ($0 < r < 1$) or rotating ($r = 1$) as depicted in Fig. 1.6. In this study, aspect-ratios greater than zero ($r > 0$) are referred to as rotational.

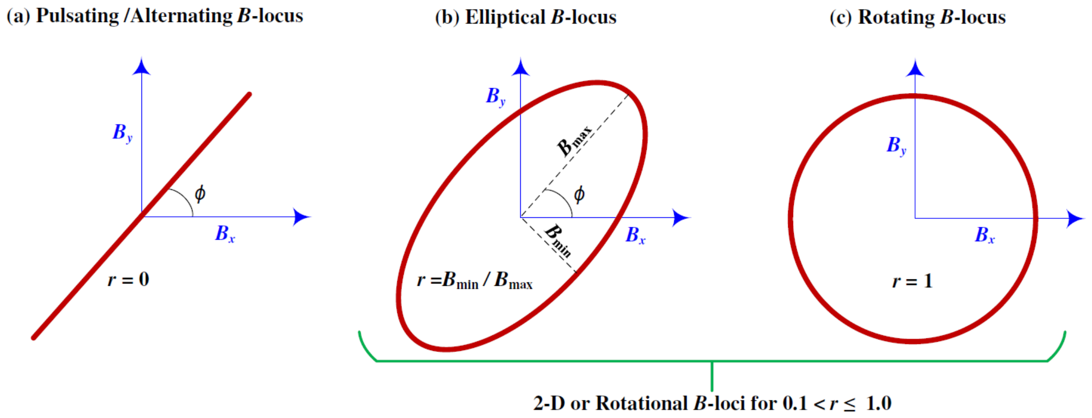

Fig. 1.6 Categorization of *B*-loci into pulsating, elliptical and rotating

This ratio maps the distribution of pulsating and rotational fields in a stator core as shown in Fig. 1.7 (a) for the 19 MVA hydro generator of Fig. 1.4. As seen in Fig. 1.7 (b), rotational flux represents over 50 % of the total flux in a typical machine stator core, hence the need for two-dimensional rotational testers.

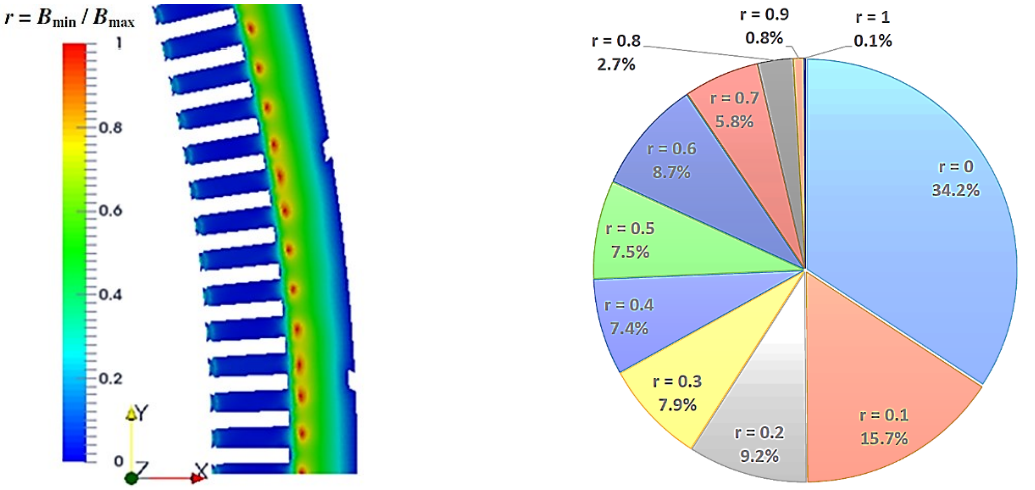

(a) Aspect-ratio map **(b) Aspect-ratio percentage distribution**

Fig. 1.7 Distribution of pulsating and rotational zones in a 19 MVA hydro generator [8]

Rotational core losses are higher than pulsating losses. This difference, which is independent of frequency, increases with aspect-ratio, such that at unity aspect-ratio, it is twice the pulsating loss in the linear region of the *B*-*H* curve. This difference can be explained by use of domain theory [5], [7], [21].

A magnetic domain is a region within a magnetic material where magnetic dipoles align resulting in uniform saturated magnetization M_s [5]. A magnetic dipole is a pair of magnetic north and south poles. Magnetization is a result of the growth of domains in the linear region (weak fields), and their rotation in the nonlinear region (very strong fields) of the magnetization curve.

Consider a sample of four crystals whose magnetizations are aligned with their easy crystal axes as shown at point *o* in Fig. 1.8. Applying an external field H_a favours the growth of domains aligned with it by wall movement, increasing the flux density *B*. The growth of domains up to point *a* is reversible, since the walls have not encountered any pinning [5], [7]. Beyond point *a*, the walls will encounter imperfections where they are stuck, requiring an increase in the applied field H_a to unpin them. This is irreversible, and it is the reason why core losses are influenced by processing and handling of core materials, that result in microstructure inhomogeneities (pinning sites).

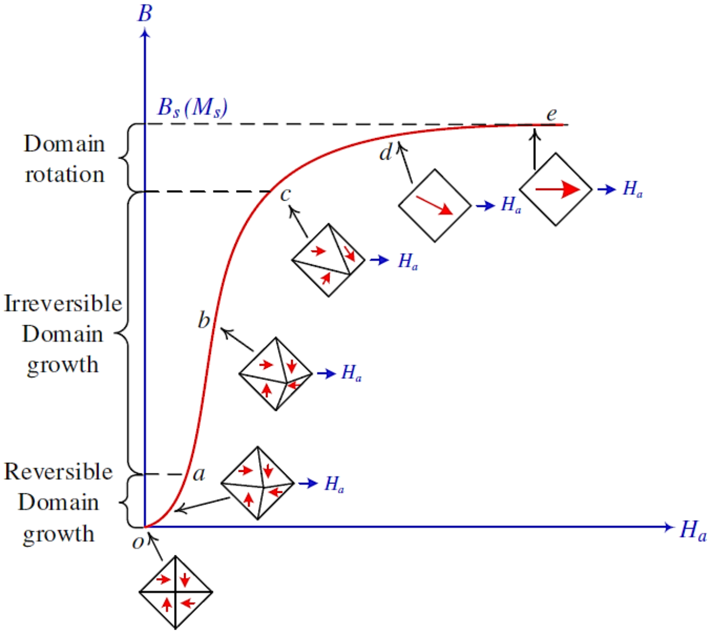

Fig. 1.8 Domain configurations during magnetization (adapted from [5])

As the applied field is increased further, the favoured domains continue to increase in volume up to about the knee point *c*. At this point, most of the domains will have rotated to their preferred orientation closest to the applied field, H_a. Increasing H_a beyond the knee, gradually rotates the domains in the direction of H_a, annihilating all the domain walls. The sample now acts like one large domain except that its magnetization M_s ($\approx B_s$) is not fully aligned with the external field, at point *d*. With further increase in H_a, the internal magnetization aligns with the external field and the material is fully saturated, with no hysteresis at point *e*.

Above point *d*, the process is reversible and is completed at point *e* where the sample is fully saturated. If H_a is reduced as in pulsating magnetization, the curve will be retraced up to point *d*. After that, it will follow the hysteresis loop of the material forming reverse domains in the single large domain.

There is no loss in the reversible regions, but in the irreversible regions, energy is used to move the walls beyond pinning sites, in annihilating and nucleating domain walls during field reversal. The *B*-*H* hysteresis loop therefore represents this energy loss in pulsating magnetizations. The energy used in domain rotation in the reversible region is returned to the external field during the field reversal [7], [20].

The previous process described pulsating magnetization, where the direction of the applied field is fixed. However, changing the direction of the applied field in rotational magnetization, results in a combination of domain wall growth and rotation. This occurs even at weak fields in the linear irreversible region. Rotation of the domains must overcome anisotropic energy, which is usually higher than domain wall movements [5], [22]. This results in a higher rotating hysteresis loss in comparison to pulsating as illustrated in Fig. 1.9. Anisotropic energy usually favours the orientation of the magnetic vector along the easy axis of a crystal [21].

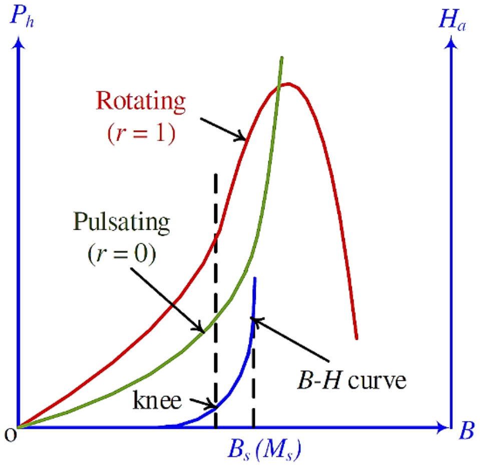

Fig. 1.9 Pulsating and rotating hysteresis loss

After the knee point, further increase in H_a tends to align the domains with the rotating field direction. With continued increase in H_a, the walls are gradually annihilated forming a single large domain at full saturation, where the internal magnetization aligns with the external field. If the applied field is strong enough to prevent the nucleation of domains and overcome anisotropy, no energy is expended since there is no formation or annihilation of domains. In addition, the internal magnetization is synchronized with the rotating externally applied field, hence, the hysteresis loss goes to zero.

Therefore, rotating magnetization results in a steep increase in the hysteresis loss curve at the knee point of the *B-H* curve, which then goes to a maximum and falls to a minimum as depicted in Fig. 1.9. The minimum point is limited by eddy-current losses and the power supply.

The existing Halbach rotational core loss tester at Concordia University power engineering laboratory is limited to 1.4 T at 60 Hz. Hence, it was insufficient in analysing rotational magnetization.

1.2 Problem Statement

The accurate estimation and modelling of core losses require data at various operating conditions. The data should account for non-sinusoidal rotational flux zones that are present in rotating machine stator cores. Additionally, manufactures provide limited sinusoidal pulsating data at specific frequencies (mostly 50 Hz and 60 Hz) and flux densities (1.0 T, 1.2 T or 1.5 T). Furthermore, most of the work that has been done in estimating core losses is based on pulsating data, such as the models used in commercial finite element analysis (FEA) packages. This results in underestimation of core losses, since rotational core losses are higher than pulsating ones. Accurate estimation of core losses is important in the uprating of MW rated and high power density machines where temperature distribution (hotspots) is key. The estimation of core losses for the stator teeth and the analysis of rotational magnetization also requires higher flux densities beyond the capability of the existing Halbach tester.

Therefore, this study proposes a compact rotational tester that extends the flux density measurement range to 2 T at 60 Hz, and maintains the same frequency range (60 Hz to 1 kHz) of the Halbach tester. Moreover, it reproduces non-sinusoidal waveforms for flux densities below 1.0 T.

1.3 Motivation

A rotational core loss measurement setup with relatively wide flux density and frequency measurement ranges, with provision for waveform control, is important in the design of electrical machines. It is from this premise that a rotational tester is proposed for high flux density measurement of core losses based on the following:

i. A rotational core loss tester allows pulsating measurements in any sample direction using only one sample, which is cost effective and faster. Epstein and single-sheet testers require the samples to be cut in different orientations. Hence, the samples have to be loaded onto the tester in the measurement of core losses for each orientation.

ii. Pulsating measurements are limited but are used to estimate the core losses under rotational flux, which results in under estimation of core losses. This error is exacerbated at higher frequencies. For example, at a flux density of 1.0 T, the measured core loss difference between an aspect-ratio of 0.8 and zero (pulsating) was 0.65 W/kg, 7 W/kg and 39 W/kg, at 60 Hz, 400 Hz and 1 kHz, respectively. Hence, rotational core loss data is invaluable in the design of high-speed machines.

iii. Although core losses are not the highest loss, they are non-uniformly distributed in the stator core. Therefore, they are important in analyzing hotspots such as when increasing the rating of large MW rated machines, predicting failure zones in high power density machines, and machines operating under transient and variable speed operation, such as in electric vehicles.

iv. The lack of rotational core loss standards in terms of design and measurements causes poor reproducibility of results. This study investigates the sources of measurement errors in detail, and suggests how they can be mitigated at the design stage of the overall measurement system (tester, sensors and data acquisition).

v. To extend rotational core loss measurements to 2 T at 60 Hz, based on the available power supply that is limited to 10 A.

The developed setup will be used to characterize electrical steels used in the design, upgrading and uprating of cored electric machines. The use of lower loss cores based on the application and cost, and uprating of MW rated machines saves on cost, improves energy efficiency and reduces emissions in the service life of a machine.

1.4 Review of Rotational Core Loss Measurements

Rotational core loss measurement methods and test benches that include sample shapes and sensing systems are discussed in this section. A comparison of measurements using different methods and in different laboratories is also presented. In addition, the challenges involved in the adoption of rotational core loss measurement standards are highlighted.

1.4.1 Measurement Methods

In rotational core loss measurements, either the sample or the field is rotated to generate a rotating flux density vector in the sample.

In the torquemetric method, the sample is rotated mechanically. Its main advantage is the direct reading of core loss from torque magnetometers, which measure torque or a change in angular speed. A uniform magnetic field H acting on a uniformly magnetized sample of magnetization M and volume V_{vol} induces a torque, T_m as [22]:

$$T_m = V_{vol}(H \times M). \tag{9}$$

If the magnetic field is non-uniform, its gradient generates a force, F_m as [22]:

$$F_m = V_{vol}(\nabla(H \cdot M)). \tag{10}$$

Therefore, to rotate a sample in a magnetic field requires energy that is equated to the core loss. It is the first method that was used in the measurement of rotational hysteresis by Baily, in 1896 [23]. Torque magnetometers are still used in the study of anisotropy, dipoles, coercivity and in the study of thin films [24], [25], [26]. They are complex and sensitive to friction and vibrations, and may require a vacuum.

Rotation of the field by use of a two or three phase winding eliminates mechanical rotation. This permits the use of the wattmetric, thermometric, and fieldmetric measurement methods. The wattmetric method is widely used in pulsating core loss measurements due to its repeatability, simplicity and availability of measurement apparatus. It is also called the voltmeter-ammeter-wattmeter or the magnetizing current method. The magnetic field is determined from the magnetizing current, resulting to better repeatability and simplicity, attributed to the high signal-to-noise ratio of the magnetic field H [27]. However, this method is rarely used in rotational measurements, due to the difficulty in defining the magnetic flux paths in rotational magnetizers [27].

The thermometric method is also called the initial rate of rise of temperature method. Core losses are determined from the rate of the rise of the temperature as [28], [29]:

$$P = C_p \frac{dT(t)}{dt}, \tag{11}$$

where C_p and $T(t)$ are the specific heat and temperature of the sample, respectively. It has higher accuracy at high flux densities [20], [28]. The disadvantages of this method include the installation, calibration and insulation of thermal sensors, a wide measurement window, low sensitivity at very low flux densities and the need for fast response thermal sensors.

The fieldmetric measurement method requires the measurement of B and H by sensors, such that the core loss per cycle at a frequency f is given by Poynting's theorem as [30]:

$$P = \frac{f}{\rho} \int \left(H_x \frac{dB_x}{dt} + H_y \frac{dB_y}{dt} \right) dt, \tag{12}$$

where ρ is the mass density of the sample. It is difficult to calibrate and align these sensors, which results to misalignment that contributes to clockwise (CW) and counter-clockwise (CCW) core loss asymmetry [20], [31]. This asymmetry occurs when the flux density vector rotation direction is changed from either direction, and the resulting core losses do not match, but diverge with increasing flux density.

At high flux densities, the fieldmetric method is susceptible to errors because of the flux density variation caused by the magnetizer, the airflux leakage and z-component magnetic fields, in addition to sensor errors [20], [28], [32]. The z-component makes the magnetic field to be non-tangential in the measurement area, while the airflux leakage field biases the measured magnetic field in terms of shape, magnitude and phase.

Regardless of these challenges, the fieldmetric method is versatile and can yield more information on the magnetic field H, such as the H locus. It is also relatively simple to implement compared to torquemetric and thermometric methods, hence, used in this study.

1.4.2 Measurement Setups and Sample Shapes

Single sheet samples are often employed in the wattmetric, thermometric and fieldmetric methods. Their shapes range from cross, strip, square to round samples. Cross and strip samples are directly wound with the magnetizing coils, which allow the attainment of higher flux densities due to the absence of airgaps. They are simple and versatile. For instance, the cross sample shown in Fig. 1.10 (a) was used to measure rotating core losses under stress, while in [33] a strip sample was used in the measurement of DC biased magnetic properties. The single strip setup shown in Fig. 1.10 (b) can be easily adapted for batch rotational core loss measurements.

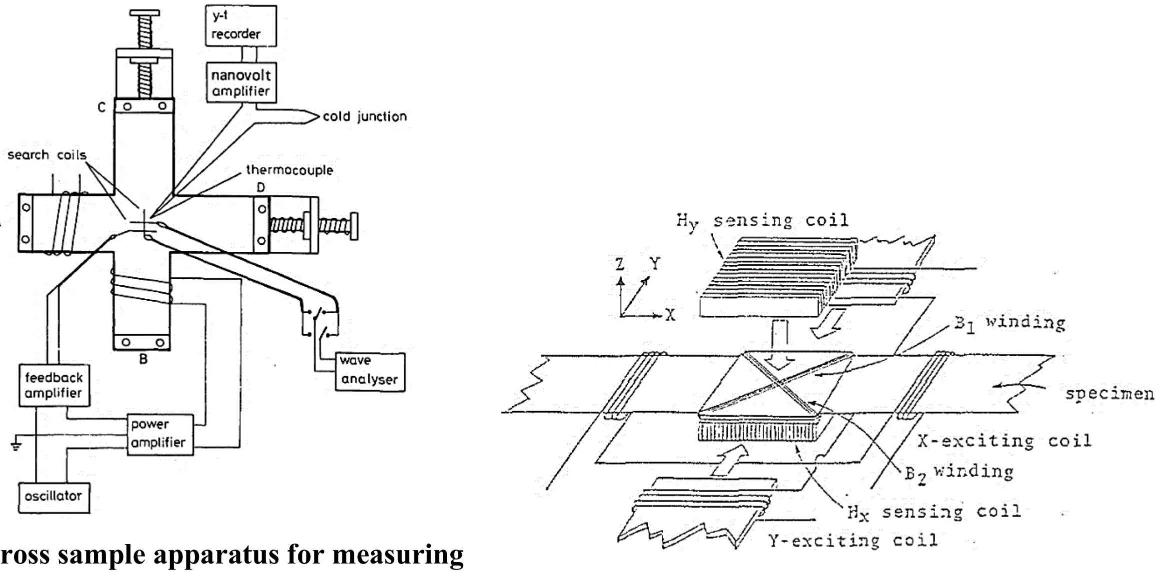

(a) Cross sample apparatus for measuring rotational losses under stress [34]

(b) Configuration of a single strip setup [35]

Fig. 1.10 Cross and strip samples

Square testers such as the one shown in Fig. 1.11 (a) are simple, can accommodate a high number of turns, and can achieve moderately high flux densities. It is also easier to incorporate DC biased magnetic measurements and domain observations in this setups [36]. However, it is difficult to achieve uniform and high flux densities at the centre of the sample in the interpolar directions, owing to flux leakage. Consequently, its measurement area is reduced to squares of 10 – 20 mm which may affect the measurement of core losses in highly grain-oriented steels (HGOS) with large grains of about 10 mm [20]. Their sample sizes are in the range of 50 - 80 mm.

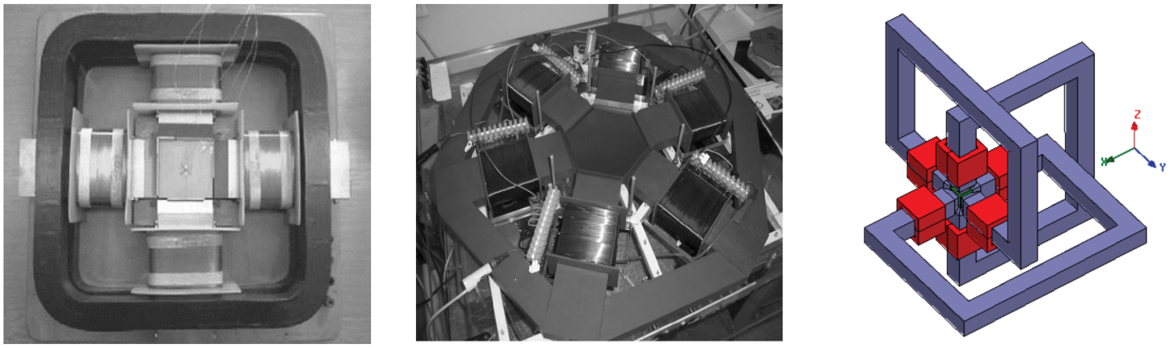

(a) A square tester [37] **(b) A hexagonal tester [20]** **(c) 3-D tester model [38]**

Fig. 1.11 Square, hexagonal and 3-D single sheet testers

Varieties of the square tester have been proposed to overcome some of these problems. For example, a vertical magnetizer with slits on its yokes [39], a triple-yoke/hexagonal setup shown in Fig. 1.11 (b) that provides magnetization support in the hard direction [20], and an eight-toothed tester with octagonal samples [40].

A three-dimensional (3-D) measurement setup was proposed in [41] to characterize soft magnetic composites (SMC) that have 3-D isotropic magnetic properties. SMC materials are well suited for 3-D electric machines (e.g. claw-pole and axial-flux), and high frequency applications [42]. Three-dimensional magnetizers, such as the one proposed in [38], whose model is shown in Fig. 1.11 (c), can be used to investigate laminating effects, and the impact of neglecting the *z*-loss in 2-D fieldmetric core loss measurements.

Round single sheet testers result in magnetization support in most magnetization directions. This is achieved by distributing the windings and equalizing the reluctance along the airgap. Consequently, they have more sinusoidal magneto motive force (MMF) in comparison to square testers, which reduces non-uniformity and magnetization asymmetry. Hence, the variation of the flux density in the measurement area with magnetization direction is minimized, and improvement in the homogeneity, result in a larger measurement region. Therefore, these magnetizers can achieve higher flux densities of about 2 T with better uniformities [43], [44].

The electromagnetic Halbach round tester shown in Fig. 1.12 (a) was proposed in [45], while a stator core based round tester shown in Fig. 1.12 (b) was used for comparative studies in [28]. In [43], a stator core based round tester with sinusoidally distributed windings, showed better performance than a square tester. A toroidally wound round tester was proposed in [46] for high frequency measurements of SMCs up to 4 kHz. Moreover, it has been used to characterize silicon-iron and iron-cobalt samples up to 1.6 T and 2.1 T, at 5 kHz, respectively [17]. The toroidal coils that are visible in Fig. 1.12 (c) reduce the end winding length; lowering resistance and inductance.

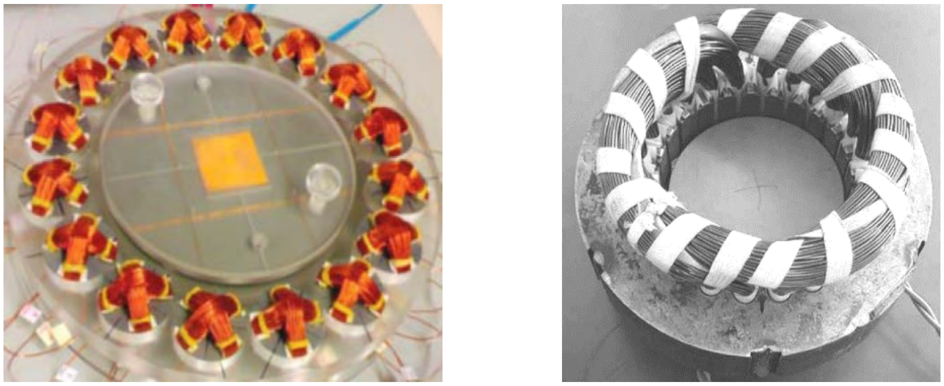

(a) Halbach round tester [45] **(b) Machine stator core round tester [28]**

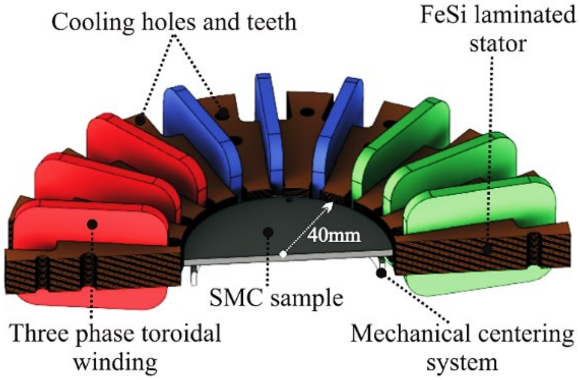

(c) Toroidal wound round tester [46]

Fig. 1.12 Round single sheet testers

Based on the advantages of round single sheet testers, they are considered in this study on how they meet the flux density requirements, and reduce the magnetizer induced non-uniformities.

1.4.3 Measurement of the Magnetic Field

The determination of the magnetic field *H* depends on the measurement method. It is not measured in the torquemetric and thermometric methods, but it is an important parameter in the wattmetric and fieldmetric methods. In the wattmetric method, it is determined from the magnetizing current and in the fieldmetric method by use of *H* sensors.

The continuity of the tangential magnetic field in the air-sample interface [5], allows the use of *H* sensors in the fieldmetric method. In other words, the tangential magnetic field inside the sample is the same as the tangential field in the air close to the sample surface. Typical magnetic field sensors are: H inductive coils (search coils), Hall sensors, magnetoresistive sensors and Rogowski-Chattock coil.

In the magnetizing current method, H is determined from Ampere's law as:

$$H(t) = \frac{N_m i_m(t)}{l_m}, \tag{13}$$

where N_m, i_m and l_m are the number of turns, magnetizing current, and the magnetic circuit mean path length, respectively.

This method requires the evaluation of the magnetic circuit, the consideration of all resistive losses, and the MMF drop of the magnetizing yoke should be negligible [47]. It is rarely used in rotational measurements because of the difficulty in defining the magnetic circuit and MMF drops.

The resistance of magnetoresistive sensors change when exposed to a magnetic field. They have higher sensitivity than Hall and inductive sensors, hence applicable in the study of local anisotropic effects [48], [49]. However, they require an auxiliary stabilizing field that limits their measurement range to about ± 6 kA/m [50]. Hence, they are rarely used in core loss measurements.

Hall sensors have a higher measurement range than magnetoresistive sensors. They use the Hall effect which induces a voltage (v_H) that is proportional to the applied magnetic field [48]. The field H acting orthogonal to the element as shown in Fig. 1.13, induces a potential difference between points a and b, that is proportional to I_H and H, as [47].

$$v_H(t) = K_H\left(I_H \times H(t)\right). \tag{14}$$

I_H is a DC current supplied externally and K_H is the sensor sensitivity, which is available in data sheets.

Hall sensors are cost effective, readily available and well suited for local magnetic field measurements. The only setback is that they require an external supply, and it is difficult to install them on the sample surface.

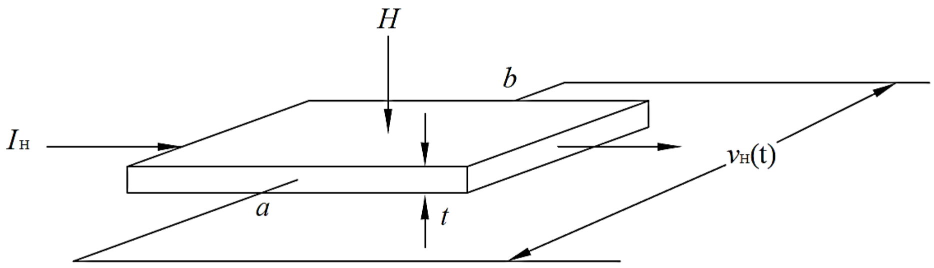

Fig. 1.13 Hall element positioned to measure the magnetic field *H*

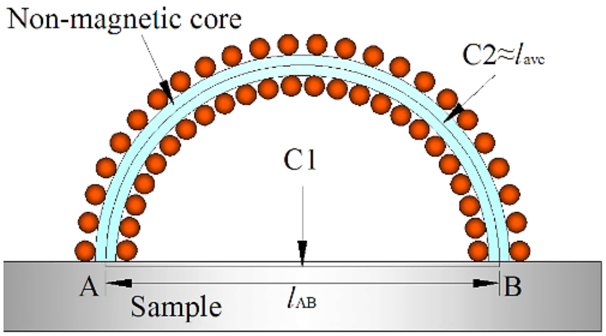

Fig. 1.14 Rogowski-Chattock coil

A Rogowski-Chattock coil is a helical coil that is uniformly wound on a non-magnetic and non-conductive flexible core bent in such a way that it ends contact the sample as shown in Fig. 1.14 [51]. Its main advantage is the capability to measure *H* directly on the sample surface.

The induced output voltage (e_R) is proportional to the rate of change of *H* between points A and B in Fig. 1.14, such that [51]:

$$e_R(t) = K_R \frac{dH_{AB}(t)}{dt}. \tag{15}$$

where K_R is the coil constant determined by calibration.

H-coils are made of thin wires with a thickness of about 0.5 mm or more [52]. To increase their sensitivity, thicker cores, double *H*-coils and multi-coil sensors have been proposed [52]. Double and multi-coil have an added advantage of improving the accuracy of measuring *H*. They are made of a high number of turns wound on a thin non-magnetic and non-conductive core, resulting in a linear relationship between the induced voltage (e_H) and the rate of change of *H* as:

$$e_H(t) = K_H \frac{dH(t)}{dt} \tag{16}$$

where K_H is the coil constant that requires calibration.

The location of inductive *H*-coils on the sample surface is shown in Fig. 1.15.

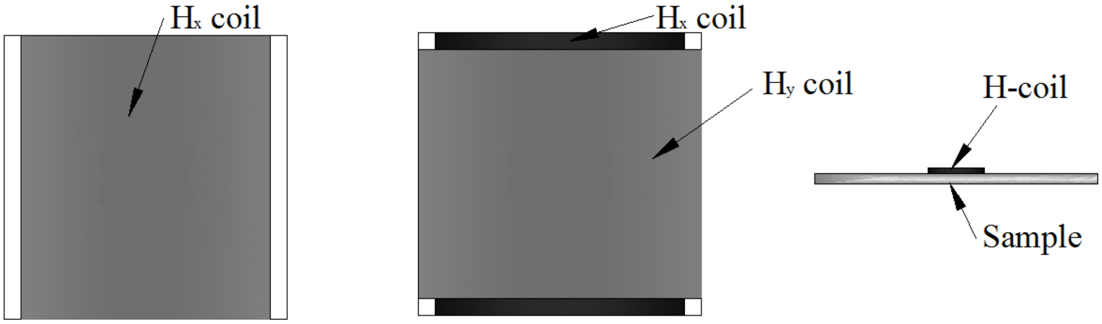

Fig. 1.15 Inductive *H*-coils

The advantages of Rogowski-Chattock and *H*-coils is linearity. The latter occupies a larger measurement area, giving better representation of material properties. Their main setback is a decrease in sensitivity at lower frequencies of less than 60 Hz, thus the need for amplification. They are also difficult to wind owing to the high number of turns made of thin wires. Hence, their accuracy depends on location and calibration.

Rogowski-Chattock and *H*-coils are prone to non-uniformly wound turns, airflux leakage fields and misalignments. They should be carefully made, calibrated, and placed where the field is uniform on the sample.

H-coils were selected based on the ease of fabrication, and a larger measurement area. However, Hall sensors were used as a cost effective way of probing local magnetic fields, for supplementing numerical design.

1.4.4 Measurement of the Flux Density

The flux density in the sample is usually measured by inductive coils using *B*-coils or *B*-tips, as illustrated in Fig. 1.16.

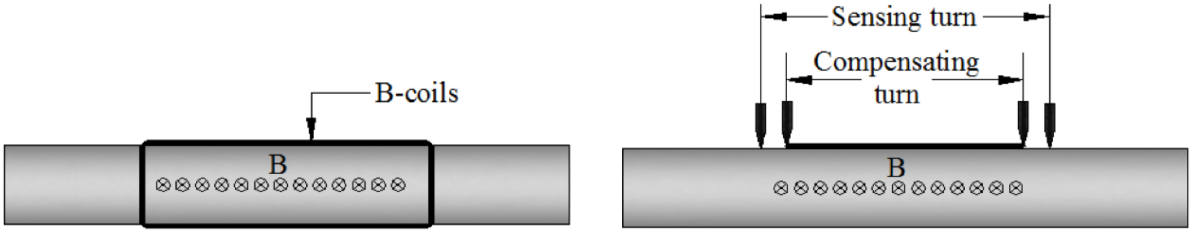

(a) *B*-coil **(b) *B*-tips**

Fig. 1.16 Inductive *B*-coils and *B*-tips

The induced *B*-coil voltage is proportional to the rate of change of the flux density as:

$$e_B(t) = K_B \frac{dB(t)}{dt}, \tag{17}$$

where K_B is the coil constant.

The *B*-tips method (also called the needle probe method) measures the induced voltage between a pair of needles. It is well suited for measuring *B* in uninsulated samples, batch and local measurements. *B*-coils require to be wound on a sample, and can be used in both uninsulated and insulated samples.

A combined *B* and *H* sensing system was proposed in [38] and in [53], for testing laminated electrical steel and SMC samples, respectively. The *B*-coils are placed on the sample surface, normal to the *B* field being measured as shown in Fig. 1.17 (a).

The performance of the surface *B*-coils has not yet been fully validated in terms of the frequency range, and the reproduction of non-sinusoidal flux density waveforms. However, they can be used for low frequency measurements, and local flux density measurements.

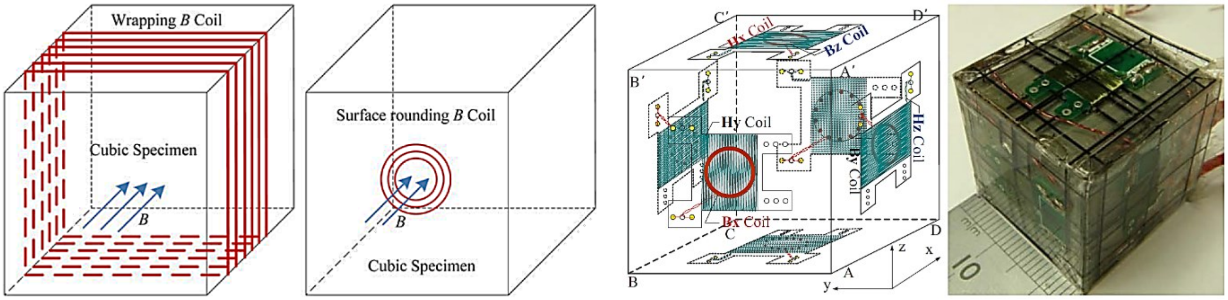

(a) Conventional and surface *B*-coils **(b) Assembled *B-H* sensing system**

Fig. 1.17 Surface *B-H* sensing system [38], [53]

Table 1.1 summarises the advantages and disadvantages of the reviewed core loss measurement methods, and their associated setups.

Table 1.1 A summary of the reviewed core loss measurement methods

Method	Apparatus	Advantages	Disadvantages
Wattmetric $H = \frac{N_m I_m}{l_m}$ $B = K_B \int e_B$	• Epstein frames, single sheet and toroid testers • Voltmeters, ammeters and wattmeters • Epstein and toroid samples	• H is determined from the magnetizing current • Better repeatability and simplicity • Available equipment • Standardized • Cost effective • Easy to implement	• Assumes the distribution of H in the sample is uniform • Not applicable in the measurement of rotational core losses • Difficult to define magnetic flux paths in 2-D rotational magnetizers
	Application: Pulsating core loss measurements		
Torquemetric $T_m = V_{vol}(H \times M)$ $F_m = V_{vol}(\nabla(H \cdot M))$ $B = K_B \int e_B$	• Rotating or vibrating sample magnetometers • Laminated or non-laminated disc samples • B sensors	• Accurate at very high flux densities • Direct measurement of core losses • H measurement is not required	• Complex mechanisms • Sensitive to friction and vibrations • Very small sample diameters • May require a vacuum chamber • Difficult to implement
	Application: Rotational core loss measurements, study of material anisotropy, dipoles and thin films		
Thermometric $P = C_p \frac{dT(t)}{dt}$ $B = K_B \int e_B$	• Pulsating and rotational setups • Thermal sensors • B sensors	• Accurate at very high flux densities • H measurement is not required	• Installation and calibration of thermal sensors • Needs a vacuum chamber • Low sensitivity at very low flux densities • Wide measurement window • Thermal sensors with fast response • Difficult to implement
	Application: Pulsating, rotational and localised core loss measurements		
Fieldmetric $P = \frac{1}{T\rho} \int \left(H_x \frac{dB_x}{dt} + H_y \frac{dB_y}{dt} \right) dt$ $B = K_B \int e_B$ $H = K_H \int e_H$	• Square, hexagonal, and round magnetizing yokes • Cross, strip, square, hexagonal and round samples • H and B sensors	• H and B loci • Relatively easier to implement than torquemetric and thermometric method	• Requires the measurement of H • Difficult to manufacture, calibrate and install H and B sensors • Prone to misalignment of sensors – contributes to CW-CCW loss asymmetry • Prone to systematic error at very high inductions
	Application: Pulsating, rotational and localised core loss measurements		

1.4.5 Standards and Comparison of Rotational Core Loss Measurements

Core loss measurement standards define the test procedures for different frequency and flux density ranges, test temperature and type of application. They also define the tester and sample sizes. These standards are well defined for Epstein, strip and toroid testers. However, the measurement difficulties associated with rotational setups causes uncertainty, resulting in a lack of standards [54]. This has prevented the characterization, adoption and standardisation of rotational measurement setups [54]. Hence, comparative results of the measurement methods and testers in the same, and in different laboratories, is the only available information.

In [54] and [55], the thermometric and the fieldmetric methods were compared with good agreement. An intercomparison of rotational core losses of samples cut from the same parent material in six European laboratories was presented in [56]. There was poor reproducibility of results attributed to measurement methods, sample and magnetizer sizes, sensors, control of the waveforms and precision in setting the control variables. However, the report fails to standardize some of these parameters such as the sample, magnetizer, measurement area and sensor sizes. This would have effectively reduced some measurement errors, which would have improved the repeatability of rotational core losses.

In spite of this, the comparison of rotational core losses between methods and laboratories is still ongoing, with positive results. In [28], the same sample was tested in two laboratories, and the results matched up to 1.4 T. In [32], there is excellent agreement between the thermometric and fieldmetric methods, as a result of waveform control and the use of round testers [28].

Therefore, the trend in rotational core loss measurements is to generate more practical based flux density patterns, perform measurements at high flux densities, high frequencies and under distorted flux densities. There is also a need to improve the measurement setups, reduce transformer noise, development of models and domain studies to describe the rotation process and explanation of the CW-CCW rotational core loss asymmetry [20], [57], [58].

This study will focus on the improvement of measurement setups by reducing systematic errors at the design stage. Additionally, an error analysis will be done to show the impact of various sources of errors, as a function of flux density under rotating magnetization.

1.5 Objective

The main aim of this study is to design a magnetizer for high flux density measurements of rotational core losses on electrical steels, for a flux density range of about 2 T at 60 Hz. This requires a reduction of the magnetizer size, which increases the non-uniformity of the flux density and measurement errors. Beyond the knee of the magnetization curve, any increase in flux density introduces additional energy requirements, which limits the achievable flux density levels and aspect-ratios, introduces systematic errors and stresses the supply. Therefore, the specific objectives meant to mitigate these effects are:

i. Propose a magnetizer that not only minimizes the variation in flux density in the measurement area, but also meets the flux density requirements within the 10 A limit of the available power amplifiers.
ii. Minimize systematic errors associated with the magnetizer design and the sizing and location of B and H sensors.
iii. Investigate the effectiveness of electromagnetic shielding in improving the measurement of the magnetic field H.
iv. Evaluate the performance of the proposed measurement setup in terms of the flux density, frequency range, sample thickness, and non-sinusoidal excitation, based on standards.
v. Evaluate the measurement errors and the uncertainty of the developed rotational core loss setup.

1.6 Methodology

The procedure that was followed in the design of the proposed setup is shown in Fig. 1.18. A review was done resulting in the selection of the round tester topology, sensors and fieldmetric measurement method, for further analysis.

A parametric numerical analysis in terms of the diametrical size, airgap, yoke depth and number of turns per phase was done to ensure the proposed magnetizer would generate a magnetic field of 30 kA/m, to achieve 2 T at 60 Hz. The flux density variation was also investigated, as it was affected by the parametric analysis. A magnetizer with the least variation in flux density, that met the design criteria, was proposed and prototyped.

The prototype allowed experimental probing of airflux leakage and *z*-component magnetic fields. Ideally, these components should be neglectable in the measurement area, which was sized by considering the length and size of *B* and *H* coils. The uncertainty of the measurement system was then determined, before using the setup for core loss measurements.

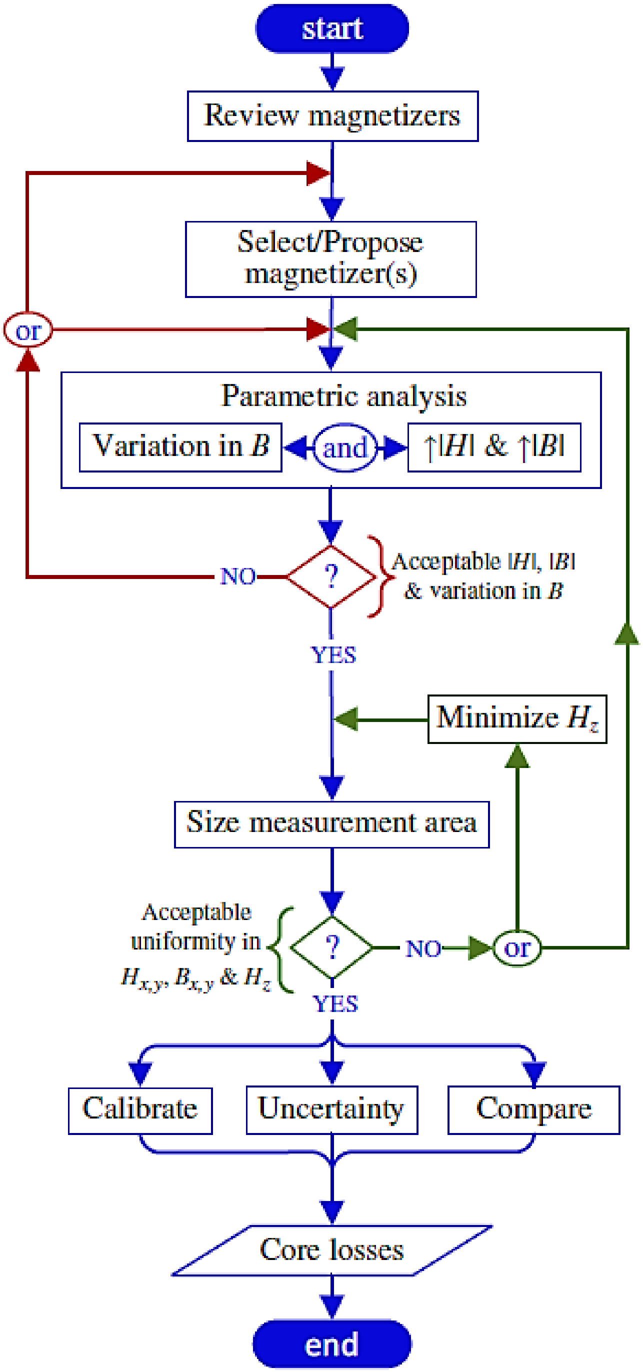

Fig. 1.18 Magnetizer design procedure

1.7 Contribution

This thesis proposes a magnetizer design procedure for high flux density rotational core loss measurements, which resulted in the following contributions:

i. Recommendation of longer effective axial length (deeper yokes) of greater than 60 mm in magnetizers to improve the homogeneity of the flux density, lower yoke losses and increases the sample magnetic loading.

ii. B-coil lengths should be greater than 40 mm in core loss measurement of unannealed samples, to minimize the effect of local degradation caused by holes, which are used to locate B-coils.

iii. Shielding at less than 9 mm should not be used in core loss measurements as it increases the magnetic field z-component as a result of magnetic interaction between the sample and the shields.

iv. The need to extrapolate the measured field, as this study will experimentally show that the airflux leakage field above the sample alters the shape, magnitude and phase of the measured field, and is one of the most dominant sources of measurement error.

These contributions resulted in the following publications:

Journals

1. **J. Wanjiku**, P. Pillay, "Design Considerations of 2-D Magnetizers for High Flux Density Measurements," *IEEE Transactions on Industry Applications*, vol. 51, no. 5, pp. 3629-3638, 2015
2. **J. Wanjiku**, P. Pillay, "Investigating the Sources of Non-Uniformity in 2-D Core Loss Measurement Setups," *International Journal of Applied Electromagnetics & Mechanics*, vol. 48, pp. 255-262, 2015

Conferences

1. **J. Wanjiku**, P. Pillay, "Design of a 2-D Magnetizer with the Consideration of the z-Component of the magnetic Field," *IEEE ECCE 2015, Montreal, Canada*
2. **J. Wanjiku**, P. Pillay, "Shielding of the z-Component of the Magnetic Field in a 2-D Magnetizer with a Deep Yoke," *IEEE IEMDC 2015, Idaho, USA*
3. **J. Wanjiku**, P. Pillay, "Investigating the Sources of Non-Uniformity in 2-D Core Loss Measurement Setups," *13th International Workshop on 1-&2-D Magnetic Measurement and Testing 2014*, Torino, Italy
4. **J. Wanjiku**, P. Pillay, "Design Considerations of 2-D Magnetizers for High Flux Density Measurements," *IEEE ECCE* 2014, Pittsburgh, USA
5. **J. Wanjiku**, N. Alatawneh, P. Pillay, "The Effect of Tooth-Width on the Distribution of Rotational Core Losses," *IEEE IEMDC 2013*, Chicago, USA

1.8 Limitation

A number of factors such as manufacturing, cutting method, stress, pressing, and handling among others, affect core losses. These factors will not be considered although they have a significant impact on the total core losses. Core loss modelling, CW-CCW rotational core loss asymmetry mechanism, and waveform control are also beyond the scope of this study.

1.9 Thesis Organisation

This thesis is organized as follows:

Chapter 1 contextualizes the research area, shows its relevance and the objectives to be achieved, and the contributions of this study. A review of core loss measurement methods, test bench setups and their sensing systems is also presented, resulting to the selection of round single sheet setups for further analysis in chapter 2.

Chapter 2 numerically investigates four round single sheet testers using 3-D finite element analysis (FEA) on how they meet the flux density requirements, with minimal induced magnetizer non-uniformity. The outcome of this chapter is a magnetizer that extend the measurement range beyond that of the benchmark Halbach tester, from 1.4 T to 2 T, at 60 Hz.

Chapter 3 analyses the systematic errors associated with uniformity in the measurement region, sizing of H and B sensors and location of the sensors. The impact of the airflux leakage field on the measured core losses is also experimentally investigated.

Chapter 4 numerically and experimentally investigates the impact of shielding in mitigating the magnetic field z-component. Moreover, the impact of design parameters such magnetizer diametrical size and yoke depth on the magnetic field z-component, are also discussed.

Chapter 5 assesses the flux density and frequency measurement range of the proposed tester using two samples, with different thickness. Moreover, it shows that rotational measurements are important in the design of high-speed machines, where the difference between rotational and pulsating core losses is substantially higher in terms of magnitudes. The ability of the proposed magnetizer to reproduce numerical B-waveforms, without any B-waveform control, is also demonstrated. The magnetizer limits are also discussed.

Chapter 6 describes a quantitative based procedure for estimating the uncertainty of the developed measurement setup from elementary errors of B and H. Additionally, it is shown that the highest component of uncertainty in fieldmetric measurement of core losses is systematic. In particular, the *H*-coil airflux leakage field error, which contributes about 70 % to the total uncertainty.

Chapter 7 concludes the thesis by showing the relevance of the study in the design and analysis of rotational core loss testers, and recommends improvements to the developed test bench.

1.10 Conclusion

The importance of soft magnetic materials in reducing the size and core losses was demonstrated. The selection of these materials is based on the application, which defines the frequency and flux density. The inadequacy of pulsating tests in the measurement of rotational core losses, and flux density limit of the existing Halbach tester was highlighted. This resulted in the motivation of the need of a rotational magnetizer that can allow the characterization of electrical steels up to about 2 T or higher, at 60 Hz.

The research area was scoped based on the objectives and limitations, and the contributions were highlighted. This lead to a review of rotational measurement methods, test benches and *B* and *H* sensors led to the selection of the fieldmetric measurement method, round testers, *B*-coils, Hall sensors for local magnetic field probing and *H*-coils for larger measurement areas.

The next chapter analyses testers for high flux density measurement of rotational core losses, and how they affect the uniformity of the flux density in the sample.

Chapter 2. Design Considerations of Rotational Magnetizers for High Flux Density Measurements

The main objective of this chapter is to propose a magnetizer that extends the current flux density (B) measurement range of a 16 pole Halbach magnetizer, from 1.4 T to 2 T, at 60 Hz. This Halbach magnetizer was proposed in [45], and is available at the power engineering laboratory, Concordia University. It has very high uniformity owing to its large sample size, wide airgap and moderate yoke depth. However, its large size and wide airgap reduces its flux density measurement range.

Achieving higher flux density loadings require a reduction of the magnetizer diametrical size, which reduces the magnetic flux path, l_m that is proportional to the sample size. The ampere-turns ($N_m I_m$) should be kept constant, and if possible increased, to increase the magnetic field (H), since:

$$H \alpha \frac{N_m I_m}{l_m}. \tag{18}$$

The impedance of the magnetizer limits the current, while reducing the yoke and increasing the number of turns increases the inductance (L_s) as:

$$L_s \alpha \frac{N_m^2}{l_m}, \tag{19}$$

Which reduces the frequency measurement range. In addition, reducing the sample size requires a reduction in the measurement region. Therefore, the proposed magnetizer should meet the following requirements:

1. Minimal variation in B and H in the measurement region, as a result of the magnetizer design.
2. A large uniform measurement region; better representation of material properties independent of grain sizes [56], and other inhomogeneities.
3. Magnetize the sample to very high flux densities to about 2 T at 60 Hz, within the limits of the available power supply (10 A).
4. Meet and/or extend the current frequency measurement range of 60 Hz to 1 kHz.

A reduction in magnetizer size increases the flux density variation across the sample, with change in magnetization direction. In addition, it results in a higher airflux leakage and *z*-component magnetic fields. Under rotating magnetization assuming isotropic conditions, the flux density vector magnitude is supposed to be constant, but magnetizers introduce directional dependent flux density variation. Furthermore, magnetizers also induce non-uniformity in the distribution of the flux density in the sample, in a given magnetization direction. Therefore, the mitigation of magnetizer induced flux density variation and non-uniformity, should be done at the design stage.

This variation at high flux densities require additional MMF, limiting the attainable aspect-ratios, flux density levels and stresses the supply. For instance, numerical results will show that a 3 % flux density variation resulted in a 36 % magnetic field variation in a square tester at 1.8 T. A numerical methodology that accounts for the flux leakage and the eddy-currents is therefore proposed to analyse uniformity and flux density variation in rotational magnetizers.

Four magnetizers were numerically designed and analysed; a square single sheet tester (SSST), Halbach round single sheet tester (HaRSST), conventionally wound induction machine round single sheet tester (CW-IMRSST) and sinusoidally wound induction machine round single sheet tester (SW-IMRSST). The magnetizers are shown in Fig. 2.1. The analysis was done beyond the knee of the magnetization curve, where any variation in flux density requires a significant increase in the MMF that is proportional to the magnetic field *H*.

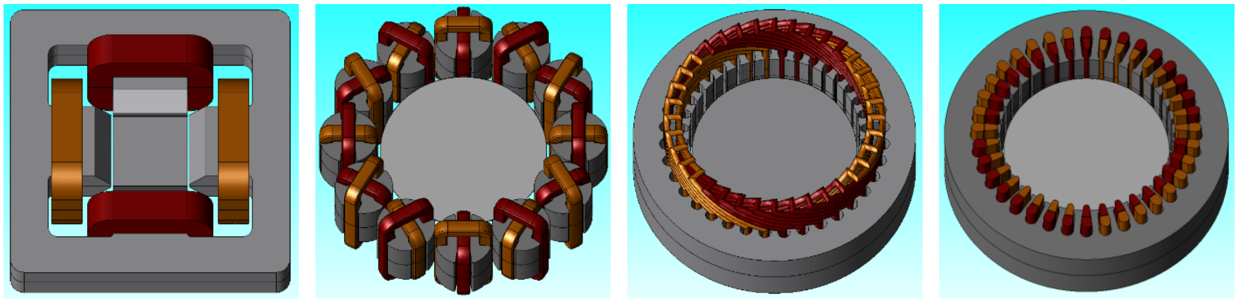
(a) Square-SST **(b) Halbach-RSST** **(c) CW-IMRSST** **(d) SW-IMRSST**

Fig. 2.1 The analysed four rotational magnetizer topologies

Numerical results will also show that round magnetizers can reduce the flux density variation, which is over 92 % for a square magnetizer, by making the MMF more sinusoidal, and equalization of the reluctance along the airgap [43]. In addition, deeper yokes (longer axial effective length) are also shown to minimize the flux density variation, increase the magnetic loading (by increasing *H*) and enlarging the measurement region. For example, doubling the yoke depth of a square and Halbach magnetizers reduced their flux density variation by 50 %, while their magnetic fields were increased by about 30 % and 70 %, respectively.

The result of this numerical analysis is a design that minimized the flux density variation by a combination of sinusoidally distributed windings, and a deep yoke. The proposed magnetizer achieved very high flux densities over a relatively wide frequency range, i.e. 2.04 T and 1.69 T at 60 Hz and 1 kHz, respectively. It extended the flux density measurement range by 43 % and magnetic field from around 1.1 kA/m to about 40 kA/m, with reference to the benchmark 16 pole Halbach model. In addition, the proposed magnetizer is experimentally shown to have a high circularity of *B*, which is an indicator of minimal flux density variation.

2.1 Numerical Analysis Methodology

Numerical analysis allowed the investigation of non-magnetic contributions to non-uniformity that are superposed on magnetic ones. For instance, isotropic *B-H* curves eliminate any anisotropic effects, but practically, it is difficult to isolate the contributions from anisotropy, *B*-holes and the magnetizer itself. Three-dimensional FEA models were used as they account for the thickness between the sample and yoke, which contributes to non-uniformity, higher *z*-component and airflux leakage magnetic fields. A transient (TR) solver was selected as it is accurate in the computation of *B* and *H*, at saturated conditions [59]. The steady state frequency (FQ) solver of the used numerical package, assumes that the magnetic field changes sinusoidally. This requires the linearization of the *B-H* curve, which results in the underestimation of flux density values in saturated conditions [59].

The benchmark 16 pole Halbach tester was used to calibrate the 3-D FEA model (meshing, solver settings etc.), whose settings were then adapted for the other cases. Nonlinear isotropic *B-H* curves at 60 Hz were assigned to magnetic parts. The sample was an M19G24 non-oriented electrical steel, that is 0.635 mm thick. Half of the model was analysed due to symmetry, which reduced the sample thickness to 0.3175 mm. A very fine mesh of 0.4 mm was assigned to the sample for high elemental aspect ratio. This resulted in two layers of mesh elements in the sample thickness for the whole model. The airgap was finely meshed since it is a transition region of the flux density from high (sample) to low (yoke), in addition to high dimensional changes. The teeth edges near the sample were set to a mesh size of 0.5 mm, while the teeth face and the rest of the stator were assigned to a mesh size of 2 mm and 10 mm respectively. The mesh size of the coils was set to a range of 2 mm to 4 mm depending on the model size. The air box was 2.5 times the model dimensions, to ensure the field lines do not influence the magnetic loading of the sample. Eddy-currents, which affect the permeation of flux into the sample, were only enabled in the sample to lower computation time. Fig. 2.2 shows the mesh developed for a 3-D model.

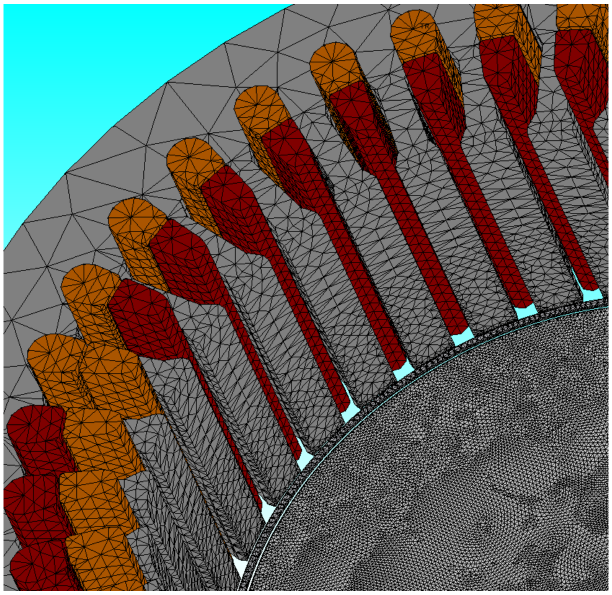

Fig. 2.2 Meshing of a 3-D model

The analyses were done beyond the knee of the *B-H* curve under a clockwise rotating *B*-vector in steps of 15 ° from 0 ° to 45 °. The 0 ° position was aligned with the *y*-axis. The *B* and *H* data points were determined from 20 mm and 60 mm measurement lines, for the square and the round testers, respectively. The lines were shortened to reduce the bias of the edge effects. These measurements lines were evenly spaced at the center of the sample, and were rotated with the magnetization direction. The measurement lines for *H* and *B* plots were located on the sample surface ($z = 0.3176$ mm), and the mid-section of the sample ($z = 0$ mm), respectively. The same current of 10 A at 60 Hz, was used in all the models. The placement of these lines for the normal and parallel components ($|B_n|$ and $|B_p|$) with respect to the magnetization direction, is shown in Fig. 2.3.

The figure also shows the measurement line for the *z*-component of the magnetic field (H_z), and the placement of the Hall sensors, for experimental measurement of the same. In addition, it also shows the non-uniform distribution of the flux density in a round sample.

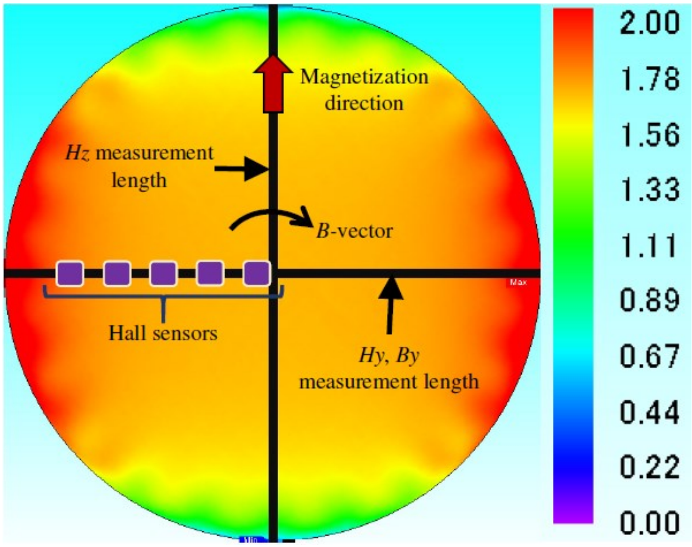

Fig. 2.3 Locations of lines for measuring H_z, H_y and B_y for numerical analysis, and Hall sensors for experimental measurements of H_z, and the non-uniform distribution of $|B|$ in tesla [T]

Parallel plots ($|B_p|$ and $|H_p|$) had higher deviations than normal plots ($|B_n|$ and $|H_n|$) at 0 ° (aligned with the *y*-axis). Hence, they were used for analyses as they represented the worst case scenario. This was confirmed by comparing their average absolute deviation (*abs_dev*) for $|B_n|$ and $|B_p|$ expressed in equation (20). Uniformity was quantized by *abs_dev*(*x*) as:

$$abs\_dev(x) = \frac{1}{n}\sum_{k=1}^{n}\left|x_k - \bar{x}_d\right| \ , \tag{20}$$

and deviation, *dev*(<*x*>) as:

$$dev(<x>) = \frac{\max\left(\{\bar{x}_d\}\right) - \min\left(\{\bar{x}_d\}\right)}{\bar{x}_m}, \tag{21}$$

where *n* is the number of data points derived from a *H* or *B* plot. The instantaneous average value in a given magnetization direction was $\bar{x}_d$. The absolute deviation, *abs_dev*(*x*) was used to determine uniformity in a given magnetization direction, while *dev*(<*x*>) determined the deviation in a set $\{\bar{x}_d\}$, whose elements corresponded to the number of magnetization directions. The average of the set was:

$$\bar{x}_m = \frac{1}{n}\sum\left\{\bar{x}_d\right\}, \tag{22}$$

for n magnetization directions. The deviation, $dev(<x>)$ was therefore used to quantize the variation in B and H caused by the magnetizer, with changing magnetization direction.

Eddy-currents introduce non-uniformity in flux density distribution, which can affect the computation of uniformity at frequencies higher than 60 Hz. The opposing spurious fields lower the magnetic loading and uniformity in the sample. Numerical analysis at 200 Hz, 400 Hz and 1 kHz, resulted in more spurious distribution of the flux density in the sample, as compared to that at 60 Hz. These fields depend on the frequency and the magnitude of the applied field. Therefore, to analyse the contribution of the magnetizers to flux density variation and uniformity, it was necessary to reduce the impact of eddy-currents. This was achieved by using a quasi-static frequency of 60 Hz, a fine sample mesh (mesh size of 0.4 mm), and reducing the solver tolerance to 10^{-4}, from 10^{-3}. These measures improved the distribution of the flux density at 60 Hz, and significantly reduced the noise in their plots.

Therefore, analysing magnetizers at higher frequencies requires a modification of the mesh (e.g. increasing the number of mesh layers) and solver settings. Such measures are necessary to ensure that dynamic effects do not bias the results, and are accounted for in the analysis. These model settings together with analyses at the nonlinear region of the magnetization curve, and the high dimensional and flux density differences between the yoke and the sample, will significantly increase the computation time.

The next sections determine the parameters of the four magnetizers (square-SST, Halbach-RSST, conventionally wound-IMRSST, sinusoidally wound-IMRSST), whose 3-D FEA models are shown in Fig. 2.1 The parameters of the square tester were assumed from literature, while the rest of the magnetizers were sized analytically.

2.2 Square Magnetizer (SSST)

A square tester with an 80 mm by 80 mm sample, with a measurement area of 20 mm by 20 mm, and an airgap of 2 mm from [37], was considered. Its magnetizing poles were chamfered to smoothen the concentration of the field into the sample. The SSST allowed the analysis of the effect of the sample shape and the concentrated winding design, on flux density variation.

2.3 Halbach Magnetizers (HaRSST)

A 2-phase electromagnetic Halbach magnetizer allows the control of the magnitude, frequency and relative phase of the two exciting fields. The poles are arranged in such a way as to concentrate the flux in the interior of the yoke, while cancelling it on the outside. The geometric formulations used in [60], to size magnetic poles and position them, are modified to account for interpolar clearance (g_{int}), sample radius (r_s) and the airgap (g) between the sample and the poles. The parameters are illustrated in Fig. 2.4, where r_p is the pole radius, r_{pcd} is the radius to the centre of the pole cP_i , α is the angle between the poles and β_i is the magnetization direction of the i^{th} pole with respect to the y-axis.

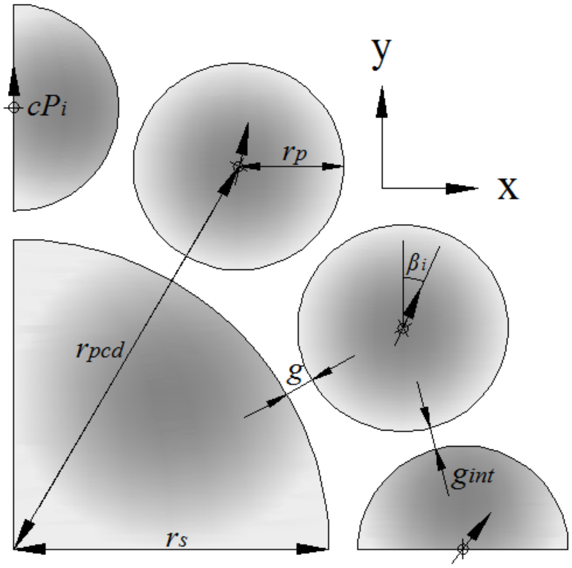

Fig. 2.4 Schematic of a quarter of a 12 pole Halbach magnetizer

The pole radius is therefore given as:

$$r_p = \frac{r_i \sin\left(\frac{\alpha}{2}\right) - \frac{g_{int}}{2}}{1 - \sin\left(\frac{\alpha}{2}\right)}, \tag{23}$$

where r_i is the inner radius of the Halbach ring, given by the sum of the sample radius (r_s) and airgap length (g). The slot sizes can then be determined based on the wire gauge and the slot-fill factor. To increase the magnetic loading with acceptable uniformity, the number of poles, the sample diameter and the yoke depth were varied, at a fixed airgap of 2 mm. The first two cases are presented first, and the yoke depth is discussed later in sub-section 2.5.2.

2.3.1 Number of Poles

Increasing the number of Halbach poles improves uniformity at the expense of lower flux densities [45]. To achieve sample saturation, the magnetizer size was reduced to sample diameters of about 100 mm, which reduced the sample and pole diameters as expressed in equation (23). This increased the poles' magnetic loading which was compensated by increasing the pole depth. It was also difficult to maintain the same number of turns for the same wire gauge. Consequently, the number of poles had to be reduced, in order to increase the pole diameter, and accommodate the same number of turns per phase.

Two-dimensional FEA static analysis was used under *x*-axis excitation, as the study was comparative. HaRSST models with 8, 12 and 16 poles of 100 mm sample diameter, and 2 mm airgap were compared with respect to the 16 pole model with a 100 mm sample, for the same number of turns per phase. The results shown in Fig. 2.5 (a), are from the normal components of B (B_n) normal to the magnetization direction, from the center to the edge of the sample.

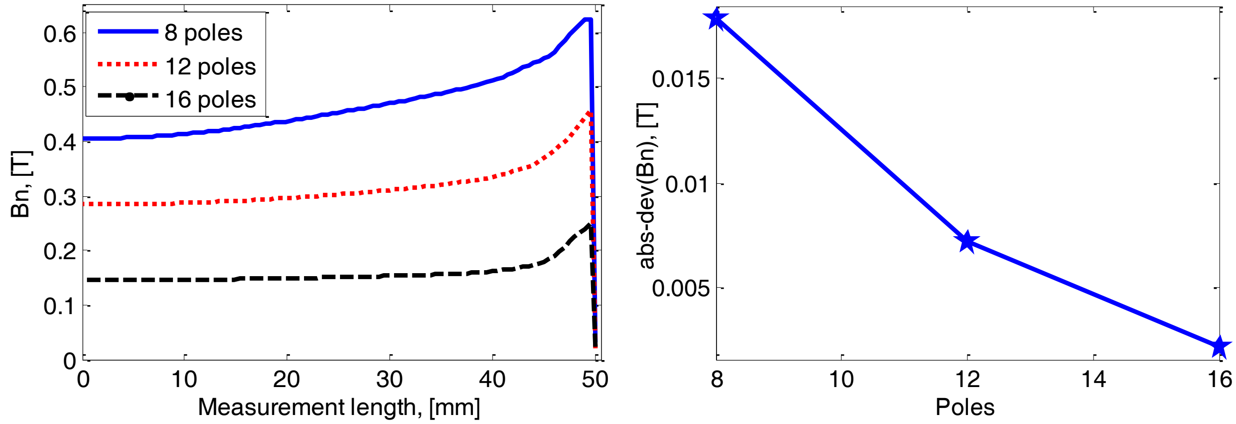

(a) Dependency of the sample's flux density loading on the number of Halbach poles

(b) Improving uniformity with increasing number of Halbach poles

Fig. 2.5 Effect of the number of poles on flux density and uniformity, for HaRSSTs

Reducing the number of poles increased the flux density significantly as shown in Fig. 2.5 (a). The 8 and 12 poles roughly tripled and doubled the flux density of the 16 pole case. This is because of the increase in the number of turns per pole for the same number of turns per phase, which resulted in the concentration of the MMF. The increase in non-uniformity followed the decrease in the number of poles. It was about eight and three times that of 16 poles, for 8 and 12 poles as shown in Fig. 2.5 (b). This is because the MMF becomes more non-sinusoidal with a reducing number of poles, which increased the flux density variation.

Therefore, to allow for a reduction in magnetizer size to achieve higher flux densities, maintain acceptable uniformities, and have woundable poles for the same number of turns, the number of poles was selected as 12. It doubled the flux density of the 16 pole case, at an acceptable uniformity.

Significant increase in the flux density, with better uniformity by changing the pole shape from circular to square or octagon is reported in [60]. However, it is applicable to larger poles where magnetic saturation and slot dimensions are not constrained, such as 4 or 8 poles.

2.3.2 Sample Diameter

The four diameters that were compared using 3-D FEA TR analysis are 106 mm, 120 mm, 140 mm and 200 mm. The first three cases had 12 poles, 2 mm airgap and 40 mm yoke depth, while the last one was the benchmark model with 16 poles, 10 mm airgap and 20 mm yoke depth. The effect of the sample diameter is presented at 0 ° magnetization direction. This direction has the highest non-uniformity for Halbach testers as it is aligned with slot-openings of the poles. Reluctance is also highest along the sample diameter.

A decrease in the sample diameter by reducing the magnetizer size increases both the flux density and the non-uniformity. In Fig. 2.6 (a) and (b), the 106 mm to 140 mm cases doubled the flux density of the 200 mm case.

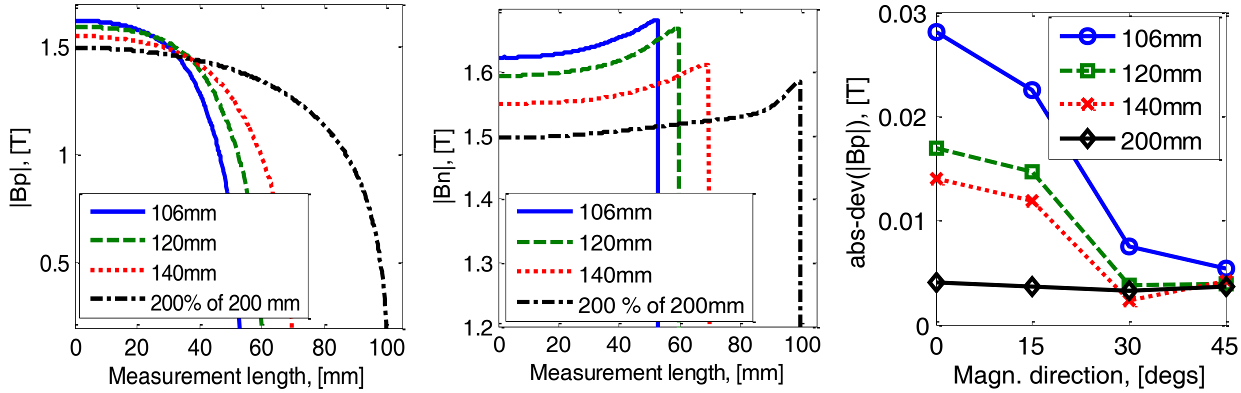

(a) Parallel components **(b) Normal components** **(c) Uniformity**

Note: The HaRSST-200 mm case was multiplied by a factor of two (200 %) to be at the same flux density level as the other cases

Fig. 2.6 Effect of sample diameter on flux density and uniformity, for HaRSSTs

This significant increase in magnetic loading sacrificed uniformity as shown Fig. 2.6 (c), where the 106 mm and 200 mm cases have the least and highest uniformities, respectively. This is because the measurement area includes more non-uniform regions, which are brought closer together with a reduction in sample diameter.

The disadvantage of increasing the diameter is that the attainable flux density decreases. For example, the benchmark model (200 mm case) had 50 % less magnetic loading compared to all the other cases, under the same excitation. Hence, its flux density waveforms were multiplied by a factor of two, to be at the same flux density level for comparison purpose as shown in Fig. 2.6 (a) and (b). Its lower flux density was also caused by its larger 10 mm airgap. From this analysis, a 12 pole HaRSST of 120 mm sample diameter, and 2 mm airgap was selected as a trade-off between magnetic loading and uniformity.

2.4 Induction Machine Stator Yoke Magnetizers (IMRSST)

A conventionally and sinusoidally wound-IMRSSTs are considered in this section. They are based on the use of an induction machine stator yoke, hence the term induction magnetizers. The designs were based on the availability of a 36 slot stator yoke whose inner diameter was 109 mm. The IMRSSTs are wound such that two poles are generated in their interior. As a result, the possible number of poles is 2 and 4; with the latter being selected to reduce the length of the end windings.

2.4.1 Conventionally Wound-IMRSST (CW-IMRSST)

The number of slots was made an even multiple of three, giving the possible number of slot as 12, 18, 24 and 36. This allowed the use of the inbuilt 3-phase coiling tool of the FEA package [59]. To improve uniformity, the quotient of the number of slots and the 4 poles must be an integer. This split the phase winding into a multiple of two, eliminating 18 slots, while 12 slots were excluded by the need of more sinusoidal MMF. The conventionally wound-IMRSST was therefore a 36 slot 2-phase magnetizer with double-layer fully pitched windings.

2.4.2 Sinusoidally Wound-IMRSST (SW-IMRSST)

In [43], it is shown that sinusoidally distributing the windings makes the resultant MMF sinusoidal in every magnetization direction. This significantly reduces the flux density variation, as compared to other magnetizer topologies.

The number of turns per phase is usually high in magnetizers to achieve higher magnetizing fields. Assuming a slot-fill factor of 40 % and a current density of 3 A/mm^2, the maximum number of turns per slot, $N_{t\max}$ was found to be 70 turns. Hence, the conventional double-layer winding had 35 turns per coil. The turns per coil for the sinusoidal winding are expressed as:

$$N_x = A_{turns} \sin\theta_s \text{, and:} \tag{24}$$

$$N_y = A_{turns} \cos\theta_s \text{,} \tag{25}$$

where $N_{x,y}$ are the turns per slot for the x, y phases dependent on the slot-angle, θ_s. The amplitude, A_{turns} is determined from $N_{t\max}$ at 45 º or 225 º slot-angle, for a double-layer winding as:

$$A_{turns} = \frac{N_{t\max}}{|2\cos\theta_s|} \bigg|_{\theta_s = 45^\circ \ or \ 225^\circ} . \tag{26}$$

The distribution of turns in slots for the two types of winding is shown in Fig. 2.7, which resulted in the winding diagrams of Fig. 2.8. The only setback in sinusoidally distributed winding is the longer end-windings.

The sinusoidal winding generates a travelling sinusoidal MMF along the airgap dependent on the instantaneous current amplitudes of the two phases. That of the conventional winding is dependent on the winding harmonics and instantaneous current amplitudes. This is evidenced in Fig. 2.9 for the two windings at two time instances. The difference in the flux density variation for the IMRSSTs will be caused by the two winding configurations.

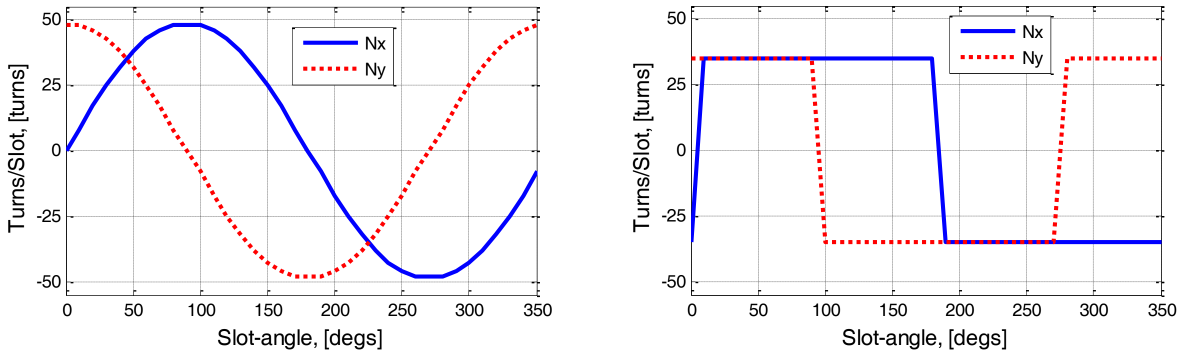

(a) Sinusoidal distribution

(b) Conventional distribution

Fig. 2.7 Distribution of turns in slots

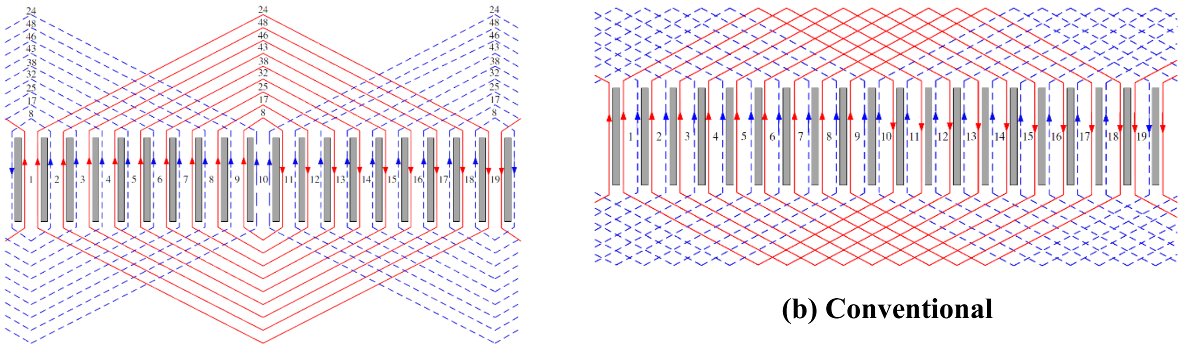

(b) Conventional

(a) Sinusoidal

Fig. 2.8 Half of the winding diagrams

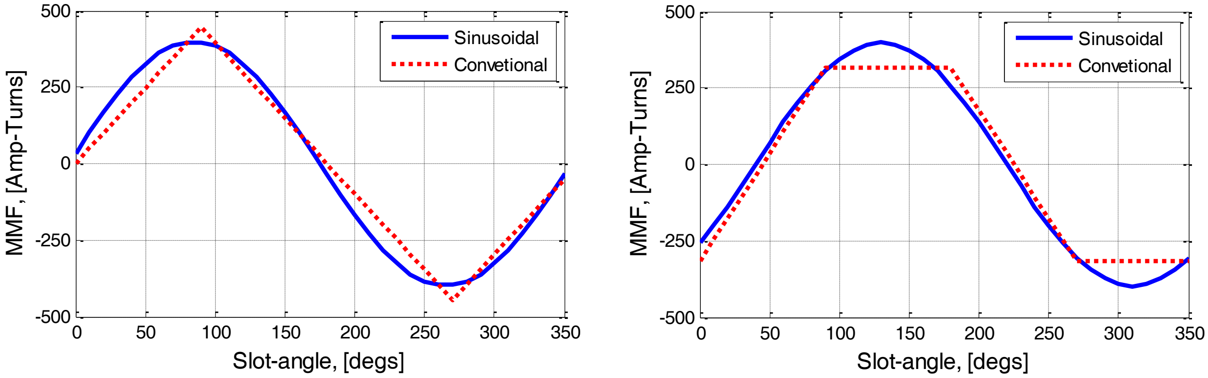

(a) time = 0 secs (= 0 º)

(a) time = 0.002083 secs (= 45 º)

Fig. 2.9 MMF waveforms at different instantaneous currents, at 60 Hz and $I_{mx} = I_{my} = 1$ A

2.5 Analysis of Numerical Results

The parameters of the four topologies are given in Table 2.1. They were numerically simulated under the same current of 10 A, with the y-current shifted by 90 º, to generate a CW rotating B-vector. The 16 pole HaRSST tester was used as a benchmark model, whose achievable flux density needed to be increased beyond 1.4 T to 2 T, at 60 Hz.

Table 2.1 Parameters of the four rotational magnetizer topologies

Magnetizer	Sample size (mm)	Airgap (mm)	Yoke depth (mm)	Winding
Square-SST	80 by 80	2	40	concentrated
12 pole HaRSST	120	2	40	distributed
16 pole HaRSST	200	10	20	distributed
36 slot CW-IMRSST	105	2	40	distributed
36 slot SW-IMRSST	105	2	40	distributed

2.5.1 Flux Density Variation with Magnetization Direction

Ideally, the rotating *B*-vector should not vary in magnitude with change in magnetization direction, except as a result of magnetic properties. It will be shown that the selection of a 2-D magnetizer and winding design in case of IMRSSTs, is important in reducing this variation.

The flux density distribution patterns in the sample should be repetitive with change in magnetization direction. However, as seen in Fig. 2.10 (a) to (d), magnetizers induce direction dependent magnetization asymmetry. These results are independent of the sample anisotropy, since isotropic *B-H* curves were used in the numerical analysis. Consequently, any flux density variation (hence *H*) with direction, is attributed to the magnetizer design.

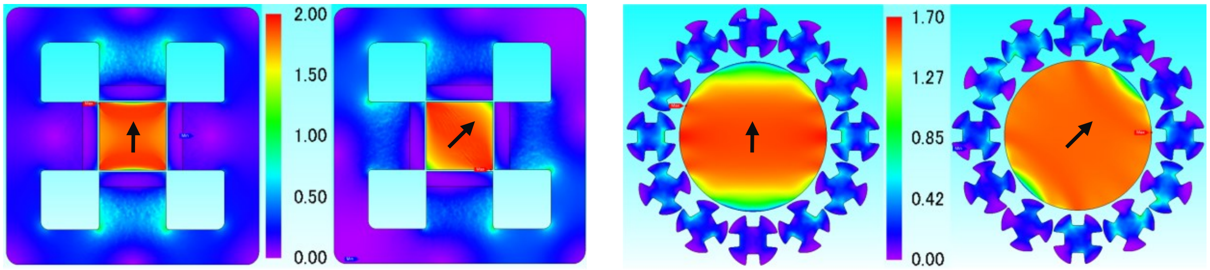

(a) Square-SST **(b) 12 pole Halbach-RSST**

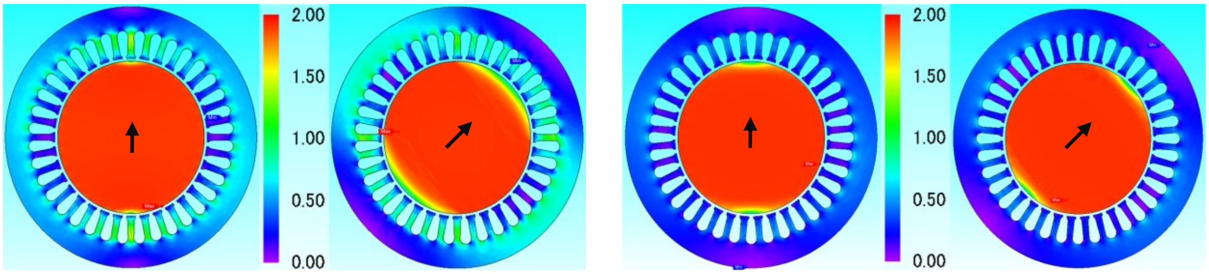

(c) Conventionally wound-IMRSST **(d) Sinusoidally wound-IMRSST**

Fig. 2.10 Variation in |*B*| patterns in tesla [T] of the four models at 0 º (*y*-axis) and 45 º magnetization directions as indicated by the arrows

The distribution of |*B*| in the yokes of Fig. 2.10 shows low operating yoke flux densities of less than 0.5 T, in the linear region of the *B-H* curve. This lowers the magnetizing energy drop in the yoke, while operating beyond the knee induces current harmonics, which affects the applied and measured magnetic fields, i.e. yoke effects.

The flux density is lowest in the magnetization direction at the sample edges as seen in |*B*| patterns of Fig. 2.10. This is because the eddy-currents that generate opposing fields are highest along the magnetization direction as shown in Fig. 2.11 (a). The magnetization direction is as indicated by the vector plot in Fig. 2.11 (b). Moreover, the highest reluctance (longest path length) is along the sample diameter, which further lowers the magnetic loading along the magnetization direction. Hence, flux will recirculate through the least paths of reluctance, elevating the magnetic loading towards the sample edges, perpendicular to the magnetization direction.

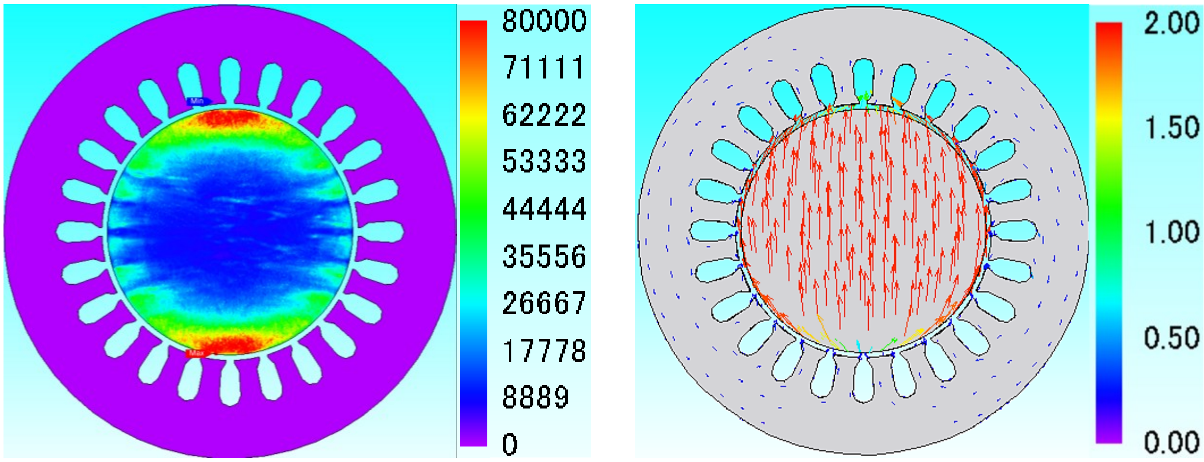

(a) Eddy-current, J distribution in A/m^2 **(b) Vector plot of $|B|$ in tesla, [T]**

Fig. 2.11 Distribution of $|B|$ and eddy-currents in the SW-IMRSST, at 0 º (y-axis) magnetization direction

The variations shown in Fig. 2.10 are further represented as plots of $|B_p|$ in Fig. 2.12. The plots further confirm a decrease in the flux density variation with a change of magnetizer design from square to round testers, i.e. $\Delta B1 > \Delta B2 > \Delta B3 > \Delta B4$, in Fig. 2.12. Non-uniformity (*abs_dev*) decreased from 0.0226 T to 0.0019 T corresponding to the square and the Halbach-RSST-120 mm testers as seen in Fig. 2.12 (a) and (b). The use of IMRSSTs further decreased the variation, since their *abs_dev*($<|B_p|>$) was about 0.0001 T, as validated in Fig. 2.12 (c) and (d). This is over 92 % reduction in flux density variation by RSSTs over the SSST. The measurement area also increased following a decrease in the flux density variation, i.e. $x1 < x2 < x3 < x4$, in Fig. 2.12.

The reduction in the flux density variation is attributed to more sinusoidal magnetizing MMF, and equalization of the reluctance in most directions for the RSSTs, as compared to the SSST. This was achieved by transitioning from the concentrated winding of the square tester to its distribution in the Halbach and conventionally wound IM testers, and finally to sinusoidally distributing it in a sinusoidally wound IM tester. Additionally, the magnetizer yoke design in terms of the number of teeth in IMRSSTs and number of poles in HaRSSTs, contributed to a lower flux density variation by increasing the airgap reluctance frequency. This is analogous to decreasing the pulsating torque frequency in rotating machines, by increasing the number of poles and slots.

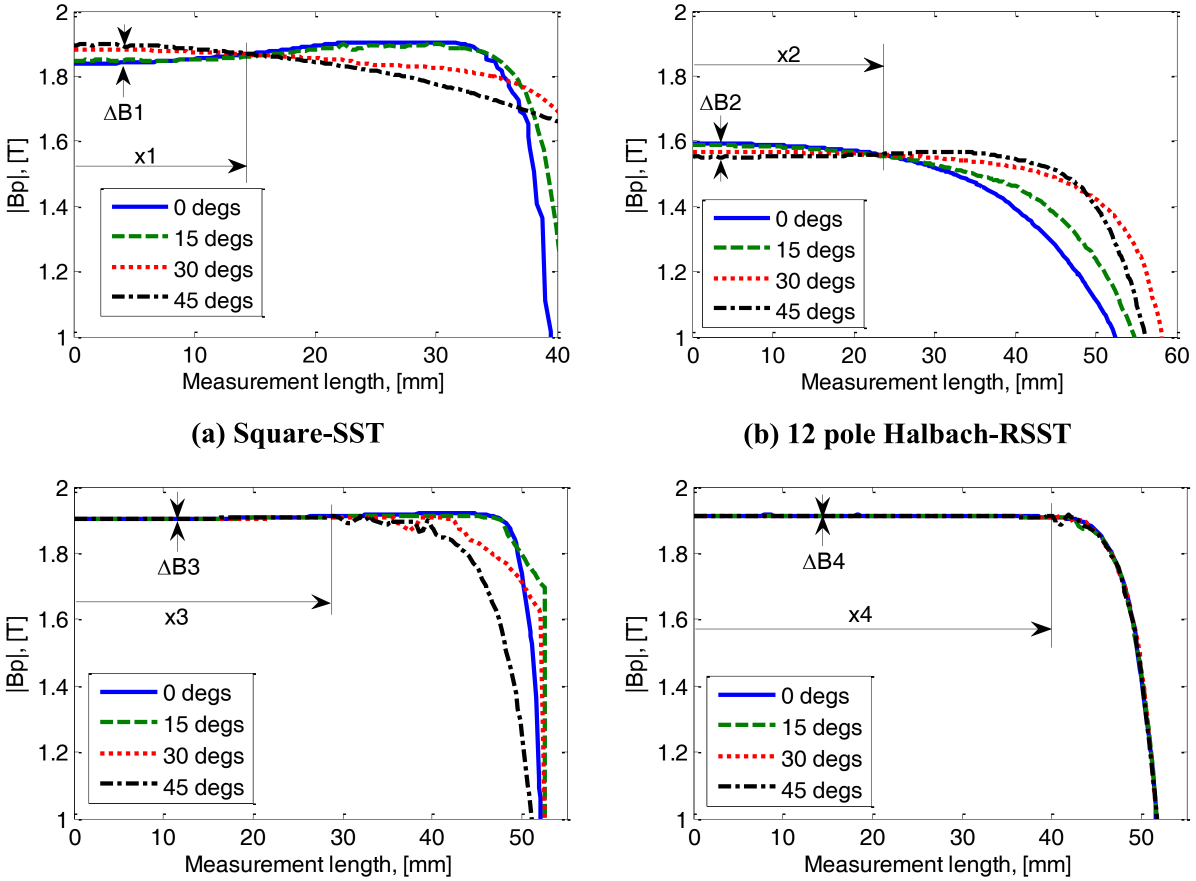

(a) Square-SST

(b) 12 pole Halbach-RSST

(c) Conventionally wound-IMRSST

(d) Sinusoidally wound-IMRSST

Fig. 2.12 Variation of the instantaneous $|B_p|$ with magnetization directions

Uniformity in flux density is twofold - within each magnetization direction (non-uniform distribution of $|B|$ in a sample for a given direction), and from one direction to another (B variation with direction). These correspond to Fig. 2.13 (a) and (b), respectively. Fig. 2.13 (a) shows the variation in uniformity within each magnetization direction for the four topologies, which were also compared with the HaRSST–200 mm model. The IMRSSTs had the best uniformities, while the HaRSST-120 mm had the highest non-uniformity in each direction.

The variation of the instantaneous average flux density ($<|B_p|>$) from one direction to another is shown in Fig. 2.13 (b). The square tester has the highest variation, with the values increasing linearly from (13,052 A/m, 1.83 T) to (18,950 A/m, 1.89 T), corresponding to the 0 ° and 45 ° directions, i.e., a mere 3 % deviation in $<|B_p|>$ resulted in a 36 % variation in $<|H_p|>$, according to

Table 2.2. This is an additional energy requirement on the power supply to meet the magnetic field asymmetry introduced by the magnetizer. This high variation in $|H_p|$ is pronounced beyond the knee of the magnetizing curve. In the linear part of the curve, the variation will not be as magnified as in saturated conditions, owing to the low H values. This argument is supported by examining the Halbach testers.

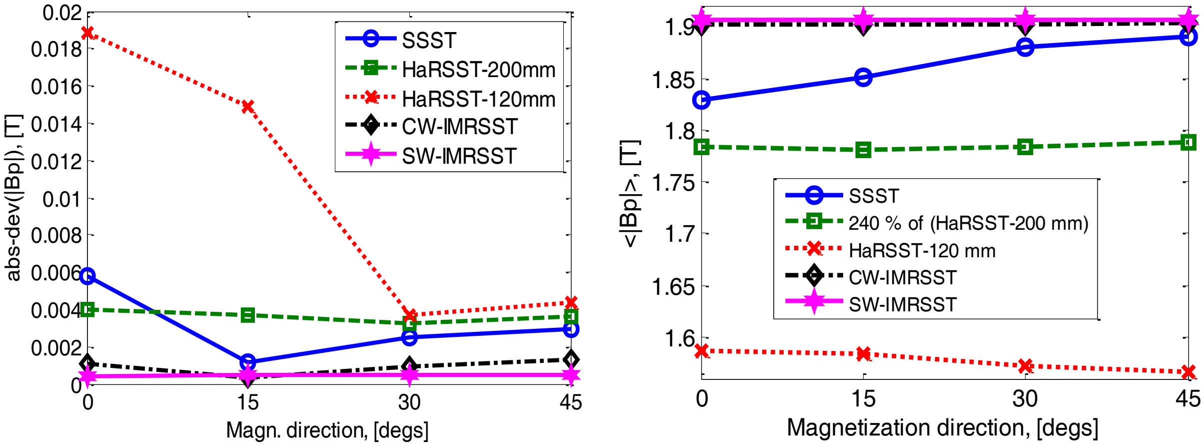

(a) Change in $|B_p|$ uniformity with direction **(b) Average $|B_p|$ vs. magnetization direction**

Note: The HaRSST-200 mm was amplified by 240 % to be at the same B level as the other cases

Fig. 2.13 Variation in $|B_p|$ uniformity and average $|B_p|$ with change in magnetization direction

The non-uniformity of HaRSST-120 mm was the highest in every direction as seen in Fig. 2.13 (a). However, in Fig. 2.13 (b), the deviation, *dev* ($<|B_p|>$) of the SSST was about 9 and 2.5 times higher, than that of the HaRSST-200 mm and HaRSST-120 mm respectively. This is because the HaRSST models had more sinusoidal MMF, and were at lower *B-H* curve operating points. That is (74 A/m, 0.74 T) and (2,874 A/m, 1.58 T), respectively, which were calculated from the average of the four directions.

Analysing the SSST and the HaRSST-120 mm cases has shown that high flux density variation is more dominant, than non-uniformity in flux density in a specific direction. Reducing the benchmark 16 pole HaRSST-200 mm model by about a half, and the airgap from 10 mm to 2 mm, doubled the achievable magnetic loading as represented by the 12 pole HaRSST-120 mm model. The former's flux density values were multiplied by a factor of 240 % in Fig. 2.13 (b) to be at the same flux density level, as the rest of the magnetizers.

In conclusion, uniformity and the flux density variation depends on the magnetizer design, the *B-H* curve operating point and the sample anisotropy. A summary of flux density variation with direction is given in Table 2.2, generated from the instantaneous $|B_p|$ and $|H_p|$ average values in the four directions.

Table 2.2 Variation of $|H_p|$ due to changes in $|B_p|$, and the impact of the yoke depth on uniformity

	SSST		**HaRSST**			**CW-IMRSST**		**SW-IMRSST**
Yoke depth **[mm]**	40	80	20	40	80	20	80	80
Sample diameter **[mm]**	80 by 80		200	120	120	105	105	105
$^{+}$***abs_dev***($|B_p|$) **[T]**	0.0226	0.0111	0.0019	0.0080	0.0045	0.0025	0.0001	<0.0001
$^{+}$***abs_dev***($|H_p|$) **[A/m]**	2,202	2,662	0	169	166	238	169	35
$^{+}$***dev***($|B_p|$) **[%]**	3.28	1.72	0.37	1.33	0.70	0.35	0.02	0.01
$^{+}$***dev***($|H_p|$) **[%]**	36.29	33.42	0.42	15.69	8.73	3.72	2.32	0.45
$<|B_p|>$ **[T]**	1.86	1.89	0.74	1.58	1.66	1.87	1.90	1.91
$<|H_p|>$ **[A/m]**	16,250	21,431	71	2,874	4,938	17,297	22,051	24,866

$^{+}$***abs_dev***(***x***) and ***dev*** (***x***) were determined using equations (20) and (21), respectively.

It is interesting to note the deviations, *dev*($<x>$) of $|B_p|$ and $|H_p|$ for the SSST, HaRSST-120 mm and CW-IMRSST cases, decreased for a yoke depth of 80 mm. This effect of deeper yokes in reducing flux density variations is analysed next.

2.5.2 Impact of a Deep Yoke on the Flux Density Variation

Increasing the yoke depth of 2-D magnetizers with non-sinusoidal magnetizing fields such as the square tester, reduces their flux density variation. The yoke depth of the HaRSST-120 mm and the CW-IMRSST, were varied in steps of 20 mm, from 20 mm to 80 mm, while 40 and 80 mm depths were analysed for the SSST. The turns per phase and the excitation currents were held constant. The results of the CW-IMRSST were extended to the SW-IMRSST. The impact of having a deep yoke is well represented using the CW-IMRSST, which had favourable results.

A longer effective axial length (deep yoke) generates a more homogeneous 3-D field over larger volumes in the interior of the yoke where the sample is placed. This improves uniformity and the magnetic loading in the measurement region as shown in Fig. 2.14 (b) vis-à-vis Fig. 2.14 (a). This is in agreement with [60] where Halbach magnetic rings were stacked to improve homogeneity.

The improvement in uniformity in each direction, resulted to a minimization in the flux density variation with a change in magnetization direction. This is represented by the gradual convergence of the instantaneous <|B_p|> values with increasing yoke depths as shown in Fig. 2.14 (c) and (d). It also results to a larger measurement region.

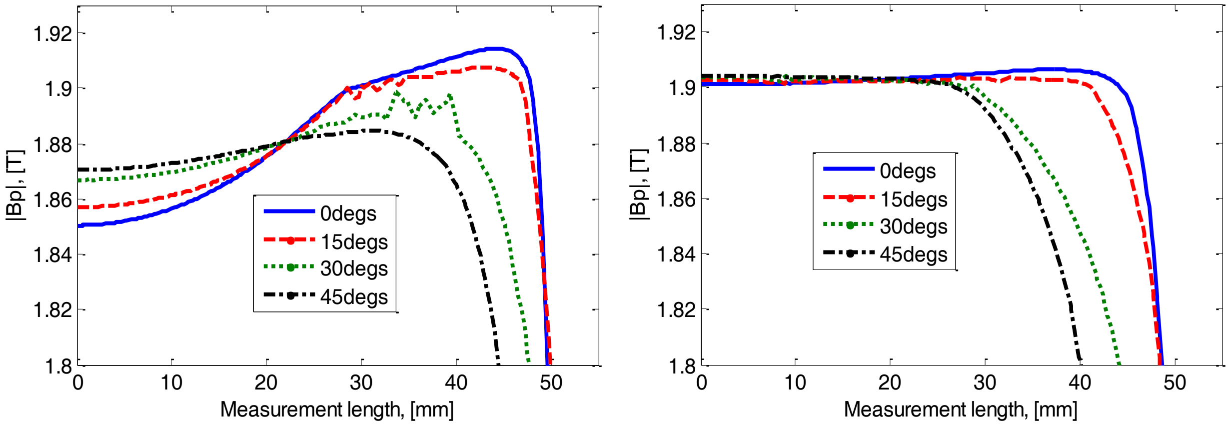

(a) High flux denity variation at 20 mm yoke depth for CW-IMRSST

(b) Reduced flux density variation at 80 mm yoke depth for CW-IMRSST

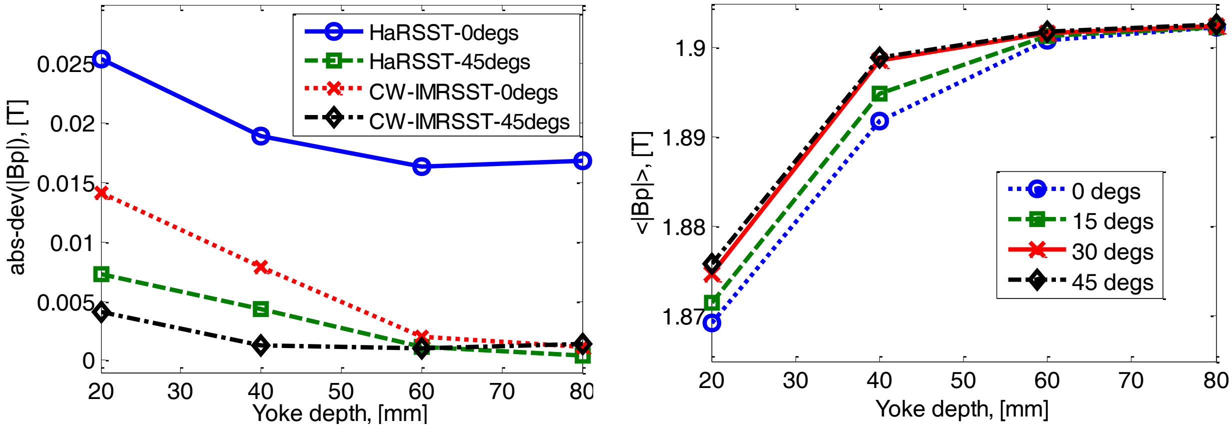

(c) Increase in uniformity with yoke depth. The HaRSST results are for 12 the pole HaRSST

(d) Convergence of <|*Bp*|> at deeper depths for the CW-IMRSST

Fig. 2.14 Improvement of uniformity and magnetic loading with increasing yoke depth

Similarly, the HaRSST-120 mm and SSST performed better with deeper yokes. For instance, increasing the yoke depth from 40 mm to 80 mm reduced the deviation in the instantaneous <|B_p|> from 3.28 % to 1.72 % for the SSST. For the HaRSST-120 mm case, the deviation in <|B_p|> and <|H_p|> were reduced from 1.33 % to 0.70 % and 15.69 % to 8.73 %, respectively. For the CW-IMRSST, *abs_dev* (<|H_p|>) was reduced by about 30 %, by increasing the yoke depth from 20 mm to 80 mm.

Another contribution of a deep yoke is the increase in the magnetic loading, which is presented using H, which shows a significant increase, as opposed to flux density values which are beyond the knee of the B-H curve. For the SSST, $<|B_p|>$ and $<|H_p|>$ increased by 1.6 % and about 32 %, respectively. For the HaRSST-120 mm, $<|B_p|>$ and $<|H_p|>$ increased by about 5 % and 72 %, respectively, and the CW-IMRSST, $<|B_p|>$ and $<|H_p|>$ increased by about 1.6 % and 27 %, respectively. These results are summarised in Table 2.2.

Therefore, deeper yokes improve uniformity, lower the flux density variation, and increases the measurement area and the magnetic loading of the sample. They also mitigate yoke effects by allowing the yoke to operate in the linear region of the B-H curve. However, it depends on the type of magnetizer as shown in Fig. 2.14 (c), where it was more effective for the CW-IMRSST case, rather than the 12 pole HaRSST case. The major setback with deep yokes is the increase in the z-component and airflux leakage fields. Based on these advantages, the recommended yoke depths for the given magnetizer parameters should be greater or equal to 60 mm.

2.6 The Proposed Rotational Magnetizer

The previous numerical analyses affirmed the advantages of a sinusoidally wound tester, over other magnetizers. Therefore, the 36 slot-105 mm sample diameter–2 mm airgap-80 mm yoke depth magnetizer was selected. The number of turns per phase and the sample size were varied to increase its frequency range and to ensure it can saturate the sample, by generating at least 30 kA/m. The number of turns per phase analysed were 386, 460, 562 and 802, while the sample sizes considered were 70, 80, 90 and 105 mm. The magnetizer size was varied proportionately to the sample size, while maintaining a 2 mm airgap.

As expected, increasing the number of turns and decreasing the sample size, increased H as seen in Fig. 2.15. As a result, inductance will increase; reducing the frequency range. The number of turns was selected as 460, which gave 25 kA/m, for a 105 mm sample diameter. This number of turns was used in the subsequent sample diameter analysis.

Reducing the magnetizer size decreased the stator teeth width; increasing their magnetic loading. It forced some of the flux to recirculate through the back yoke, instead of going through the sample resulting into magnetization asymmetry. As a result, the number of slots was decreased to 24 to widen the tooth-width in the analysis of sample diameters of less than 105 mm. This ensured there was no magnetization asymmetry introduced by tooth design. A 90 mm sample diameter could achieve a field of 30 kA/m. The FEA package extrapolated the *B* values using the permeability of free space, resulting in the flattening of the *B-H* curves after 2 kA/m in Fig. 2.15.

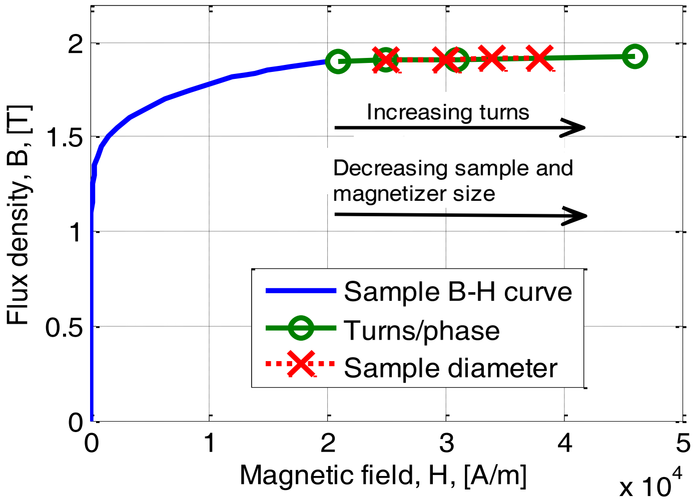

Fig. 2.15 Increasing *H* range by varying the number of turns and sample/magnetizer size

The proposed magnetizer was therefore a sinusoidally wound 2-phase 24 slot–90 mm sample diameter–2 mm airgap–80 mm yoke depth tester, which is shown in Fig. 2.16.

Fig. 2.16 The proposed 24-slot-SW-IMRSST magnetizer

It was validated by testing an M19G29, 0.356 mm thick non-oriented sample at 60 Hz, 400 Hz and 1 kHz, under rotating magnetization. The respective peak flux densities were 2.04 T, 1.72 T and 1.69 T, respectively, whose loci are shown in Fig. 2.17 (a). The aspect-ratios were 0.9863, 0.9809 and 0.9797, respectively.

The numerical *B*-locus had a magnitude of 1.93 T and an aspect-ratio of 0.9795, and was generated in steps of 10 °. The numerical and experimental *B*-loci at 60 Hz compare well, although the numerical value was underestimated by the extrapolation of B. These results also confirm the relatively wide frequency measurement range of the proposed magnetizer at very high flux densities, which can be explored beyond 1 kHz.

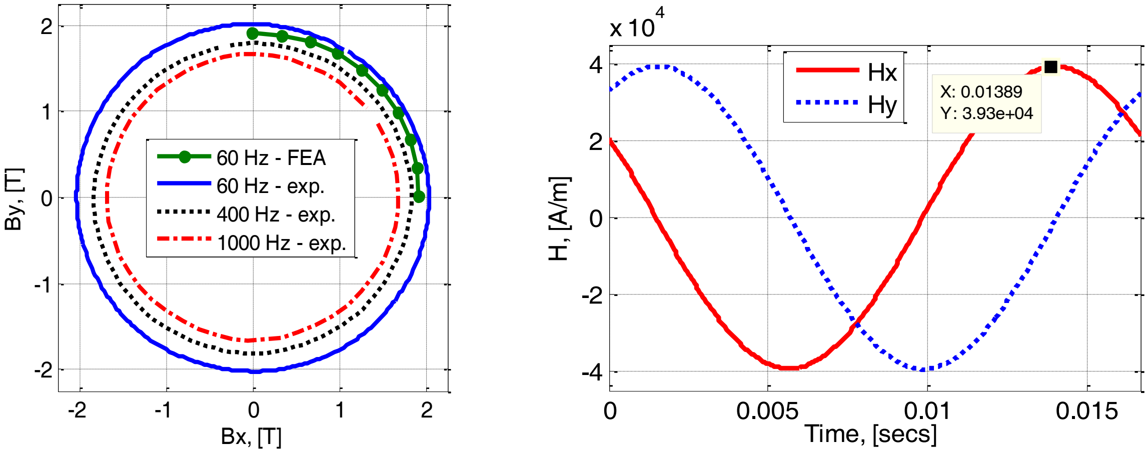

(a) Experimental *B*-loci **(b) Experimental magnetic fields at 60 Hz**

Fig. 2.17 Experimental validation of the proposed rotational magnetizer

The magnetizer was designed to achieve 30 kA/m which would ensure a flux density loading of about 2 T at 10 A, at 60 Hz. The experimental flux density was 2 T at 40 kA/m with a supply of 8 A, at the same frequency. The difference in the magnetic field results can be attributed to the difference in sample thickness, i.e., in numerical analysis 0.635 mm sample was used while in the experimental setup, it was 0.356 mm thick. Furthermore, it is difficult to fully represent the magnetic properties of a sample numerically. The ability of the magnetizer to generate very high magnetic fields; about 40 kA/m as shown in Fig. 2.17 (b) for the 60 Hz case, can be exploited in the study of lamination stacking.

The circularity of B-loci from two pairs of orthogonal B-coils, which were rotated by 45 ° with respect to each other, is used to investigate the flux density variation of the proposed tester. An M19G29 non-oriented sample was used due to its low anisotropy. Two pairs of tangential B-coils were wound at 0 ° (B_{x0degs}) and 90 ° (B_{y0degs}), for the *0 degs* pair, and 45 ° ($B_{x45degs}$) and 135 ° ($B_{y45degs}$), for the *45 degs* pair, as shown in Fig. 2.18 (a). As seen in Fig. 2.18 (b), there was good agreement in the B-loci of the two pairs of B-coils, such that the *45 degs* pair lowered the aspect-ratios by 0.6 %, 1.0 %, 0.7 % and 1.4 %, at 0.9 T, 1.2 T, 1.5 T and 1.8 T, respectively. This was with respect to the *0 degs* pair at 200 Hz, and each B-coil had five turns.

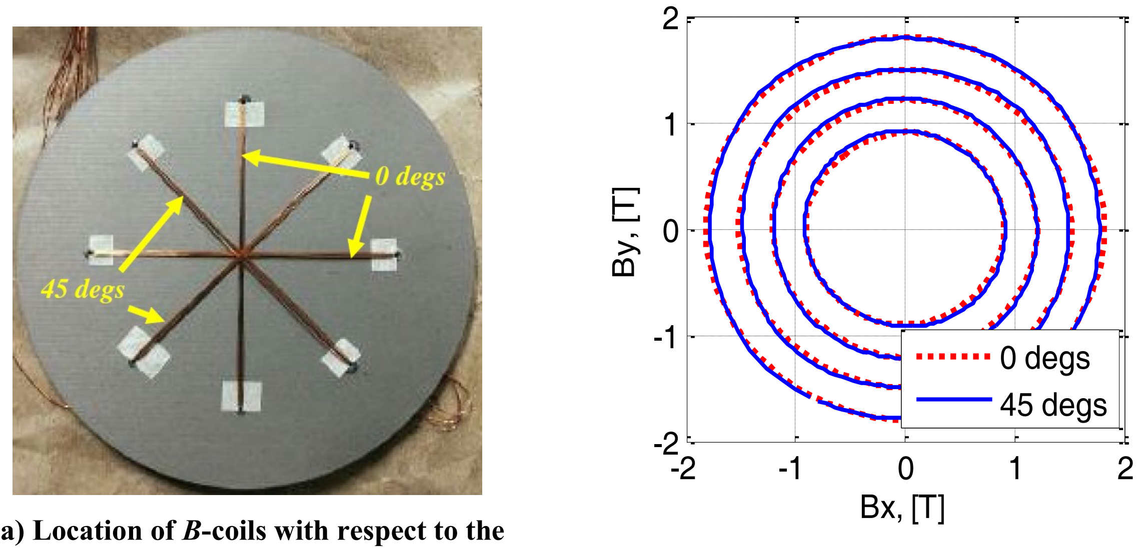

(a) Location of B-coils with respect to the rolling direction aligned with the x-axis

(b) B-loci at 0.9, 1.2, 1.5 and 1.8 T, at 200 Hz

Fig. 2.18 Circularity of B-loci with respect to the B-coil locations

2.7 Conclusion

A numerical methodology that accounts for flux leakage and eddy-currents was proposed to analyze uniformity and flux density variation, at high flux densities for 2-D rotational magnetizers. The sinusoidally wound tester reduced the flux density variation of the square tester by 92 %, by having a more sinusoidal MMF and equalizing the reluctance along the airgap. In addition, this tester had the highest uniformity and flux density level, and wider measurement area.

Increasing the yoke depth improved uniformity in the distribution of flux density in the sample, lowered the flux density variation in magnetizers with non-sinusoidal MMF, and increased the magnetic loading. It also mitigated yoke effects, which influences the magnetic field applied to the sample. Hence, a yoke depth equal or greater than 60 mm is recommended for round testers.

The experimental results at 60 Hz of 2 T at 40 kA/m of the proposed sinusoidally wound-IMRSST, validated the numerical results of 1.93 T at 30 kA/m, at the same frequency. The discrepancy was attribute to the difference in sample thickness, underestimation of flux density values in numerical analysis, and limitations in modelling all magnetic properties. It also had a relatively wide frequency measurement range at high flux densities of 2 T at 60 Hz, and 1.7 T at 1 kHz. Moreover, it was shown to have a high circularity of B, which was validated experimentally by using two pairs of tangentially wound B-coils, where the highest difference of their aspect-ratio was 1.4 %.

Finally, the proposed magnetizer extended the flux density measurement range by 43 %, and the magnetic field *H* increased from around 1.1 kA/m to about 40 kA/m at 60 Hz, in comparison to the benchmark 16 pole Halbach magnetizer.

The *H* and *B* sensors of the proposed setup are sized, and their locations are determined in the next chapter.

Chapter 3. Instrumentation

The fieldmetric measurement of core losses depends on the measurement of *B* and *H*. Consequently, the accuracy of the measurements is subject to the uniformity in the measurement region, size and location of the sensors, acquisition and processing of the signals. Therefore, it is important to consider these factors, in determining the size and location of *B* and *H* sensors.

The location of *B*-coils on a sample results to overestimation or underestimation of the measured flux density values, which directly affects the measured core loss. Experimental results will show a 14 % (at 0.8 T) and 6 % (at 1.6 T) difference between two locations of *B*-coils. *B*-holes, which are used to locate and align *B*-coils, introduce additional non-uniformity in the measurement region, and locally increase *B* and *H*. However, it will be numerically shown that *B*-holes have a minimal effect on the average *B* value; less than 1%, but the local increase in *H* is in the order of 10^4 A/m, at saturation. Therefore, averaging over a larger measurement area by use of longer *B*-coils, will be shown to minimize the impact of magnetic degradation owing to *B*-holes.

The use of Helmholtz coils to calibrate *H*-coils will be discussed, while the impact of the size of the sample measurement area will be analysed using two *H*-coil sizes. The vertical location of the *H*-coils relative to the sample surface will be shown to influence the amount of the airflux leakage field included in the measured magnetic field *H*.

The main contribution of this chapter is to show experimentally that the airflux leakage field biases the shape, amplitude and phase of the measured magnetic field. The effect of this leakage field on core losses, and *H*-loci will be analysed experimentally using three magnetizers. They are the benchmark diametrically larger 16 pole Halbach tester [45], and the proposed compact sinusoidally wound tester with 80 mm, and 10 mm yoke depths.

The compact sinusoidally wound tester with an 80 mm deep yoke, was proposed to improve the homogeneity of the fields in the measurement region, and reduce the flux density variation in Chapter 2. This was at the expense of higher airflux leakage and *z*-component magnetic fields. The larger Halbach tester and reducing the yoke depth of the proposed magnetizer to 10 mm allowed the analysis of the effect of the magnetizer parameters on these fields. The airflux leakage magnetic field is discussed at the end of this chapter, while the *z*-component magnetic field is presented in Chapter 4.

3.1 Measurement of Flux Density

The flux density is determined from the induced voltages (e_B) of the *B*-coils as:

$$B(t)=\frac{k_{cal}}{N_B A_B}\int e_B(t)dt\,, \qquad (27)$$

where N_B is the number of turns, A_B is the cross-sectional area of the *B*-coils and k_{cal} is the calibration constant. The *B*-coil method was preferred as it is applicable to both insulated and uninsulated samples, and has higher sensitivity.

B-coils can be wound around the sample, or threaded through holes made on the sample. *B*-holes affect the uniformity of the field, increase the magnetizing energy requirement and degrades local magnetic properties, which require annealing. Therefore, the effect of *B*-holes on uniformity, the location of *B*-coils, sample anisotropy, circularity of the *B*-locus and length of *B*-coils, are investigated using FEA and experiments.

3.1.1 Location of *B*-Coils

The various ways of locating *B*-coils on a sample are shown in Fig. 3.1 (a) and (b), as used in literature [35], [45], [61], [62].

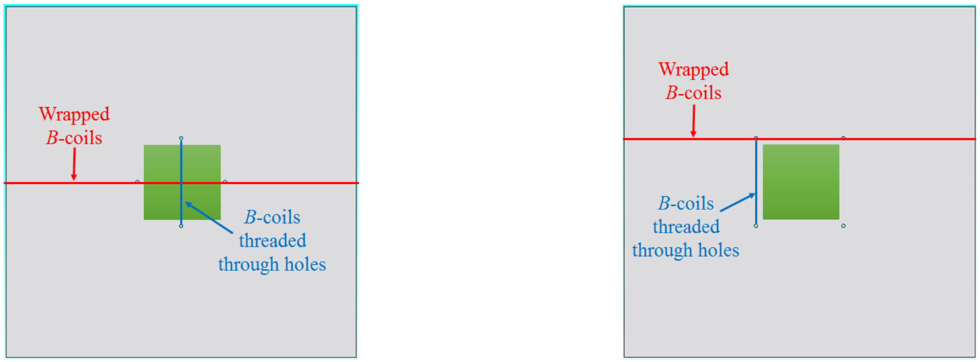

(a) Centrally placed *B*-coils **(b) *B*-coils positioned besides *H*-coils**

Fig. 3.1 The possible locations of *B*-coils on a square sample

In numerical analysis, the *B*-vector was rotated clockwise in steps of 10 ° from the *y*-axis. The regions around the *B*-holes were finely meshed by assigning a mesh size of 0.2 mm to the hole edges, whose diameter was 0.8 mm. The magnitude of the *B*-vector and its angle from the *y*-axis (the 0 ° position), are used to present the results. Only the square and sinusoidally wound testers were considered, since the square tester had the highest flux density variation, while the latter had the least.

The labelling of centered coils wrapped around and threaded through holes is *Center-Wrap.* and *Center-B-Holes*, respectively as shown by the numerical *B*-loci of Fig. 3.2. S*ide-Wrap.* and *Side-B-Holes* are *B*-coils wrapped and threaded besides *H*-coils. The type of the magnetizer and the location of *B*-coils determines the amount of non-uniformity included in the measured *B* values, owing to the non-uniform magnetization of the sample. This results to the deviation of the *B* values from those at the center of the sample (origin) as shown in Fig. 3.2, for different magnetization directions.

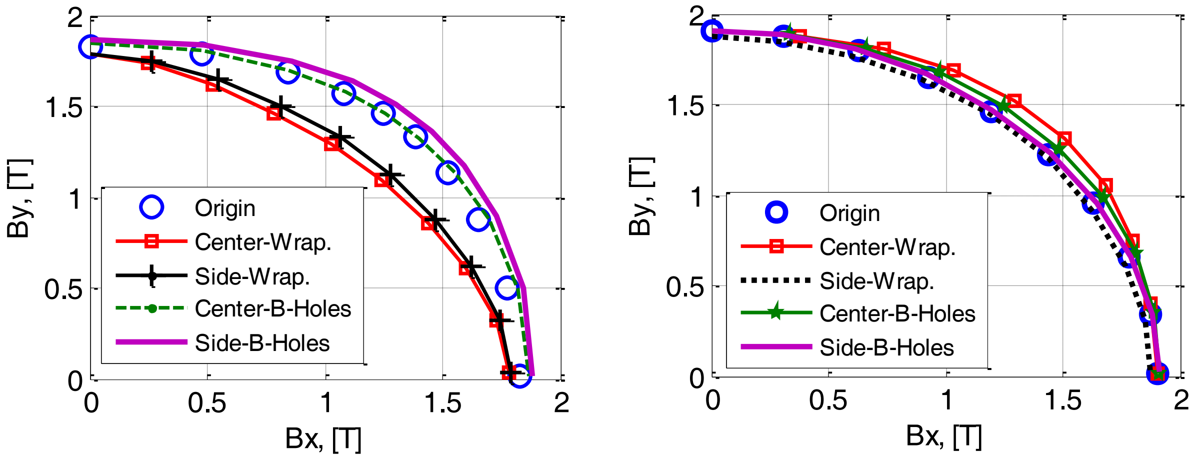

(a) Square tester **(b) Sinusoidally wound tester**

Fig. 3.2 Numerical results on the effect of the location of the *B*-coils, and the type of magnetizer, on *B*-loci

The wrapped coils in both magnetizers had the highest difference. The *B* values for the wrapped coils were lower by about 13 % at 40 ° than at the origin for the square tester, as shown in Fig. 3.2 (a). For the sinusoidally wound magnetizer, the center-wrapped coil value was higher by about 6 % at 30 °, while that of the side-wrapped coil was lower by about 2 % at 50 °, with the origin as the reference.

Threaded coils had the least difference, because they exclude the non-uniformities at the sample edges. For the square tester, the *B* values were higher by 4 % at 30 ° and 2 % at 0 ° for the side and center-threaded coils, respectively. For the sinusoidally wound magnetizer, the values were higher by 3 % at 50 °, and less than 1 % for the centered and side-threaded coils, respectively.

Although, the side-threaded coil had a lower difference than the center-threaded coil for the sinusoidally wound magnetizer, their accuracy is dependent on the location, uniformity of the sample and type of magnetizer. Therefore, center-threaded coils, which are located on the most uniform central area of the sample, are recommended.

Experiments verified the numerical results using the sinusoidally wound tester at the same current, at 60 Hz. The *B*-coils locations on an M19G29 non-oriented sample are shown in Fig. 3.3 (a) and (b) for the center and side-wrapped *B*-coils, and center-threaded *B*-coils, respectively. The numerical and experimental loci have similar trend of sandwiching the center-threaded *B*-locus by the wrapped ones, as seen in Fig. 3.2 (b), and Fig. 3.4 (b).

(a) Center and side-wrapped *B*-coils **(b) Center-threaded *B*-coils**

Fig. 3.3 *B*-coils wound on samples for analysing the effect of *B*-coil location

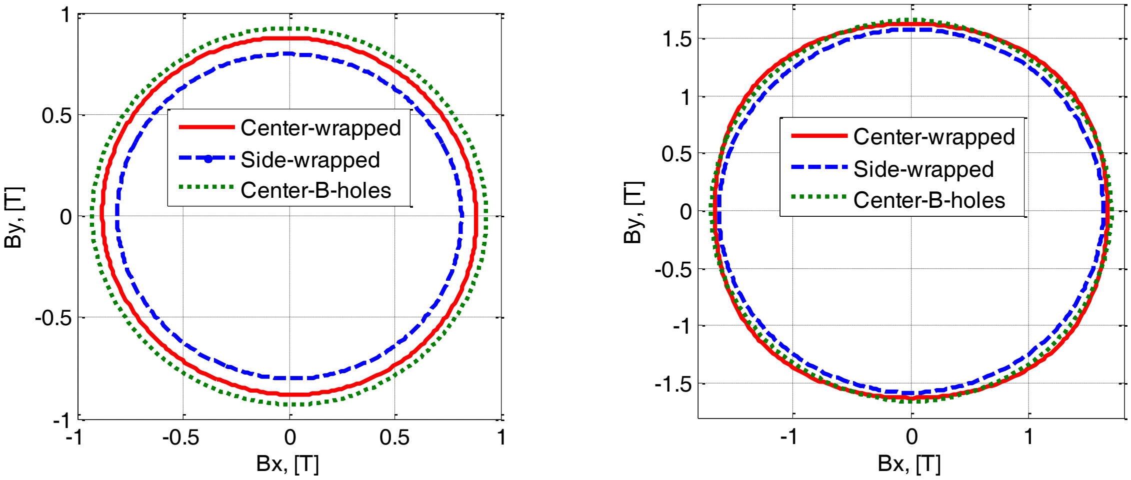

(a) $I_{mx} = I_{my} = 0.4$ A **(b) $I_{mx} = I_{my} = 2$ A**

Fig. 3.4 Experimental results based on the type and location of *B*-coils, at 60 Hz

The difference due to the *B*-coil location was more pronounced at lower flux densities of less than 1.0 T, as seen in Fig. 3.4 (a). In this case, the difference between the side-wrapped and center-threaded coils was about 14 %. At high flux densities beyond the knee of the *B*-*H* curve, this difference decreased to about 6 % as shown in Fig. 3.4 (b). This discrepancy is attributed to the uniformity of *B* in the sample, where it was more uniform at higher flux densities than at lower flux densities. This is confirmed by the higher difference of the *B*-loci below 1.0 T shown in Fig. 3.4 (a). Above 1.5 T, the loci approached the same value as seen in Fig. 3.4 (b). Therefore, at low flux densities, the center-threaded *B*-coils will give higher *B* values, than wrapped *B*-coils which enclose sample edges that are at a lower *B*.

Therefore, the location of *B*-coils and the uniformity of *B* in a sample will result to overestimation or underestimation of the measured flux density *B*, hence the measured core loss. Center-threaded *B*-coils are preferred, as wrapped *B*-coils enclose more non-uniform regions.

3.1.2 Size of the *B*-holes

A *B*-hole increases the local reluctance, which forces the flux to recirculate to its sides, increasing non-uniformity. *B*-holes also increase the magnetizing energy requirements, caused by the formation of complex domain patterns [22], and magnetic degradation. All these factors are dependent on the size of the hole. This effect is maximum when the magnetization direction (in this case the *y*-axis) is aligned with the hole, as shown in Fig. 3.5.

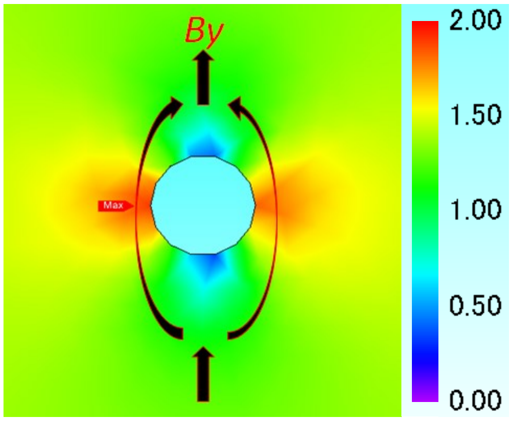

Fig. 3.5 Distribution of |*B*| in tesla [T] around a *B*-hole

Hence, numerical analysis was done along the *y*-axis magnetization direction. H_y and B_y were measured normal to the magnetization direction using lines at the surface and in the mid-section of the sample, respectively. The analysis considered 0.3 mm and 0.8 mm centrally located *B*-holes, which are used in [31], [61] and [62]. The hole edges were assigned a mesh size of 0.1 mm and 0.2 mm, respectively. The analysis was done at high flux densities where a slight change in *B* results in a large variation in H. As seen in Fig. 3.6 (a) to (b), B-holes result in the local spiking of B and H, which depends on magnetic loading. The plots are from the center of a square sample, to the edge of a B-hole.

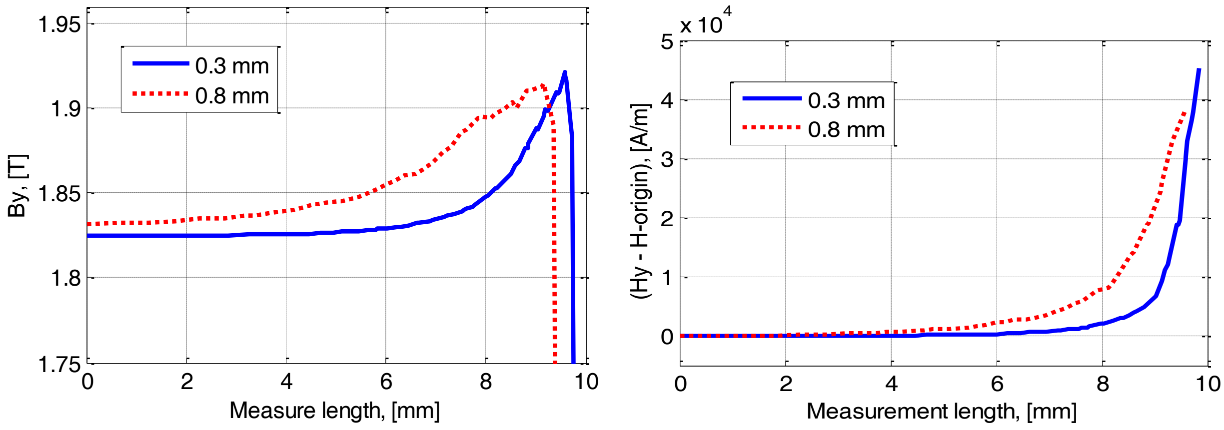

(a) Increase in B_y **(b) Deviation of H_y**

Fig. 3.6 Local increase in B and H caused by a B-hole

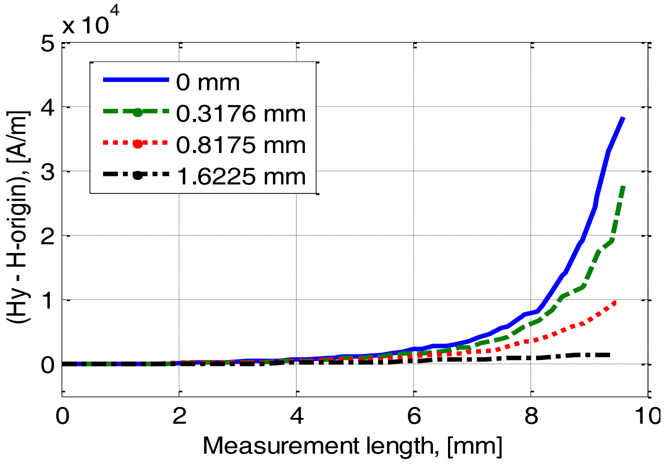

Fig. 3.7 Decrease in H_y deviation from the sample surface

The increase in the instantaneous average B values relative to the origin is less than 1 % for the two hole sizes. The instantaneous average B values were averaged from the B waveforms obtained using a measurement line between two B-holes. The slight increase in the average B might seem insignificant, but it results in very high H values at the hole edges where it is in the order of 10^4 A/m. This is an over 300 % increase in H relative to the center of the sample, as shown in Fig. 3.6 (b). This will contribute to H sensing noise, that decreases with distance from the sample surface as shown in Fig. 3.7, for the 0.8 mm hole diameter.

Non-uniformity caused by *B*-holes will have a greater effect in the testing of grain-oriented electrical steels, under rotational fields. Higher fields are needed to overcome their high anisotropy, resulting to higher deviation in *H*. Fortunately, since the effect of *B*-holes on the instantaneous average *B* values is low, *B*-coils can be made longer in order to have an allowance in the placement of *H*-coils. In addition, small diameter holes (< 0.8 mm) reduce this *H*-noise, and the regions affected by magnetic degradation. However, larger holes may be preferred because they can accommodate more turns, which reduces the misalignment of *B*-coils (by averaging the misalignments in individual turns) and increase their sensitivity.

3.1.3 Sample Anisotropy

The sample introduces inherent non-uniformity caused by anisotropy. Anisotropy results in direction dependent magnetic properties, as opposed to isotropic magnetic properties. It was modelled by scaling isotropic *H* values by 0.45 and 1.55 to get the easy (x) and hard (y) direction fields. These scaling factors were assumed from [49], for non-oriented electrical steel. The square and sinusoidally wound testers were used in this analysis, but the results can be generalized to any magnetizer.

The progression of non-uniformity with the introduction of *B*-holes, and anisotropy is depicted in Fig. 3.8, and in Fig. 3.9, for the square and sinusoidally wound testers, respectively. In the instance shown in the figures, the hard direction coincides with the magnetization direction (y-axis) and with the axis of the *B*-holes, which results to the highest non-uniformity. The first cases to the left (i.e. (a)) of Fig. 3.8 and Fig. 3.9 show the contribution of the magnetizer to non-uniformity, since their *B*-*H* curves were isotropic. The middle cases (i.e. (b)) are due to the combination of *B*-holes and isotropic *B*-*H* curves, while those to the right (i.e. (c)) are as a result of the combination of *B*-holes and anisotropy.

High reluctance causes the flux to recirculate through the easy axis (x-axis) for the combined cases of *B*-holes and anisotropy, as shown in Fig. 3.8 (c) and Fig. 3.9 (c). This lowers the aspect-ratio caused by the changing reluctance under rotational magnetization as shown in Fig. 3.10 (a). In addition, the *B*-waveforms become more non-sinusoidal as seen in Fig. 3.10 (b). The isotropic loci had higher aspect-ratios of greater than 0.98, when compared to the anisotropic loci of less than 0.71. As expected, the sinusoidally wound tester had higher circularity of *B*, which is attributed to more sinusoidal MMF, and equalization of reluctance [61], than the square tester, besides having a larger measurement area.

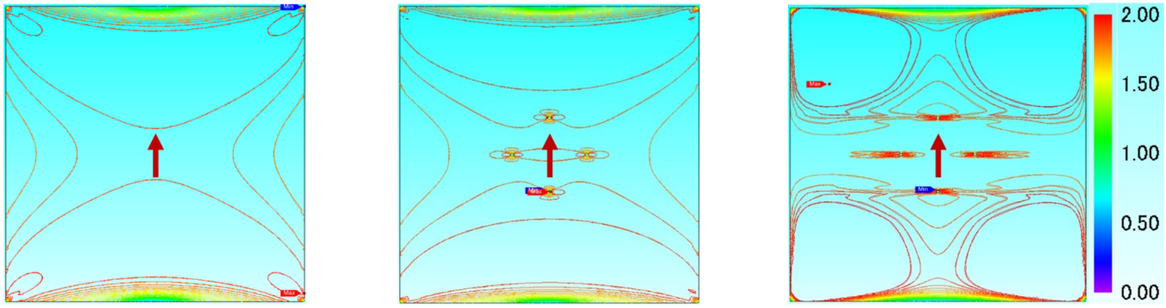

(a) Isotropic **(b) Isotropic and *B*-holes** **(c) Anisotropic and *B*-holes**

Fig. 3.8 Increasing non-uniformity with the introduction of *B*-holes and sample anisotropy, in a square sample of an SSST

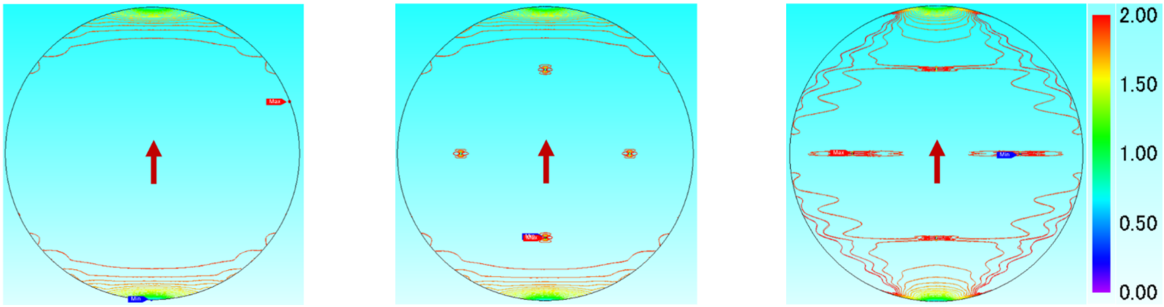

(a) Isotropic **(b) Isotropic and *B*-holes** **(c) Anisotropic and *B*-holes**

Fig. 3.9 Increasing non-uniformity with the introduction of *B*-holes and sample anisotropy, in a round sample of a sinusoidally wound-IMRSST

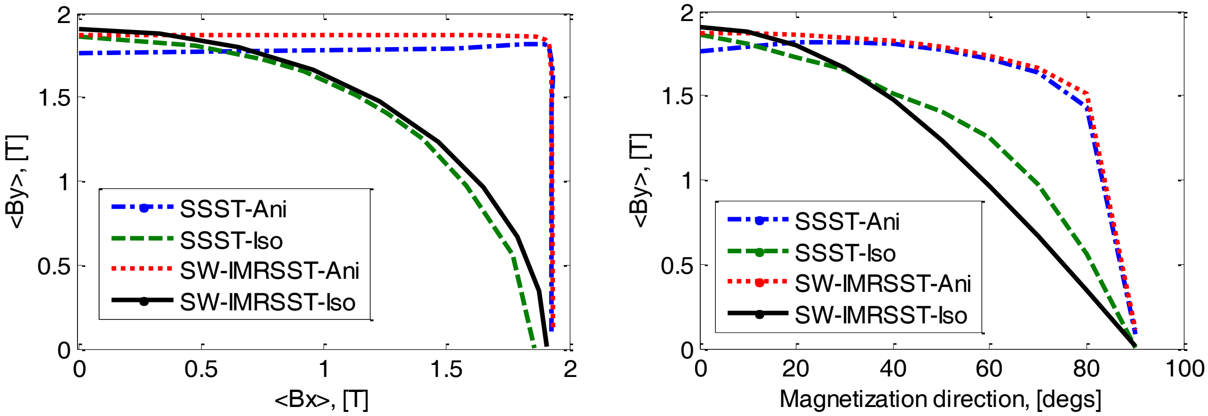

(a) *B*-loci **(b) Instantaneous average B_y**

Fig. 3.10 Numerical results on the effect of anisotropy on the circularity of *B*-loci, and *B* waveforms

The B-loci are therefore a function of the magnetizing energy (limitation of the power supply), anisotropy and type of magnetizer.

3.1.4 Length of *B*-coils

Single sheet testing is predisposed to any magnetic imperfections that might arise in the sample, in addition to magnetic degradation from B-holes. These errors can be minimized by averaging over larger sample areas, hence the need to investigate the length of the B-coils. This was done experimentally by using four B-coil lengths of 90 mm, 60 mm, 40 mm and 20 mm, as shown in Fig. 3.11.

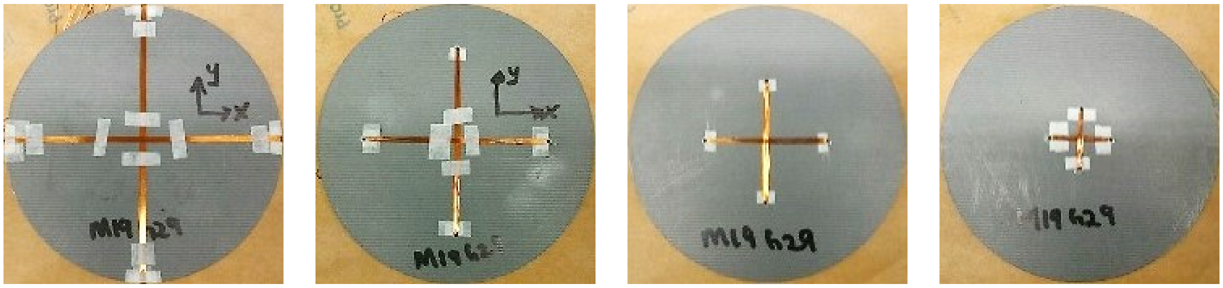

(a) 90 mm **(b) 60 mm** **(c) 40 mm** **(d) 20 mm**

Fig. 3.11 Analysed *B*-coil lengths

The B_x-coils were aligned with the rolling direction (RD), and the B_y-coil with the transverse direction (TD). Each B-coil had ten turns threaded through 1 mm diameter holes that were dependent on the laser kerf. The M19G29 non-oriented samples were laser cut from the same parent material, and there was no subsequent annealing. Hence, it was possible to investigate the degradation caused by B-holes, and show that it can be minimized by averaging over longer B-coil lengths.

Pulsating and rotating core losses determined using these B-coil lengths, are shown in Fig. 3.12. Below 1.0 T under both pulsating ($r = 0$) and rotating ($r = 1$) fields, the core losses are independent of the B-coil lengths. Beyond 1.0 T, the pulsating core losses gradually diverge and at about 1.8 T, the 90 mm length has the highest loss, followed by the 60 mm, then the 40 mm and the least is the 20 mm. The pulsating core loss difference between the 90 mm and the 20 mm B-coil lengths is about 18 %, with respect to the average of the four cases. This is because averaging over longer lengths includes more non-uniform regions, which reduced the resultant B value. This required a higher magnetizing field, hence a higher core loss value. This holds for rotating core losses between 1.0 T and 1.5 T. Above 1.5 T, the rotating core losses peak and gradually fall to a minimum. In comparison to the pulsating plots, there was a reversal of the plots beyond 1.5 T, i.e. the 20 mm and the 90 mm lengths had the highest and the least core losses, respectively.

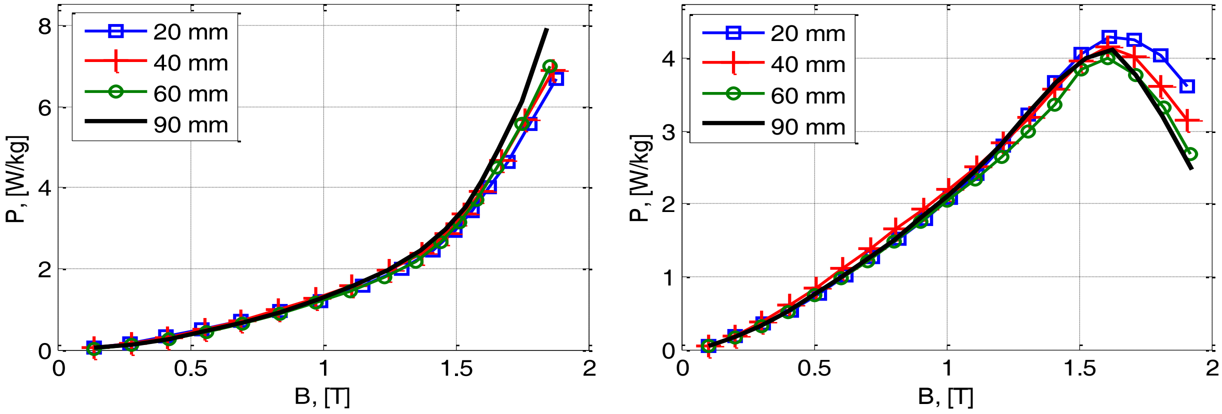

(a) Pulsating (*r* = 0) **(b) Rotating (*r* = 1)**

Fig. 3.12 Effect of *B*-coil lengths on the measured core losses, at 60 Hz

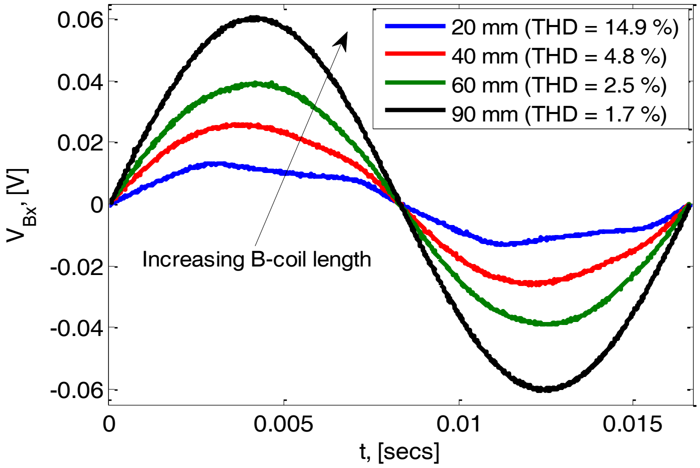

Fig. 3.13 *B*-coil voltages at 0.5 T and 60 Hz

At low frequencies under rotating magnetization, the core loss falls to a minimum as the flux density tends to saturation, as seen in Fig. 3.12 (b). Hence, the core loss component of the magnetic deterioration around the *B*-holes becomes significant, resulting to the higher loss with decreasing *B*-coil lengths, beyond 1.5 T. However, in pulsating measurements, this component is insignificant when compared to the material loss that increases exponentially with *B* as shown in Fig. 3.12 (a). Consequently, its influence on pulsating core losses is negligible.

The impact of magnetic degradation as a result of laser cutting of *B*-holes was determined using harmonic distortion of the *B*-coil voltages, as shown in Fig. 3.13, where the 20 mm length had the highest voltage distortion of 14.9 %, and the 90 mm case had the least (1.7 %).

These results are from the magnetic linear region of the sample, i.e. at 0.5 T, where the voltages are expected to be sinusoidal. Hence, for unannealed samples, the *B*-coil length should be greater than 40 mm.

In spite of this magnetic degradation by *B*-holes, they are important in ensuring *B*-coils are orthogonal. The misalignment of *B*-coils cannot be minimized by averaging of CW and CCW core losses, which is very effective in minimizing the misalignment in *H*-coils [31]. Centre-threaded *B*-coils were shown to have the least deviation of *B*, from the values at the origin of a sample. Consequently, a centered *B*-coil arrangement of 60 mm length was selected for the prototype.

3.2 Measurement of Magnetic Field

The magnetic fields were measured using calibrated *H*-coils before being used for core loss measurements, while linear Hall sensors were used to map Helmholtz coils fields, measure the *z*-component and the airflux leakage fields. The output voltage of the Hall sensors is scaled by its sensitivity and medium permeability to get the measured local field, whereas the measured field from the *H*-coils, is determined from the induced voltage $e_H(t)$ as:

$$H(t) = \frac{k_{cal}}{\mu_0 N_H A_H} \int e_H(t)dt, \tag{28}$$

where N_H is the number of turns, A_H is the cross-sectional area enclosed by the coils and k_{cal} is the calibration constant. It is difficult to wind the high number of turns uniformly out of fine wire on thin formers and hence, *H*-coils require calibration.

3.2.1 *H*-coil Calibration

Calibration was done using a known magnetic field generated by a Helmholtz coils setup. The calibration field should be of high homogeneity, and cover the entire *H*-coil volume. The desired volume was 60 mm by 60 mm by 2 mm, whose Helmholtz conditions as per Fig. 3.14 (a) are a coil radius (*R*) of 80 mm, which is equal to the distance between the two coils, z_3. Helmholtz conditions are met when the separation distance of two identical coils is equal to the coil radius, i.e. $R = z_3$ as in Fig. 3.14 (a). The realizable coil radius was 69.25 mm based on an available hollow cylinder, which affected the homogeneity of the calibrating field. The cylinder was wound with 84 turns per coil (N_{coil}), and the final coil separation distance z_3 was 80 mm. The fabricated Helmholtz coils setup is shown in Fig. 3.14 (c).

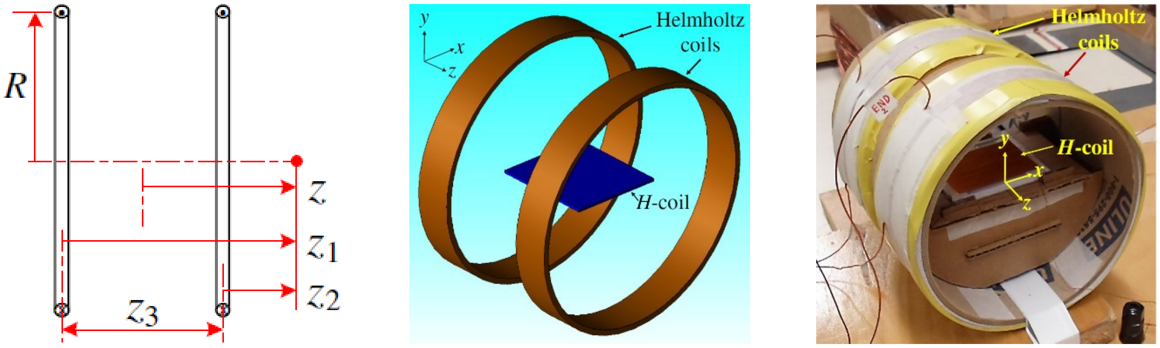

(a) Parameters **(b) 3-D FEA model** **(c) Fabricated setup**

Fig. 3.14 The Helmholtz coils setup used to verify Hall sensors and calibrate *H*-coils

The fabricated Helmholtz coils setup lowered the homogeneity which was evaluated using standard deviation, σ. For the desired setup with $R = z_3 = 80$ mm, $\sigma = 5.03 \times 10^{-6}$ A/m. For a setup based on the available cylinder and meeting Helmholtz conditions, i.e. $R = z_3 = 69.25$ mm, $\sigma = 9.88 \times 10^{-6}$ A/m, and for the fabricated setup whose $R = 69.25$ mm, and coil separation distance, z_3 was 80 mm, $\sigma = 6.30 \times 10^{-6}$ A/m. These standard deviations were analytically determined using equation (29) along the axis of the setup on a 60 mm measurement line.

Five sensors were randomly selected from twenty-four EQ-730L Hall sensors of 128 mV / mT sensitivity, with a linear measurement range of ± 13 mT (about ± 10 kA/m) [63]. The twenty-four sensors were compared in terms of magnitude and phase-shift, where one sensor was used as a reference at the same current. Their standard deviations in terms of fundamental magnitude (A_{n1}/A_{ref1}) and phase-shift ($\phi_{n1} - \phi_{ref1}$) were 4.00×10^{-4} and 0.0296 °, respectively. The five Hall sensors were then aligned with the axis (z-axis in Fig. 3.14 (c)) of the Helmholtz coils to measure the main axial component. The spacing between them was 10 mm. A comparison was then done with numerical (H_{FEA}) and analytical ($H_{\mathrm{analy.}}$) results at the center of the setup. The numerical results were generated using the 3-D FEA model shown in Fig. 3.14 (b) of the fabricated Helmholtz coils and *H*-coils, while the analytic value was expressed as [64]:

$$\left.\begin{aligned} B &= \mu_0 \frac{N_{coil} i}{2}\left(\frac{R^2}{\left(R^2+z_1^2\right)^{3/2}}+\frac{R^2}{\left(R^2+z_2^2\right)^{3/2}}\right)\\ z_1 &= z+\frac{z_3}{2},\ z_2 = z-\frac{z_3}{2} \text{ and } H_{analy} = \left.\frac{B}{\mu_0}\right|_{z=0} \end{aligned}\right\}. \tag{29}$$

The results of the verification of the Hall sensors are given in Table 3.1, where the third Hall sensor, $Hall_3$ located at the center of the Helmholtz coils was used for calibration. Its calibration factor was assumed for the rest of the Hall sensors, based on the low variance ($\sigma^2_{A_{n1}/A_{ref1}} = 1.60\times10^{-7}$ and $\sigma^2_{\phi_{n1}-\phi_{ref1}} = 8.76\times10^{-4}$) of the 24 Hall sensors. The average of the Hall sensor calibration factor, k_{Hall} was 0.996543, at 60 Hz, which was assumed to be unity. Hence, the sensitivity of Hall sensors was verified as 128 mV / mT.

Table 3.1 Verification of the Hall sensors using Helmholtz coils, at 60 Hz

I_{rms}, (A)	H_{FEA}, (A/m)	$H_{analy.}$, (A/m)	$Hall_1$, (A/m)	$Hall_2$, (A/m)	$Hall_3$, (A/m)	$Hall_4$, (A/m)	$Hall_5$, (A/m)	$k_{Hall} = H_{FEA} / Hall_3$
0.50	557	561	564	561	558	559	563	0.999573
1.00	1,113	1,120	1,128	1,121	1,115	1,117	1,124	0.998579
1.50	1,670	1,680	1,696	1,686	1,676	1,680	1,691	0.996126
2.00	2,227	2,241	2,265	2,254	2,240	2,247	2,259	0.994239
2.50	2,783	2,800	2,830	2,817	2,800	2,806	2,824	0.994197

The field map of the fabricated Helmholtz coils setup was then generated at 0.5 A, and 60 Hz as shown in Fig. 3.15.

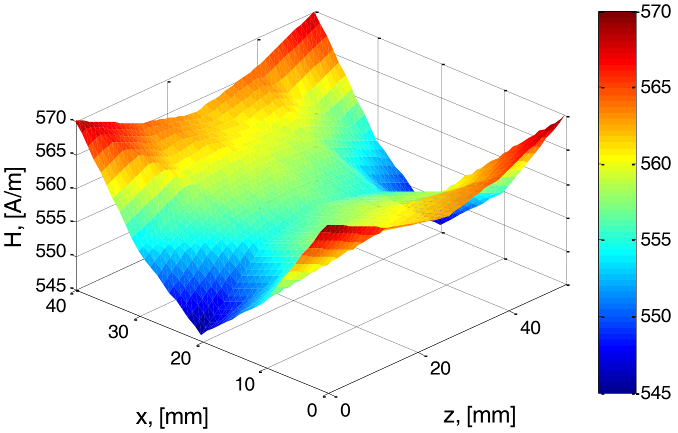

Fig. 3.15 Helmholtz coils field map generated at 0.5 A and 60 Hz

Its standard deviation is 6.9739 A/m, which is higher than that along the main axis (z-axis) of the coils setup. It was a result of using shorter coil radius than the desired, and not meeting Helmholtz condition. However, it was minimized by numerically modelling the actual fabricated Helmholtz setup, and the actual H-coil core sizes, which were then used as the reference in the calibration process. The normal component of the magnetic field to the enclosed area was averaged over the entire volume of the core to get H_{FEA}, while the analytical field ($H_{\mathrm{analy.}}$) was evaluated at the center of the setup.

Two H-coil sizes were made, and each size had a pair of coils for measuring H in the x and y directions. The first set of coils had 220 turns wound on a 53 mm × 43 mm × 1.6 mm core, and the second had 180 turns wound on a 30 mm × 30 mm × 1.4 mm core. The cores were non-magnetic and non-conductive, while the diameter of the copper conductors for both B and H coils was about 0.2 mm (AWG 34). The calibration results of the four H-coils are tabulated in Table 3.2, at 60 Hz for the two sets of coils.

Table 3.2 Calibration of *H*-coils, at 60 Hz

(a) 220 turns; 53 mm × 43 mm × 1.6 mm core

I_{rms} (A)	H_{FEA} (A/m)	$H_{\mathrm{analy.}}$ (A/m)	$H\mathrm{coil}_1$ (A/m)	$H\mathrm{coil}_2$ (A/m)	$k_{cal\text{-}1}$	$k_{cal\text{-}2}$
0.50	559	561	669	645	0.835623	0.867087
1.00	1,117	1,120	1,342	1,302	0.832902	0.858185
1.50	1,676	1,679	2,019	1,946	0.830238	0.860849
2.00	2,235	2,240	2,681	2,592	0.834024	0.861970
2.50	2,794	2,800	3,354	3,235	0.833039	0.863730
Average of the calibration constant					**0.833165**	**0.862364**

(b) 180 turns; 30 mm × 30 mm × 1.4 mm core

I_{rms} (A)	H_{FEA} (A/m)	$H_{\mathrm{analy.}}$ (A/m)	$H\mathrm{coil}_3$ (A/m)	$H\mathrm{coil}_4$ (A/m)	$k_{cal\text{-}3}$	$k_{cal\text{-}4}$
0.50	550	552	601	588	0.914619	0.936076
1.00	1,102	1,106	1,207	1,203	0.912856	0.915856
1.50	1,656	1,662	1,838	1,825	0.901404	0.907440
2.00	2,213	2,221	2,467	2,439	0.898580	0.905441
2.50	2,765	2,775	3,092	3,062	0.895257	0.902109
Average of the calibration constant					**0.904543**	**0.913384**

3.2.2 Size of *H*-coils

The flux density distribution in a sample is usually non-uniform. Hence, the area occupied by *H*-coils should influence the measured core losses. Therefore, the two sizes of the already calibrated *H*-coils were used in the measurement of pulsating ($r = 0$) and rotating ($r = 1$) core losses. The coils are shown in Fig. 3.16.

Fig. 3.16 Two *H*-coil sizes of 30 mm by 30 mm by 1.4 mm of 180 turns, and 53 mm by 44 mm by 1.6 mm of 220 turns

The smaller *H*-coil resulted in higher core losses after 1.4 T, under both pulsating and rotating magnetization as seen in Fig. 3.17. The highest differences with respect to the average of the two core losses at both pulsating and rotating conditions were: 6.6 % at 1.85 T, and 6.2 % at 1.60 T, respectively.

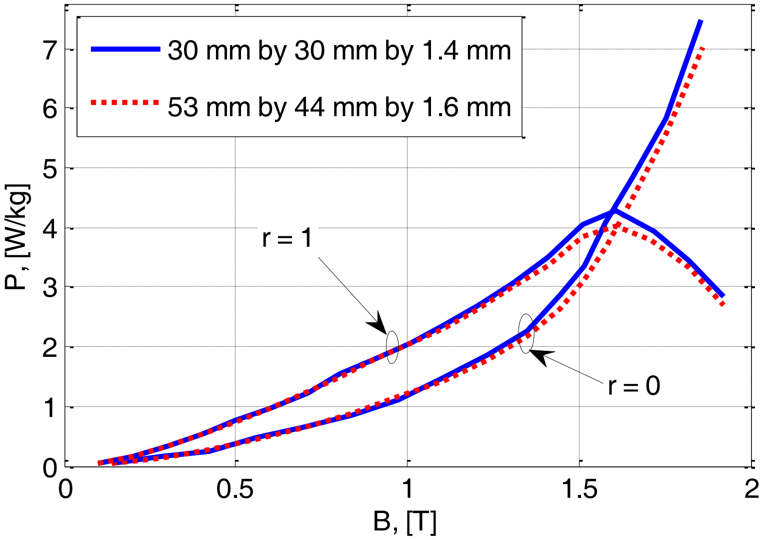

Fig. 3.17 Pulsating ($r = 0$) and rotating ($r = 1$) experimental core losses, at 60 Hz

The smaller *H*-coils were in a more uniform region, and were exposed to lower *z*-component and airflux fields. The larger coils averaged *H* over a larger measurement region, which was more non-uniform, hence lower *H*. Furthermore, the sensitivity ($N_H A_H$) difference of the two coil sizes was about 60 %, which was also equal to the difference in their measurement area. However, the near agreement of core losses from the two *H*-coil sizes is attributed to the airflux leakage field in the measured *H*. This is related to the thickness of the enclosed area of the *H*-coils, which captured more airflux fielded than necessary, making the losses independent of the measurement area. The larger *H*-coils had higher sensitivity, and less scatter, hence were selected for the setup.

3.2.3 Location of *H*-coils

Ideally, the measured *H* should be the inaccessible sample field. The continuity of the tangential fields inside the sample, and in the airflux near the sample, allows the measurement of magnetic field *H* using *H*-coils, as long as there are no surface currents along the interface [5]. Therefore, *H*-coils should be very thin and placed directly onto the sample surface. However, *H* and/or *B*-turns displace the effective area of the *H*-coils from the sample surface. This area is also deliberately made larger to increase sensitivity. This result in the inclusion of more airflux leakage field than necessary in the measured *H*, as illustrated in Fig. 3.18.

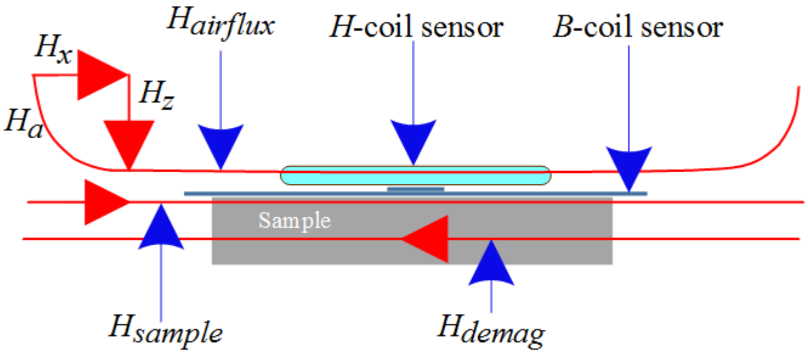

Fig. 3.18 The location of *H*-coil with respect to *B*-coil and the sample, and the associated fields

Hence, the measured *H* is the superposition of the airflux ($H_{airflux}$) and the sample (H_{sample}) fields. It will be shown that with increasing distance from the sample surface, the airflux fields approach the applied field, which is an indicator of the diminishing influence of the sample demagnetizing field (H_{demag}).

To investigate the airflux leakage field above the sample, five Hall sensors (H1 to H5) were positioned to measure the tangential component, H_x above the sample as shown in Fig. 3.19. H1 was closest to the sample surface at about 2.5 mm, and placed on top of *B*-coils. The distance between the Hall sensor centres was about 8.0 mm for a total height of 34 mm. Pulsating measurements whose sample effects are embedded on the *H*-waveforms were used, since rotational magnetization results to more sinusoidal *H*-fields at high flux densities, for non-oriented samples.

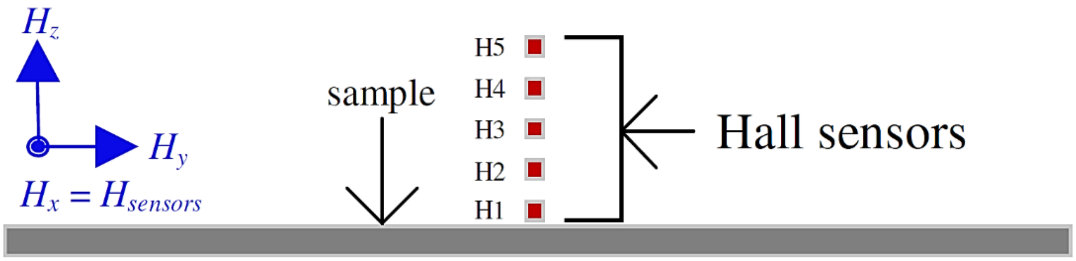

Fig. 3.19 Hall sensor locations for measuring the tangential component of the air flux, H_x

The measured airflux leakage fields as a function of magnetic loading for the sinusoidally wound tester with a 10 mm yoke depth are shown in Fig. 3.20. A yoke depth of 10 mm was used to evaluate its impact in minimizing this leakage field.

Before saturation, the magnitude and the phase-shift of the airflux field increases away from the sample surface as shown in Fig. 3.20 (a) and (b). This is caused by the opposing demagnetizing fields of the sample on the applied field. Hence, H1 has more information about the magnetization state of the sample. Further, away from the sample, the waveforms approach the airflux fields as represented by H3 to H5, in addition to the weakening of the demagnetizing fields of the sample. The need to locate *H*-coils as close as possible to the sample surface is verified.

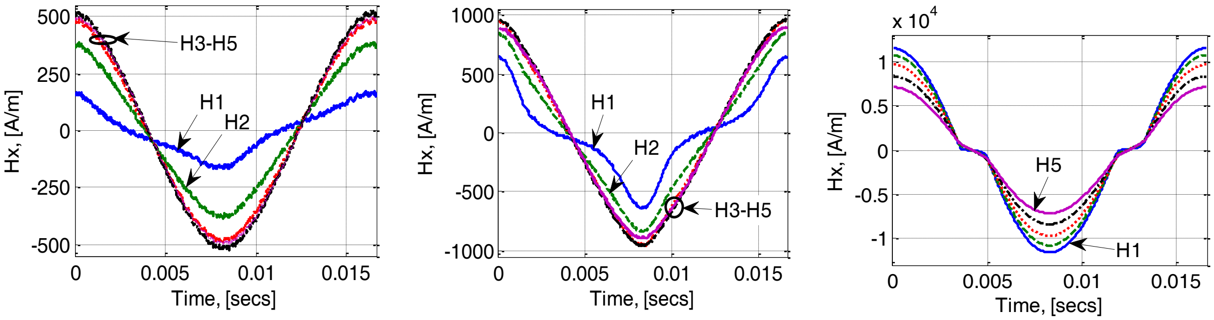

(a) 1.0 T **(b) 1.5 T** **(c) 1.8 T**

Fig. 3.20 Measured airflux leakage field above the sample of the SW-IMRSST with a 10 mm yoke depth, under pulsating magnetizations, at 60 Hz

As the sample goes into saturation ($\mu_r \rightarrow 1$), the field decreases away from the sample surface as shown in Fig. 3.20 (c). This case is similar to a magnetizer without a sample, where the field concentrates in the mid part of the yoke depth. The trend is the same for all magnetizers, as long as the yoke is thicker than the sample thickness.

The amplitudes and the fundamental phase angles of the airflux fields were used to extrapolate the peak sample field, H_s and its phase angle at the sample surface (z = 0). The peak of the H-coil field (H_c) was then interpolated at 1.5 mm; the probable location of H-coils. The phase-shifts between the field waveforms and the sample field were then determined as:

$$\Delta\phi_{af} = \phi_H - \phi_s \, . \tag{30}$$

These results are tabulated in Table 3.3 and Table 3.4 for the amplitudes and phase-shift differences, respectively.

The lag in the Hall fields with distance from the sample surface as seen in Table 3.4, is because of magnetic fields propagating faster in the sample, which is highly permeable in comparison to air. The propagation (v) of an electromagnetic wave in a medium of relative permeability, μ_r is [5]:

$$v = \frac{c}{\sqrt{u_r}} , \tag{31}$$

where c (3×10^8 m/s) is the speed of light. Therefore, as μ_r approaches that of air, the lag angle tends to zero as shown in Table 3.4 at 1.8 T and 2 T.

Table 3.3 Airflux magnetic fields under pulsating measurements, at 60 Hz

H	z (mm)	Tangential magnetic fields H_x										
		0.2 T	**0.5 T**	**0.8 T**	**0.9 T**	**1.0 T**	**1.2 T**	**1.4 T**	**1.5 T**	**1.6 T**	**1.8 T**	**2 T**
H_s, (A/m)	0	31	32	54	82	84	142	325	560	996	2,534	5,773
H_c, (A/m)	1.5	43	61	98	137	139	207	391	612	1,019	2,532	5,715
H1, (A/m)	2.5	50	79	125	170	172	247	432	645	1,029	2,524	5,664
H2, (A/m)	10.5	95	188	300	387	388	496	678	844	1,154	2,489	5,328
H3, (A/m)	18.5	116	243	385	492	492	618	802	954	1,222	2,373	4,871
H4, (A/m)	26.5	122	260	414	525	524	652	827	962	1,188	2,153	4,264
H5, (A/m)	34.5	114	248	394	501	503	619	782	898	1,090	1,895	3,671

H_s = extrapolated sample field; H_c = extrapolated H-coil field; H# = Hall sensor fields above the sample, where # = 1:5;

Table 3.4 Phase difference under pulsating measurements, at 60 Hz

$\Delta\phi_{af}$	z	Fundamental phase-shift difference, $\Delta\phi_{af} = (\phi_H - \phi_s)$										
	(mm)	0.2 T	0.5 T	0.8 T	0.9 T	1.0 T	1.2 T	1.4 T	1.5 T	1.6 T	1.8 T	2 T
H_s °	0	0.00	0.00	0.00	0.00	0.00	0.00	0.00	0.00	0.00	0.00	0.00
H_c °	1.5	-3.26	-5.77	-4.99	-4.58	-3.60	-3.56	-2.84	-1.70	-1.00	-0.23	-0.03
H1 °	2.5	-4.92	-9.59	-8.01	-7.51	-5.54	-5.84	-4.89	-2.88	-1.73	-0.37	-0.04
H2 °	10.5	-16.97	-24.57	-22.61	-19.82	-17.64	-15.65	-11.45	-7.32	-4.20	-0.95	-0.20
H3 °	18.5	-19.54	-27.36	-25.04	-21.83	-19.78	-17.45	-13.07	-8.80	-5.22	-1.33	-0.34
H4 °	26.5	-20.99	-28.41	-26.18	-22.78	-20.57	-18.34	-13.89	-9.39	-5.79	-1.62	-0.44
H5 °	34.5	-21.35	-28.86	-26.71	-23.33	-21.15	-18.70	-14.27	-9.82	-6.12	-1.77	-0.52

This lag reduces the loss angle between H and B, since H leads B; reducing the core loss as shown in Fig. 3.21, where the core loss of H2 was lower by 12 %, as compared to that of H1.

This analysis has shown that the airflux leakage field will influence the amplitude, shape and phase-shift of the measured H, which depends in the location of the H-sensors from the sample surface. In addition, the phase-shift error directly affects the loss angle between H and B waveforms as shown in Fig. 3.21, and contributes to CW-CCW core loss asymmetry. This requires calibration with a different measurement method, such as thermometric or torquemetric.

Alternatively, double H-coils [52], [65] can be used to extrapolate the sample field and correct the phase-shift, at the expense of increasing the cost of the setup, as additional simultaneously sampled acquisition ports are needed. However, single H-coils with relatively thick cores of 1.4 mm to 1.6 mm were used since the prototype was not configured to hold double H-coils.

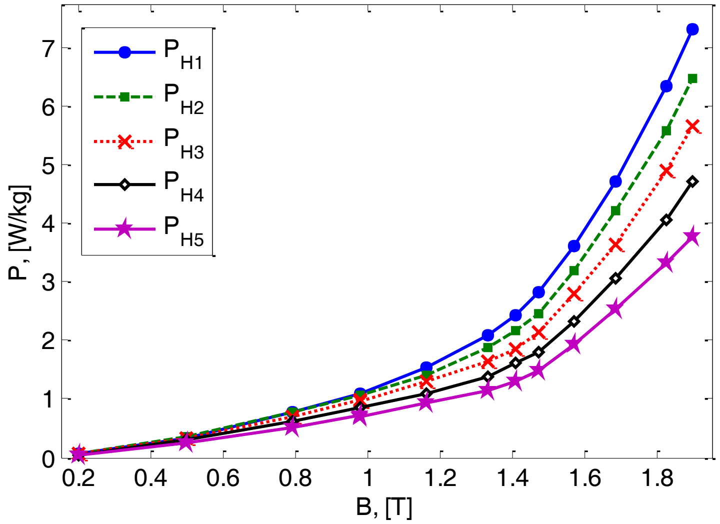

Fig. 3.21 Pulsating core losses at different Hall sensor locations above the sample, at 60 Hz

3.3 Comparison of Magnetizers in Core Loss Measurements

After determining the sizes of *B* and *H*-coils, pulsating and rotating core losses were determined at 60 Hz using the three magnetizers, shown in Fig. 3.22. The 80 mm deep yoke of the proposed magnetizer increased the *z*-component and airflux leakage magnetic fields. Hence, it was reduced to 10 mm to study its impact in minimizing the airflux leakage and the *z*-component fields, yielding the third tester. The *z*-component will be analysed in the next chapter.

(a) HaRSST-200 mm sample-20 mm airgap-20 mm yoke depth, proposed in [45]

(b) SW-IMRSST-90 mm sample-2 mm airgap-80 mm yoke depth

(c) SW-IMRSST-90 mm sample-2 mm airgap-10 mm yoke depth

Fig. 3.22 Magnetizers used in the analysis of the *z*-component and airflux leakage fields, and in the comparison of pulsating and rotating core losses, at 60 Hz

The larger Halbach magnetizer was equipped with *H*-coils of 240 turns wound on 50 mm by 50 mm by 1.6 mm formers, and *B*-coils of 180 mm length wrapped besides *H*-coils (side-wrapped) on a 200 mm diameter M19G29 sample. A 90 mm diameter M19G29 sample derived from the same parent material as the 200 mm sample was tested using the two compact magnetizers. Its *B*-coils were center-threaded and 60 mm long, while the *H*-coils had 220 turns wound on 53 mm by 44 mm by 1.6 mm formers. Therefore, any difference in the measured core losses can be attributed to the magnetizer design and airflux leakage field as a result of the *H*-coil sizes and location.

There is good agreement in the measured core losses of the two compact magnetizers as shown in Fig. 3.23, which shows the independence of the results on the yoke depth. However, the larger HaRSST magnetizer results are lower than those of the compact magnetizers below 1.0 T by 8 % for pulsating at 0.5 T, and by 9 % for rotating at 0.6 T. Above 1.0 T, they are slightly higher by 4 % for pulsating at 1.2 T, and 3 % for rotating at 1.3 T.

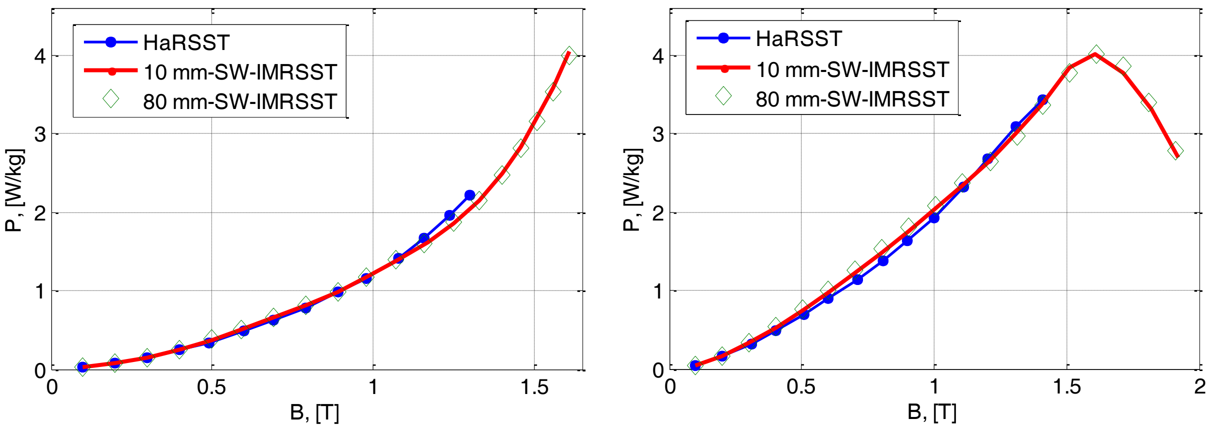

(a) Pulsating ($r = 0$) core losses at 60 Hz **(b) Rotating ($r = 1$) core losses at 60 Hz**

Fig. 3.23 Measured core losses using the three magnetizers

The larger airgap, diametrical size and moderate yoke depth of the HaRSST, led to higher reluctance, which reduced the airflux leakage field in the measured *H*, as most of the flux was channelled through its sample. Besides that, its *H*-coils were mounted on top of the sample, unlike in the compact testers, where they were on top of the *B*-coils. As a result, it had lower core losses below 1.0 T, as well as lower measured *H* than the compact magnetizers as confirmed by the *H*-loci at 0.6 T in Fig. 3.24 (a).

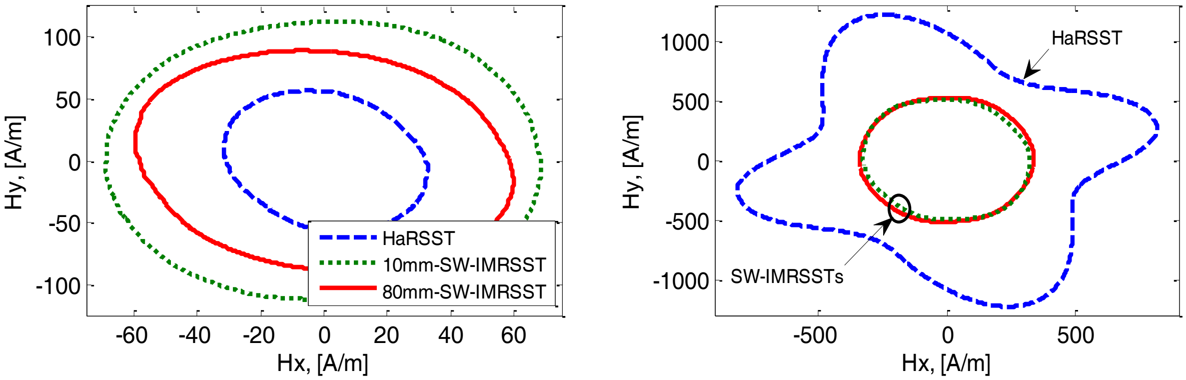

(a) 0.6 T **(b) 1.4 T**

Fig. 3.24 Counter-clockwise *H*-loci under rotating fields, at 60 Hz

Above 1.0 T, the sample goes to higher flux densities, which requires a higher applied field especially for the larger HaRSST. This explains the higher *H* (hence higher core loss) of the larger HaRSST, as compared to the compact testers in Fig. 3.24 (b), since the airflux field is higher. The influence of the airflux field, which is more sinusoidal, is also seen in Fig. 3.24 (b), where the *H*-loci of the compact magnetizers are more circular.

In the analysed compact setups, the center of the enclosed area of the *H*-coils was about 1.5 mm above the sample, which is close to H1 at 1.2 mm. For the HaRSST, it was about 0.8 mm. Therefore, the *H*-loci of the latter had more sample information embedded in the measured *H*-waveforms as shown in Fig. 3.24 (b). The location of *H*-sensors from the sample surface is therefore important, as it determines the amount of airflux leakage field included in the measured magnetic field *H*, and its content in terms of sample information.

3.4 Conclusion

The *B* and *H* sensor locations and sizes were determined, and their implications on the measured core losses were discussed. Center-threaded *B*-coils were preferred, although *B*-holes increase non-uniformity and *H*-noise. Magnetic degradation caused by *B*-holes should be mitigated by annealing, which will increase the time and cost of testing. Averaging the flux density over longer lengths (≥ 40 mm), was recommended to minimize this effect on the measured core loss. Moreover, the loss component due to magnetic deterioration was shown to affect rotating core losses more than pulsating core losses. A voltage harmonic distortion technique of analysing magnetic degradation due to *B*-holes was discussed. It is simple and cost effective, compared to microstructure imaging.

The use of a Helmholtz coils setup in calibrating *H*-coils was described in detail. The use of Hall sensors in local magnetic field measurements, supplemented the numerical analysis of the magnetizers, and it is a cost effective alternative to magnetic imaging.

The airflux leakage field above the sample was shown to influence the shape, magnitude and phase of the measured field, which contributes to loss angle error between *B* and *H*, and CW-CCW core loss asymmetry. This field is dependent on the magnetizer design, and it affects compact magnetizers more than larger ones. Its influence on the accuracy of the measured *H* and core losses was shown to depend on the displacement of the *H*-coils relative to the sample surface, and magnetizer diametrical size. Furthermore, for compact magnetizers the measured core losses were independent of the *H*-coil size (sample area occupied by *H*-coil) and the yoke depth, because of the relatively thick *H*-coil core (1.4 – 1.6 mm). The z-component magnetic field is analysed next.

Chapter 4. Mitigation of the Magnetic Field *Z*-component

The proposed sinusoidally wound rotational tester achieved very high flux density of 2 T, at 60 Hz, due to a combination of sinusoidal distribution of the MMF, a reduction in its diametrical size and a deep yoke [28], [43], [60], [66]. However, these measures increase the volumetric region under 3-D fields. Furthermore, the sample has higher permeability than the surrounding air, and it is also thin relative to the yoke depth. Hence, the flux will concentrate into it from the thicker yoke. All these factors will contribute to the *z*-component of the magnetic field (H_z), which is highest at the sample edges, and falls to zero at the center of the sample. Therefore, H_z is a function of magnetic loading and magnetizer design parameters.

This component makes the resultant airflux field (from which *H* is determined) non-tangential in the measurement region. As a result, the fieldmetric method should include the *z*-loss as:

$$P = \frac{f}{\rho}\int\left(H_x\frac{dB_x}{dt} + H_y\frac{dB_y}{dt} + H_z\frac{dB_z}{dt}\right)dt \,. \qquad (32)$$

It is difficult to measure the *z*-components on a single sheet electrical steel with a thickness of less than 1 mm. Hence, it is usually neglected. However, 3-D testers used to characterize soft magnetic composites [38], [41], [42], [67], can be used to investigate the *z*-components in laminated electrical steels, and the impact of negating the *z*-loss in 2-D fieldmetric core loss measurements.

From the numerical results of Fig. 4.1, H_z in the sample can be assumed zero (justifying the negation of the *z*-loss) but it is significant in the air region where the *H*-sensors are placed. The H_z plots were determined on the sample-air boundary along the magnetization direction, where H_z is maximum. Towards the sample edges, H_z is very high; even greater than the tangential components especially at low flux densities less than 1.0 T. Therefore, the *z*-component negation error affects compact magnetizers more than larger ones.

From these numerical plots, we can conclude that only tangential magnetic fields exists inside the sample, within the measurement region. As a result, the tangential measured field is not equal to the sample field, since the applied field (H_a) is the same at both the coil and sample locations, as:

$$H_a = f_{coil}(H_{c_x}, H_{c_y}, H_z) = f_{sample}(H_{s_x}, H_{s_y}). \tag{33}$$

H_z therefore contributes to H measurement errors that do not affect the torquemetric and thermometric methods.

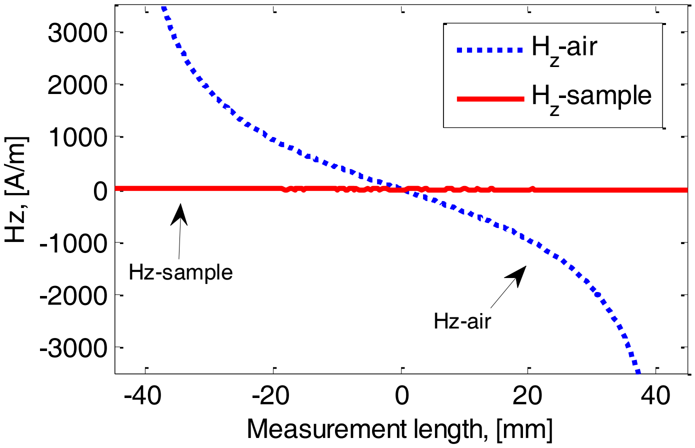

Fig. 4.1 Numerical H_z at the boundary of the sample and the air, at 0.54 T and 60 Hz, under rotating flux, for the unshielded SW-IMRSST

The magnetic field *z*-component may also contribute to CW-CCW core loss asymmetry under rotational magnetization [68]. This is significant towards saturation where the phase shift (loss angle) between B and H, goes to zero. Therefore, any unaccounted *z*-loss will contribute to this asymmetry.

The suppression of H_z using opposing fields under rotational magnetization is challenging. Electromagnetic shielding is therefore a practical option that minimizes H_z, as well as improves the homogeneity of the field [69], [70], [71]. The shields are of the same material, orientation and diameter as the sample and placed at a distance d from the sample as shown in Fig. 4.2.

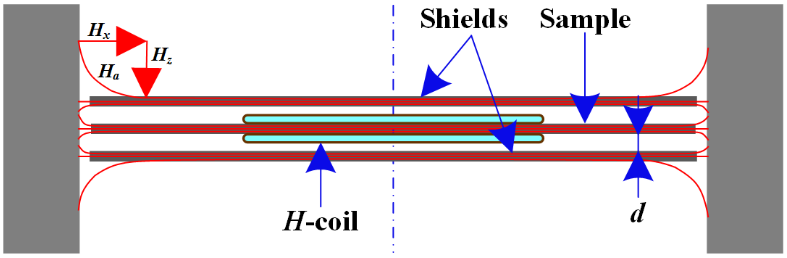

Fig. 4.2 Location of the shields, sample and *H*-coils

Skin effect, which is dependent on permeability (μ) and electrical conductivity (σ) of the shield, minimizes the effective yoke depth seen by the sample. At low frequencies, the shields permeate the field above and below the sample, whereas at high frequencies the skin depth δ_s as given in equation (34) attenuates the field.

$$\delta_s = \frac{1}{\sqrt{\pi f \mu \sigma}} . \tag{34}$$

The result, is a reduction of the field from the end sections of the yoke, reducing H_z. Shielding also increases the flux leakage at the sample and shield edges via the yoke that is dependent on the shield distance.

Shielding was proposed in [69], to improve homogeneity in a square tester; minimization of H_z was a secondary effect, which was further reduced by use of chamfered poles. The impact on H_z was not explicitly presented, and the 2-D analysis used may overestimate the effectiveness of shielding; particularly if a static solver was used without considering eddy-currents. In [70], 3-D numerical analysis accounting for eddy-currents was used to determine an optimal shield distance of 9 mm. Similarly, the effect on H_z was not explicitly presented. In these two cases, the effectiveness of the shield distance was not evaluated for the entire flux density range, nor the explicit effect on H_z presented.

Magnetic interaction also contributes significantly to H_z as was experimentally validated in [71], where two grain-oriented samples were analysed at a separation distance of 0.15 mm. Consequently, H_z increases with reducing shield distance. This interaction together with H_z contributes to CW-CCW core loss asymmetry, according to [71].

This chapter will show numerically and validate experimentally, that an optimal shield distance, at a given flux density, does not mitigate H_z evenly for the entire flux density range. Therefore, shield distances of 9 mm to 10 mm and 18 mm to 22 mm are effective at low ($B < 1.0$ T) and higher ($B > 1.0$ T) flux densities, respectively. The impact of shielding on the tangential components is also numerically investigated, as well as the dependency of H_z on magnetizer diametrical size and yoke depth. Finally, magnetic properties and interaction of the sample and shields are shown to reduce the effectiveness of shielding in deep saturation at 2 T and 60 Hz, supporting the findings in [71].

4.1 Numerical Analysis Methodology

Three-dimensional FEA and local magnetic field measurements were used to analyse the three-magnetizers shown in Fig. 3.22. They are the larger Halbach tester with a 200 mm sample, the proposed sinusoidally wound tester with a 90 mm sample, whose yoke depth was reduced from 80 mm to 10 mm, yielding the third magnetizer. Hence, it was possible to investigate the impact of the diametrical size and yoke depth on H_z.

In numerical modelling, the mesh design as described in section 2.1 was adapted for the shields. Anisotropic contributions to H_z were negated by assigning isotropic *B-H* curves to magnetic parts. Moreover, *B*-holes were not included in numerical analysis. These assumptions resulted in a difference in numerical and experimental results. Numerical analysis was done in one arbitrary magnetization direction aligned with the *y*-axis, as shown in Fig. 2.3. The figure shows the measurement line of H_z aligned with the magnetization direction, where H_z was obtained on the sample surface. Note that the peak H_z is in the direction of magnetization that lies in the *x-y* plane, and it decreases away from it.

4.2 Numerical Analysis of the Magnetic Field *Z*-component

Deep yokes will result to very high H_z as shown in Fig. 4.3 for the four models that were analysed in Chapter 2. The models are a square tester, 12 pole Halbach tester with a 120 mm sample, conventionally and sinusoidally wound testers with a 105 mm sample. An 80 mm yoke depth and 10 A phase current, was assumed for all the models.

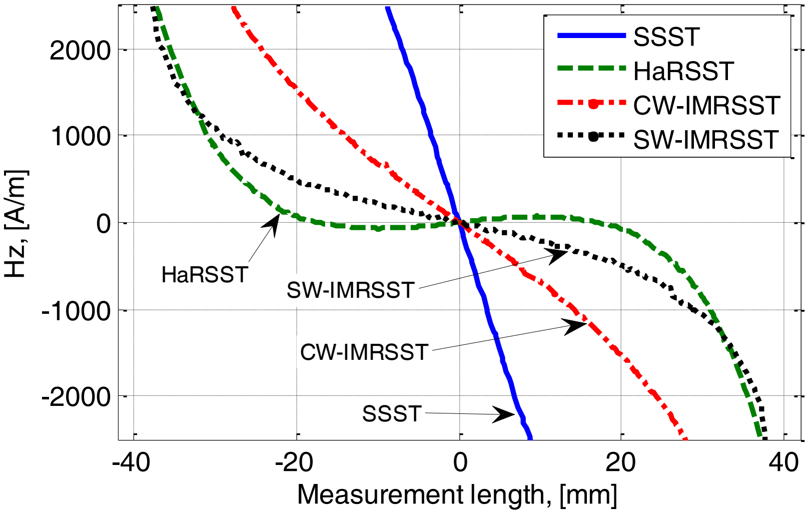

Fig. 4.3 Numerical H_z of the four models, at 10 A and 60 Hz

From Fig. 4.3, the square tester has the highest H_z, irrespective of its chamfered poles owing to its small size which magnified the impact of the yoke depth. The difference in H_z between the conventionally and sinusoidally wound tester, is that the former generated a higher triangular MMF (see Fig. 2.9 (a)) in this particular magnetization direction, hence higher H_z. But its H_z is still lower than that of the square tester. The Halbach tester had the least H_z owing to its large sample size, as well as higher reluctance because of the slot-openings in the poles, which lowered the field seen by the sample, as well as H_z.

These numerical results show a reduction in H_z in the measurement region with increasing diametrical size of the magnetizer. They also show the need to select the yoke depth based on the magnetizer size, in the mitigation of H_z. Therefore, the impact of the yoke depth on H_z for the proposed sinusoidally wound tester with 24 slots, 90 mm sample was explored further.

As shown in Fig. 4.4, decreasing the yoke depth minimized H_z, which motivated the reduction of the yoke depth of the proposed magnetizer from 80 mm to 10 mm.

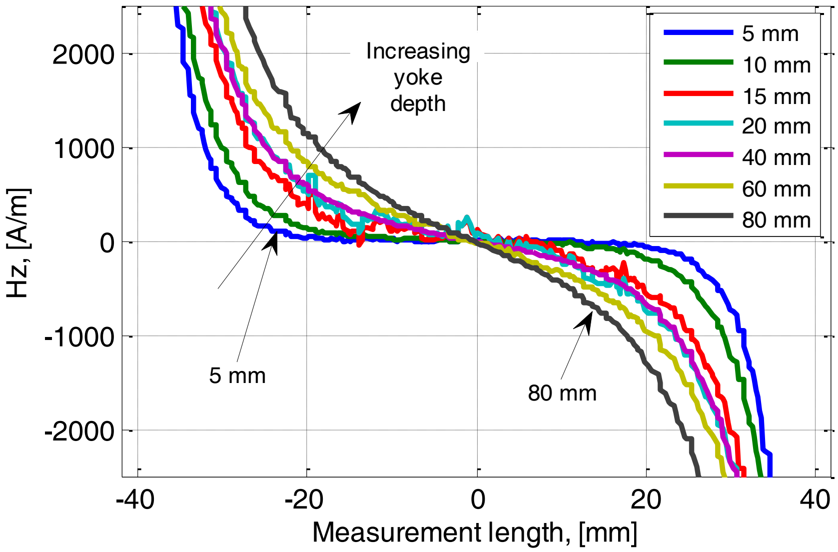

Fig. 4.4 The impact of the yoke depth on numerical H_z, at 10 A and 60 Hz

The next sub-sections examines the impact of the shield distance on H_z, and shielding on tangential fields of the proposed magnetizer with an 80 mm yoke depth.

4.2.1 Shielding Distance

The shield distance, d shown in Fig. 4.2 was varied. The analysis was done at 0.3 A and 10 A. Hence, the effectiveness of a given shield distance at both low and high flux densities was analysed. A number of shield distances were analysed; but only three cases of 2.5 mm, 9 mm and 18 mm are presented, owing to their practicality and effectiveness. The 2.5 mm shield distance was determined based on sandwiching *H*-coils between the shields and the sample. The 9 mm and 18 mm cases were more effective in minimizing H_z at different magnetic loadings. Therefore, the number of cases used to discuss the numerical results are based on these shield distances, with reference to the unshielded sinusoidally wound tester with an 80 mm deep yoke.

A. Low flux densities

At lower excitations of 0.3 A (~0.33 T), H_z was higher than H_y towards the outlying areas of the measurement region. For example, Fig. 4.5 (a) shows the plot of H_y for the 2.5 mm case ($Hy_{d=2.5\text{mm}}$), whose H_z was higher. This was similarly reflected in the unshielded, 2.5 mm and 18 mm cases. At low flux densities, shielding at too close ($d = 2.5$ mm) or too far ($d = 18$ mm) from the sample was not effective as moderate spacings of around 9 mm, which agreed with [70].

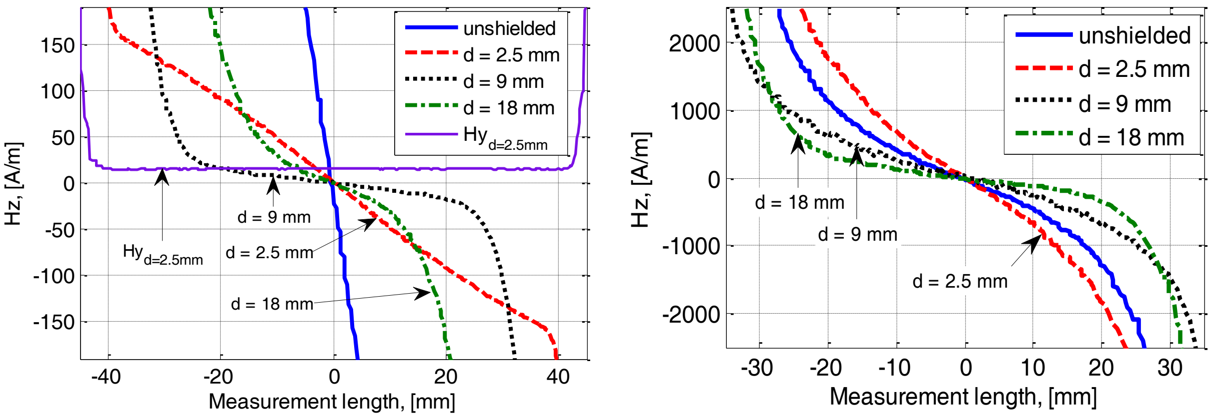

(a) $I_{mx} = I_{my} = 0.45$ A, $B = \sim 0.33$ T **(b) $I_{mx} = I_{my} = 13$ A, $B = \sim 2$ T**

Fig. 4.5 Numerical H_z at different shield distances, at 60 Hz

B. High flux densities

The effect of the shield distance, *d* on H_z at very high flux densities of about 2 T is seen in Fig. 4.5 (b). The choice of *d* is important, as it may even exacerbate the problem if the shield is closer to the sample, as illustrated by the 2.5 mm case. This is caused by a reduction of the magnetic path length of H_z between the shields and the sample, which reduces the reluctance in the *z*-direction, resulting in their magnetic interaction. This interaction excludes anisotropic effects, since isotropic *B-H* curves were assumed for numerical analysis. As the shield distance increased to 9 mm, H_z

decreased significantly compared to the unshielded case in Fig. 4.5 (b). Further increase in d to 18 mm reduced H_z, but beyond it, the decrease was not as significant, and it approached the unshielded case.

The differences in the effectiveness of a given shield distance can be elaborated further by using Fig. 4.6, at both low and high flux densities. It shows the distribution of H_z on a half section with of the model with an 18 mm shield distance.

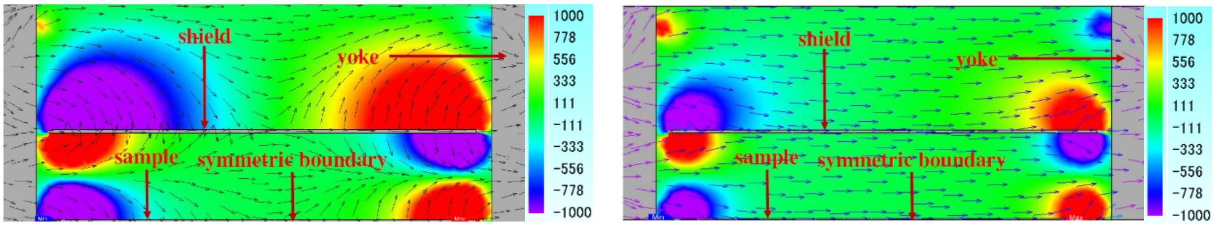

(a) H_z distribution in A/m at low flux density of 0.35 T; $I_{mx,my}$ = 0.45 A

(b) H_z distribution in A/m at high flux density of 1.98 T; $I_{mx,my}$ = 13 A

Fig. 4.6 Half section numerical distribution of H_z, at 60 Hz

At low flux densities, the permeability of the sample is higher than that of air. Hence, most of the flux will concentrate into the sample and shields as shown by the H-vectors in Fig. 4.6 (a), resulting in very high H_z in the regions close to the yoke. That is why H_z was more dominant in the unshielded case than in the rest of the cases since there was no sharing of the field. The H_z distribution of the unshielded case is similar to that of Fig. 4.6 (a), above the shield.

Shields reduce the yoke depth by sharing it (hence the field) with the sample. This lowers the regions under the influence of H_z as shown in Fig. 4.6 (a) between the sample and the shield, as compared to that above the shield. Reducing the shield distance, reduces both the volume of the regions under the influence of H_z, and the reluctance between the shields and the sample. The latter results to magnetic interaction, which is more dominant than the yoke depth in contributing to H_z, for lower shield distances of less than 9 mm. This was validated by the 2.5 mm case in Fig. 4.5 (a) and (b), which had the highest H_z. For that reason, smaller shield distances of less than 9 mm should be avoided, though they improve homogeneity of the tangential components at low flux densities, as discussed in the next sub-section.

At high flux densities, the permeability of the sample tends to that of air. Therefore, the field becomes more tangential as indicated by the H-vectors in Fig. 4.6 (b), which significantly reduces the regions under the influence of H_z as shown in Fig. 4.6 (b) in comparison to Fig. 4.6 (a). The effect of reducing the shield distance is similar to that under low flux densities.

Therefore, an effective shield distance is a balance between minimizing the effective yoke depth seen by the sample, and magnetic interaction. Larger shield distances may be preferred since they not only reduce magnetic interaction of the shields and sample, but the sample can reach higher magnetic loadings. The shortcoming of larger spacings is that their effectiveness is mostly at higher magnetic loadings.

C. Impact of shielding on tangential components

The tangential components used to generate the numerical results of Fig. 4.7 and Fig. 4.8 were H_y and B_y. The measurement lines traversed the sample diameter and were aligned with the x-axis, and were normal to the magnetization direction (y-axis). The plots are from the center of the sample to its edge, whose flatness is a rough indicator of uniformity.

At low flux densities, the uniformity of both H_y and B_y improved with decreasing shield distance, as seen in Fig. 4.7 (a) and Fig. 4.8 (a). The counter holds for higher magnetic loadings, as seen in Fig. 4.7 (b) and Fig. 4.8 (b). This shows that shielding at the optimum distances of 9 mm and 18 mm minimizes H_z, and improves homogeneity for flux densities less than, and greater than 1.0 T, respectively. However, lower shield distances of less than 9 mm are more effective in improving homogeneity, at lower flux densities as represented by the 2.5 mm case in Fig. 4.7 (a) and Fig. 4.8 (a).

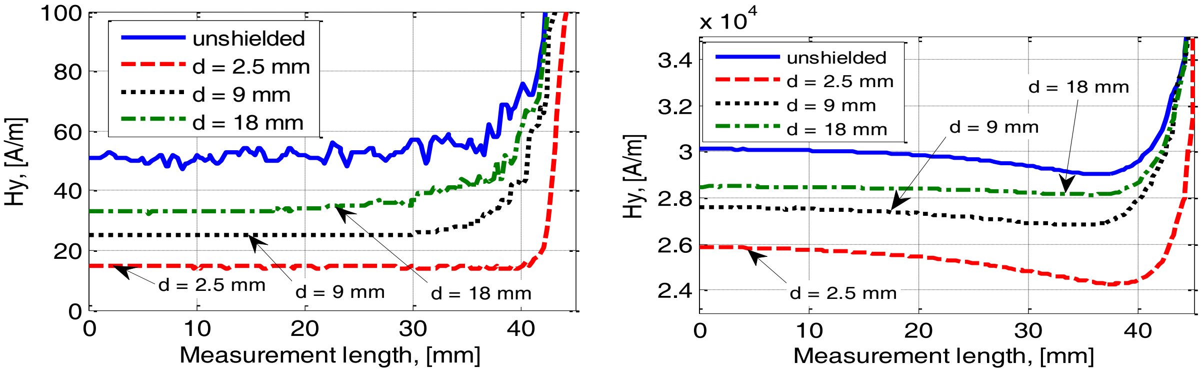

(a) $I_{mx} = I_{my} = 0.45$ A, $B = \sim 0.33$ T **(b) $I_{mx} = I_{my} = 13$ A, $B = \sim 2$ T**

Fig. 4.7 Instantaneous numerical H_y at different shield distances, at 60 Hz

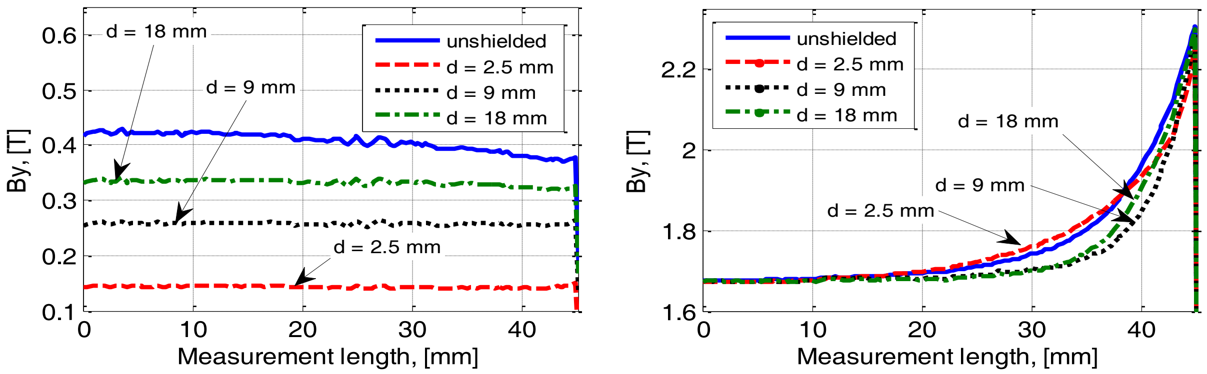

(a) $I_{mx} = I_{my} = 0.45$ A, $B = \sim 0.33$ T **(b) $I_{mx} = I_{my} = 13$ A, $B = \sim 2$ T**

Fig. 4.8 Instantaneous numerical B_y at different shield distances, at 60 Hz

The impact of the magnetizer diametrical size and yoke depth on H_z was alluded to at the beginning of section 4.2. The availability of the three-magnetizer prototypes allowed the investigation of these two parameters.

4.2.2 Impact of Magnetizer Size and Yoke Depth on H_z

The effect of the diametrical size and the yoke depth in mitigating H_z is analysed, and compared with shielding, where 9 mm and 18 mm shield distances are considered for flux density less than, and greater than 1.0 T, respectively. The curves of the unshielded SW-IMRSST with a 10 mm yoke depth are represented by the *unshld.-10mm*, while those of the shielded and unshielded SW-IMRSSTs with a yoke depth of 80 mm, are represented by $d_{9mm\ or\ 18mm}$*shld.-80 mm* and *unshld.-80mm*, respectively. Those of the larger 16 pole-Halbach tester with a 200 mm sample, are labelled as *HaRSST-200mm*. The results are with reference to the unshielded sinusoidally wound tester, with an 80 mm yoke depth.

A. Low flux densities

The larger HaRSST magnetizer had the least H_z component as shown in Fig. 4.9 (a). Its larger 200 mm sample, 10 mm airgap and moderate yoke depth of 20 mm, significantly increased its reluctance. Consequently, its H_z is very low in the measurement region (less than 2 %). Shielding at moderate spacings of 9 mm (d_{9mm}*shld.-80mm*) is similarly effective in the measurement region at low flux density of 0.5 T, as shown in the same figure. The unshielded SW-IMRSST with a yoke depth of 10 mm (*unshld.-10 mm*) was expected to significantly mitigate H_z to the same levels as the shielded cases, but as seen in Fig. 4.9 (a), its reduction is not as significant. This was attributed to its small diametrical size.

B. High flux densities

At higher flux densities, the numerical results of Fig. 4.9 (b) show that the larger magnetizer was still effective, followed by minimizing the yoke depth and shielding at a spacing of 18 mm.

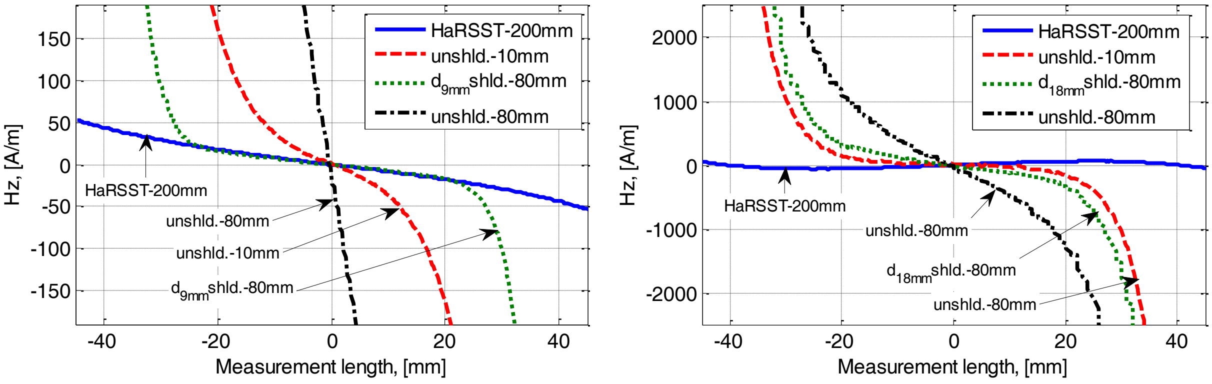

(a) $I_{mx} = I_{my} = 0.45$ A, $B = \sim 0.33$ T **(b) $I_{mx} = I_{my} = 13$ A, $B = \sim 1.88$ T**

Fig. 4.9 Impact of diametrical size and yoke depth on numerical H_z, at 60 Hz

4.3 Experimental Analysis of the Magnetic Field *Z*-component

Local magnetic field measurements of the H_z component were done under rotating magnetisation at 60 Hz using the EQ-730L® Hall sensors [63]. The sensors were attached on the sample as shown in Fig. 4.10, to measure the H_z component.

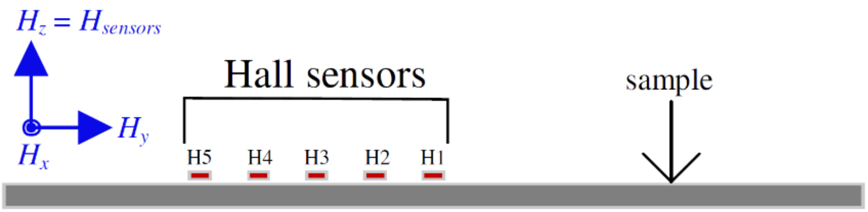

Fig. 4.10 Location of Hall sensors for measuring H_z

Shielding distances of 10 mm and 22.5 mm were considered for the sinusoidally wound tester with an 80 mm yoke depth, based on the availability of spacers. One side shield was used since the setup was not designed to accommodate the lower shield. Additionally, *H*-coils could not be positioned on the shielded side. As a result, core losses could not be analysed as a function of shield distance. However, the tangential field (H_y) was measured using a *H*-coil placed on the unshielded side. The shield was 0.71 mm thick, and of the same material, diameter and orientation as the M19G29 non-oriented sample. The experimental results of H_z were determined from the peak of the Hall sensors for one cycle, derived from the average of five cycles.

The Hall sensors were one-dimensional and were uncompensated for off the plane fields, which are tangential and higher than H_z fields, especially at high flux densities, i.e. $H_{x,y} > H_z$. Hence, there was need to estimate the effect of these fields together with noise. The results of these tests are shown in Fig. 4.11 at 0.5 T, 1.5 T and 2.0 T, measured on the unshielded sinusoidally wound tester with a yoke depth of 80 mm.

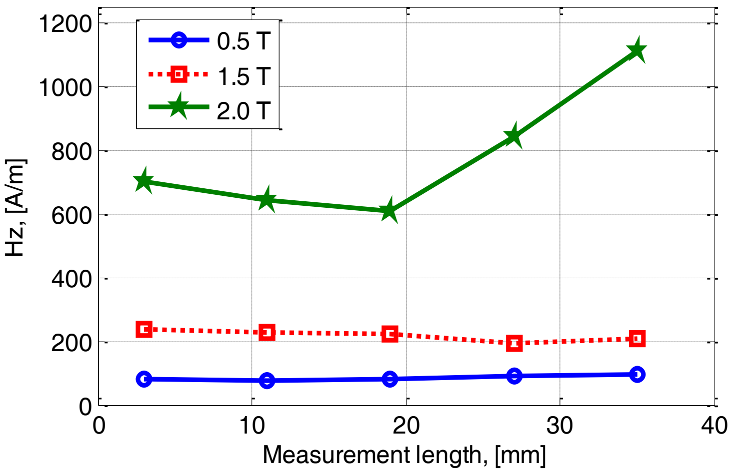

Fig. 4.11 Induced H_z by stray fields at 0.5 T, 1.5 T and 2.0 T, at 60 Hz

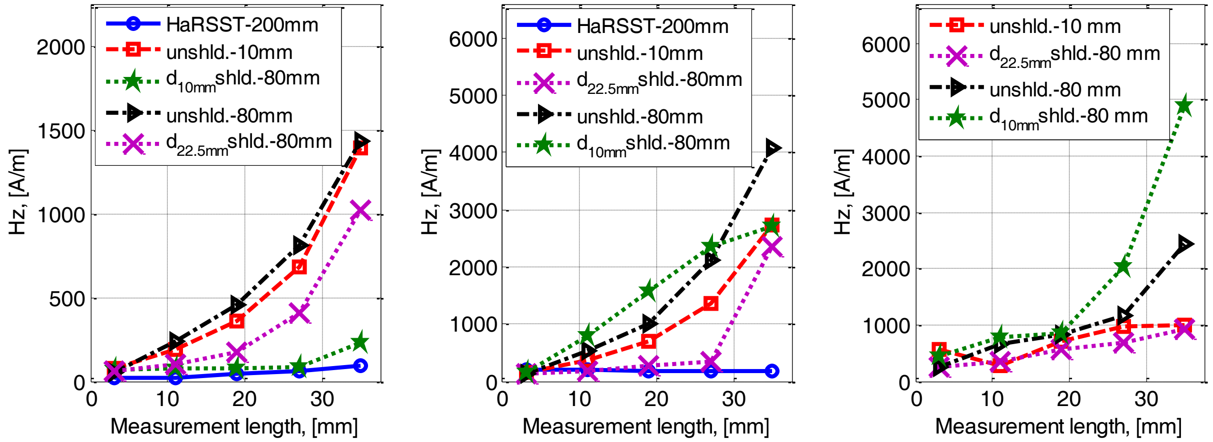

(a) 0.5 T **(b) 1.5 T** **(c) 2.0 T**

Fig. 4.12 Experimental H_z, at 60 Hz

The curves do no go to zero because of the effect of the stray fields. Comparing Fig. 4.11 with Fig. 4.12 (a) and (b) at 0.5 T and 1.5 T, show that the stray fields are neglectable. At 2.0 T, the stray fields are significant but they will not affect the discussion of the results, since the analysis is comparative and they will shift the plots with the same margin.

The measured H_z of the five analysed cases are shown in Fig. 4.12, where d_{10mm}*-shld-80mm* and $d_{22.5mm}$*-shld-80mm*, represents shielding at 10 mm and 22.5 mm shield distances of the sinusoidally wound tester with an 80 mm yoke depth. The results at 0.5 T in Fig. 4.12 (a) validate the numerical results at low flux densities (Fig. 4.5 (a) and Fig. 4.9 (a)) where the larger HaRSST magnetizer and a shield distance of 10 mm effectively minimized H_z, followed by the 22.5 mm case. However, a yoke depth of 10 mm (*unshld.-10 mm*) was not as effective. This is similarly attributed to its small diametrical size in relation to the larger HaRSST.

At 1.5 T in Fig. 4.12 (b), the larger diametrical size and shielding at 22.5 mm agreed with numerical results of Fig. 4.5 (b) and Fig. 4.9 (b) at around 2 T, whereas the 10 mm case (d_{10mm}*-shld-80mm*) had higher H_z than the unshielded reference case. This shows that magnetic contributions can even exceed those of the magnetizer design for shielding at less than 10 mm, which resulted in a difference with numerical results. Reducing the yoke depth (*unshld.-10 mm*) was still not as effective as expected, i.e., a 30 % reduction in H_z.

Hence, for the unshielded magnetizers, a larger diametrical size will mitigate H_z at the expense of sample magnetic loading. Moreover, for compact magnetizers (sample diameters $\leq$ 100 mm and airgaps $\leq$ 2 mm), their H_z and airflux leakage fields are independent of the yoke depth.

In deep saturation (2 T at 60 Hz) shown in Fig. 4.12 (c), the effectiveness of shielding at 22.5 mm and reducing the yoke depth, were diminished to 27 % and 4 %, respectively. This is attributed to magnetization process, and the magnetic interaction of the sample and shields. They contribute significantly to H_z as the material goes into higher flux density, such that for the 10 mm case, its H_z increases steeply after 20 mm to very high values. The results of the larger HaRSST are not shown in Fig. 4.12 (c), as it was limited to about 1.4 - 1.5 T, at 60 Hz.

4.4 Contribution of Magnetic Properties to the Magnetic Field *Z*-component

The contribution of sample magnetic properties to H_z was analysed using the larger HaRSST since it was least affected by H_z. Three Hall sensors are used to show the results for clarity. As seen in Fig. 4.13 (a) to (c), the magnitude of H_z increases with increasing flux density and tangential fields. Below 1.0 T, the results agreed with numerical analysis, i.e., the outer most regions towards the sample edges had higher H_z. These regions were also at higher magnetic loadings than the interior of the sample. At 1.5 T, the H_z waveforms became non-sinusoidal and approached the same magnitude, as seen in Fig. 4.13 (c).

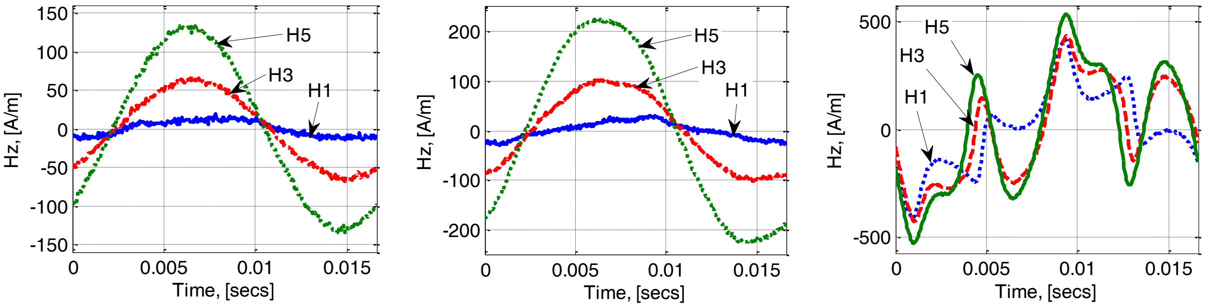

(a) 0.5 T **(b) 1.0 T** **(c) 1.5 T**

Fig. 4.13 Experimental H_z of the 200 mm sample HaRSST magnetizer, at 60 Hz

The increase in the magnitude of H_z in the inner regions of the sample at higher magnetic loadings corresponded to a more homogeneous distribution of the flux density in the sample. At these densities, the material can be said to induce its own H_z component in addition to that arising from the magnetizer design. This can also explain the reason why H_z increased towards the sample edges which are at a higher flux density than the interior. Therefore, at saturation, the H_z component due to magnetic properties and interaction of the sample and the shield become dominant, which explains the diminished effectiveness of shielding and yoke depth at 2 T and 60 Hz.

The numerical results are summarised in Table 4.1, where $H_{z\text{-max}}$ is the maximum of H_z on a 40 mm measurement line, ΔH_z is evaluated with respect to the unshielded sinusoidally wound tester, with an 80 mm yoke depth. H_y and B_y were averaged over a 60 mm measurement line. The measurement lines for all these cases were centred with respect to the diameter of the sample, to exclude the bias from the sample edges. Uniformity, *abs_dev* (H_y) was calculated from equation (20) as the absolute deviation of H_y from the average value. The experimental results are similarly summarised in Table 4.2.

Shielding at 9 mm reduced H_z to the same levels as the larger HaRSST by 98 %, which was validated experimentally as 83 %, for a shield distance of 10 mm, at 0.5 T. At high flux densities, shielding at 18 mm reduced H_z by 71 %, which was validated experimentally as 72 %, by a 22.5 mm shield distance at 1.5 T. Magnetic contributions reduced the effectiveness of shielding after 1.5 T. For example, the magnetic interaction of the shield and sample increased H_z by 58 % for a shield distance of 10 mm. Finally, the H_z component is more dominant than the tangential component H_y at flux densities less than 1.0 T, as indicated by their ratios in Table 4.2.

Table 4.1 Summary of numerical H_z, at 60 Hz

(a) $I_{mx,my}$ = 0.45 A, B = 0.33 T		***d_y (mm)**	**$^{\#}2r_s$ (mm)**	**$H_{z\text{-max}}$ (A/m)**	**ΔH_z (%)**	**H_y (A/m)**	**$^{+}abs\_dev(H_y)$ (A/m)**	**B_y (T)**
SW-IMRSST	**Unshielded**	80	90	958	-	51	1.47	0.54
	d = 2.5 mm	80	90	92	-90	15	0.17	0.16
	d = 9 mm	80	90	18	-98	25	0.15	0.26
	d = 18 mm	80	90	172	-82	34	1.13	0.35
SW-IMRSST	**Unshielded**	10	90	161	-83	33	1.37	0.35
HaRSST	**Unshielded**	20	200	18	-98	17	0.06	0.18

(b) $I_{mx,my}$ = 13 A, B = 2 T		***d_y (mm)**	**$^{\#}2r_s$ (mm)**	**$H_{z\text{-max}}$ (A/m)**	**ΔH_z (%)**	**H_y (A/m)**	**$^{+}abs\_dev(H_y)$ (A/m)**	**B_y (T)**
SW-IMRSST	**Unshielded**	80	90	1,230	-	29,871	188.06	2.00
	d = 2.5 mm	80	90	1,839	+50	25,501	269.27	1.96
	d = 9 mm	80	90	663	-46	27,352	169.55	1.97
	d = 18 mm	80	90	354	-71	28,401	65.29	1.98
SW-IMRSST	**Unshielded**	10	90	148	-88	28,367	18.63	1.98
HaRSST	**Unshielded**	20	200	18	-99	103	0.45	0.97

*d_y = yoke depth; $^{\#}2r_s$ = Sample diameter; $^{+}abs\_dev(H_y)$ calculated from equation (20)

Table 4.2 Summary of experimental H_z, at 60 Hz

$B_{x,y}$ = 0.5 T		***d_y (mm)**	**$^{\#}2r_s$ (mm)**	**$H_{z\text{-max}}$ (A/m)**	**H_y (A/m)**	**$H_{z\text{-max}} / H_y$**	**ΔH_z (%)**
SW-IMRSST	**Unshielded**	80	90	458	110	4.16	-
	d = 10 mm	80	90	78	120	0.65	-83
	d = 22.5 mm	80	90	176	96	1.83	-62
SW-IMRSST	**Unshielded**	10	90	357	96	3.72	-22
HaRSST	**Unshielded**	20	200	63	116	0.54	-86

$B_{x,y}$ = 1.0 T		***d_y (mm)**	**$^{\#}2r_s$ (mm)**	**$H_{z\text{-max}}$, (A/m)**	**H_y (A/m)**	**$H_{z\text{-max}} / H_y$**	**ΔH_z (%)**
SW-IMRSST	**Unshielded**	80	90	1,021	229	4.46	-
	d = 10 mm	80	90	156	263	0.59	-85
	d = 22.5 mm	80	90	350	238	1.47	-66
SW-IMRSST	**Unshielded**	10	90	566	182	3.85	-31
HaRSST	**Unshielded**	20	200	102	241	0.42	-90

$B_{x,y}$ = 1.5 T		*d_y (mm)	#$2r_s$ (mm)	$H_{z\text{-max}}$ (A/m)	H_y (A/m)	$H_{z\text{-max}} / H_y$	ΔH_z (%)
SW-IMRSST	**Unshielded**	80	90	998	1,619	0.62	-
	***d* = 10 mm**	80	90	1,579	2,241	0.70	+58
	***d* = 22.5 mm**	80	90	276	1,910	0.14	-72
SW-IMRSST	**Unshielded**	10	90	701	1,866	0.03	-12
HaRSST	**Unshielded**	20	200	245	2,602	0.09	-75
$B_{x,y}$ = 2.0 T		*d_y (mm)	#$2r_s$ (mm)	$H_{z\text{-max}}$ (A/m)	H_y (A/m)	$H_{z\text{-max}} / H_y$	ΔH_z (%)
SW-IMRSST	**Unshielded**	80	90	818	38,676	0.03	-
	***d* = 10 mm**	80	90	851	39,339	0.02	+4
	***d* = 22.5 mm**	80	90	554	39,430	0.02	-32
SW-IMRSST	**Unshielded**	10	90	720	45,656	0.03	-12
HaRSST	**Unshielded**	20	200	-	-	-	-

*d_y = yoke depth; #$2r_s$ = Sample diameter

4.5 Conclusion

A diametrically large magnetizer is the only way to significantly reduces H_z at the expense of the attainable flux density. Shielding is a balance between reducing the effective yoke depth seen by the sample, and minimizing the magnetic interaction of the shields and the sample, which increases H_z. Therefore, shielding at 18 mm to 22.5 mm is recommended, although for a measurement range of less than 1.0 T, shielding at 9 mm to 10 mm is as effective as larger magnetizers. Beyond 1.0 T, using a shielding distance of less than 10 mm increases H_z because of magnetic interaction, which surpasses the H_z contribution from a deep yoke and compact size.

Magnetic contributions to H_z were shown to increase with decreasing shielding distances, and increasing magnetic loading of the sample. Additionally, unshielded compact magnetizers are inherently predisposed to higher H_z components, irrespective of their yoke depths. Therefore, mitigating H_z by reducing the yoke depth in compact magnetizers is not effective (about 30 % at 1.0 T at 60 Hz) in unshielded compact magnetizers with sample diameters of less than 100 mm, and 2 mm airgap.

The complications of holding the shields, multiple effective shielding distances and the associated cost, prohibited the shielding of the proposed setup, whose performance is assessed next.

Chapter 5. Core Loss Measurement Analysis

In this chapter, the flux density and frequency core loss measurement ranges are assessed using 0.35 mm 0.65 mm thick non-oriented electrical steel samples. First, it is shown that rotational measurements are invaluable in the design of high-speed machines, where the difference between rotational and pulsating core losses is higher. Secondly, the ability of the proposed magnetizer to reproduce numerical non-sinusoidal waveforms for flux densities equal or less than 1.0 T, without any waveform control, is demonstrated. Lastly, the magnetizer limits are discussed.

In Chapter 3 and Chapter 4, the airflux leakage and the *z*-component fields were shown to be independent of the yoke depth for the proposed sinusoidally wound tester. However, the 10 mm yoke depth had a slightly lower H_z, while the 80 mm yoke depth reduces the yoke flux density operating point; hence yoke effects. These two magnetizers relatively have the same performance, as validated in Fig. 3.23 for both pulsating and rotational measurements, at 60 Hz. Subsequent core losses were measured using the proposed sinusoidally wound tester with a 10 mm yoke depth, as it was already assembled in the core loss measurement test bench. *B* and *H*-coils sizes were determined in Chapter 3, resulting in 10 turn center-threaded *B*-coils, whose length is 60 mm. The selected *H*-coils had 220 turns wound on a 53 mm × 43 mm × 1.6 mm non-magnetic core, and were calibrated using Helmholtz coils, as described in section 3.2.1.

The magnetizer can generate a rotating, elliptical or pulsating flux by controlling the magnitude ($V_{x,y}$) and phase ($\Delta\phi$) of the input voltages to its two phases as:

$$\left.\begin{aligned} v_x &= V_x \sin(\omega t) \\ v_y &= V_y \cos(\omega t - \Delta\phi) \end{aligned}\right\}. \tag{35}$$

This indirectly controls the current, hence the magnetic field, *H*.

The associated voltage signals are generated in a Simulink® model that is then built into C-code and loaded into a dSPACE® DSP platform, for use in real-time control of the *B*-locus. The dSPACE® signals are then converted into power voltage signals by the voltage controlled linear power amplifiers. The induced voltages in the *B* and *H*-coil sensors are then acquired using four simultaneously sampled ADCs, after which the fundamental flux density tangential components and their phases are computed in real-time, and used by the operator to control the *B*-locus. The *B* and *H*-coils induced voltage signals are then saved, and used in the post-processing of the core loss per cycle. The schematic of the measurement setup is shown in Fig. 5.1, as implemented in Fig. 5.2.

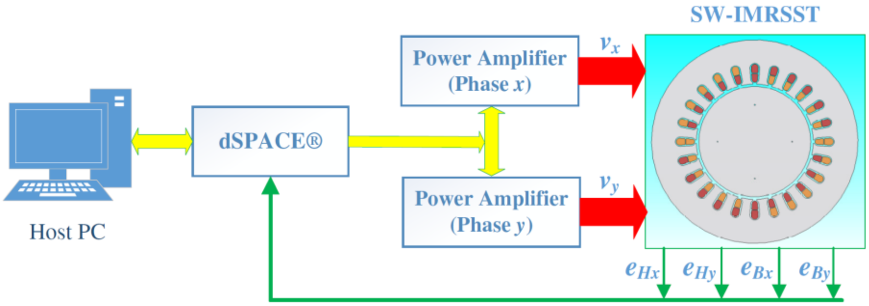

Fig. 5.1 Schematic of the rotational core loss measurement system

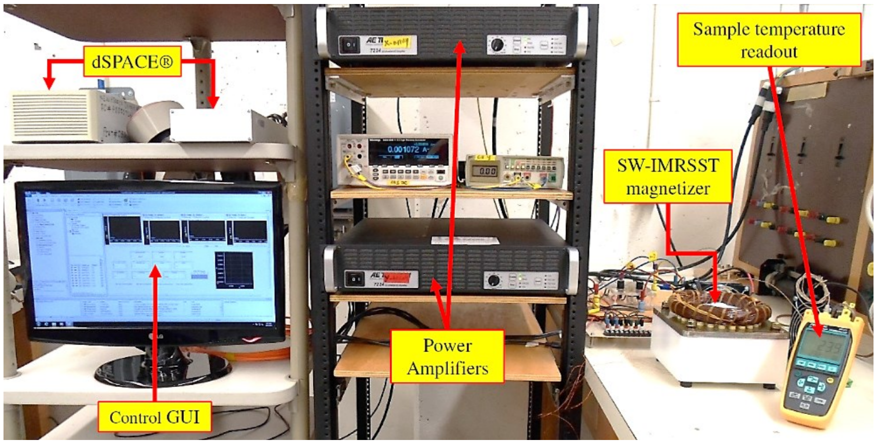

Fig. 5.2 The developed rotational core loss measurement test bench at Concordia University power engineering laboratory

5.1 Measurement Methodology

The core losses were measured under pulsating ($r = 0$), elliptical ($0 < r < 1$), and rotating ($r = 1$) sinusoidal magnetizations, at 60 Hz, 400 Hz and 1 kHz. The samples are insulated M19G29 and M19G24 non-oriented electrical steels. Moreover, non-sinusoidal measurements were done for the M19G29 sample at 60 Hz for select flux density values, to evaluate the magnetizer performance.

The following procedure, which was partly adapted from ASTM standards [72] and [73], was followed for core loss measurements at each frequency, for a given aspect-ratio (r):

i. The sample gauge and density were determined from several sample thickness and mass measurements.

ii. The sample was prepared by locating the B_x and B_y-coils and ensuring equal number of turns (10 turns) for both coils.
iii. H_x and H_y-coils were attached to fixtures such that the sample was sandwiched between them, in a sample-sensor assembly that could be rotated with respect to the magnetizer.
iv. The sample was then placed in the fixture, and the rolling direction was aligned with the x-axis of the magnetizer field. At this point, the x and y sensors were assumed orthogonal with respect to each other.
v. The sensors leads were then connected to the ADC ports, and the magnetizing circuit checked for continuity.
vi. The magnetizer was then energized to very low current values to ascertain the phases of the sensor signals.
vii. The coupling between B_x and B_y was minimized by energizing only one phase of the magnetizer, and rotating the sample-sensor assembly until the unexcited components were as minimum as possible.
viii. The sample was then demagnetized by increasing B to the highest achievable sample flux density (depends on frequency and sample thickness) for the desired aspect-ratio, and then decreased to zero.
ix. Core losses were then measured starting from 0.1 T to the highest value in steps of 0.1 T. After each step, B was reduced to zero, and then incremented to the next B value.
x. For aspect-ratio greater than zero, CW and CCW rotational core losses were measured, and averaged to get the final core loss. Temperature was also monitored.

The parameters of the two samples are given in Table 5.1, whose results at different frequencies are presented next.

Table 5.1 Parameters of the two non-oriented electrical steels

Sample	Thickness (mm)	Mass (g)	Volume (mm^3)	Density (kg/m^3)
M19G29	0.35	17.29	2162	7998
M19G24	0.65	31.27	4133	7566

5.2 Core Losses under Sinusoidal Excitation

The measurements were done for aspect-ratios of 0 to 1.0 in steps of 0.2, at the three test frequencies.

The 60 Hz results shown in Fig. 5.3 for the two samples are very similar, and their pulsating core losses ($r = 0$) increases exponentially with B. For rotational core losses ($r > 0$), the loss plots start to decrease at very high flux densities (> 1.5 T), but the drop is more pronounced for aspect-ratios ≥ 0.6. The loss goes to a minimum for rotating flux ($r = 1$).

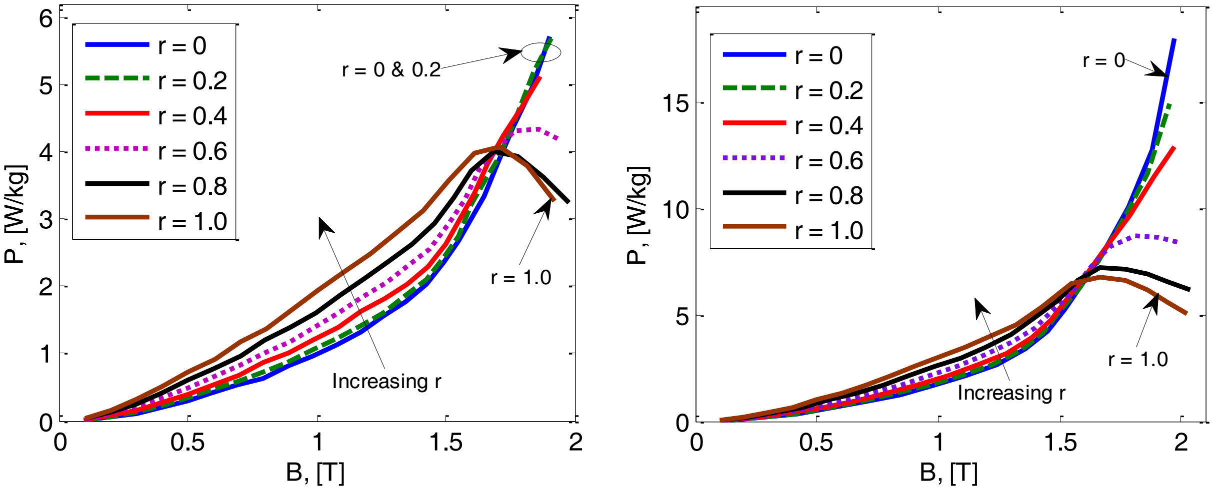

(a) M19G29 **(b) M19G24**

Fig. 5.3 Measured core losses at 60 Hz

The thicker M19G24 sample (0.65 mm) had higher losses because of a higher eddy-current core loss component, when compared to the M19G29 sample (0.35 mm), by comparing Fig. 5.3 (a) and (b). This difference owing to sample thickness will increase with frequency.

The eddy-current component, and other magnetic non-uniformities such as anisotropy, limits the minimum core loss value at high flux densities under rotating ($r = 1$) magnetization. At 400 Hz and 1 kHz, the trend of the core loss plots is similar to that of 60 Hz, but the peaking and decreasing of rotating core losses, is not as distinct. This is evident by comparing the core loss results at 60 Hz, 400 Hz and 1 kHz, in Fig. 5.3, Fig. 5.4 and Fig. 5.5, respectively. The high frequency results shown that with a higher capacity power supply, and good thermal management, their loss plots will be similar to those of 60 Hz. Hence, this rotational phenomenon is independent of frequency.

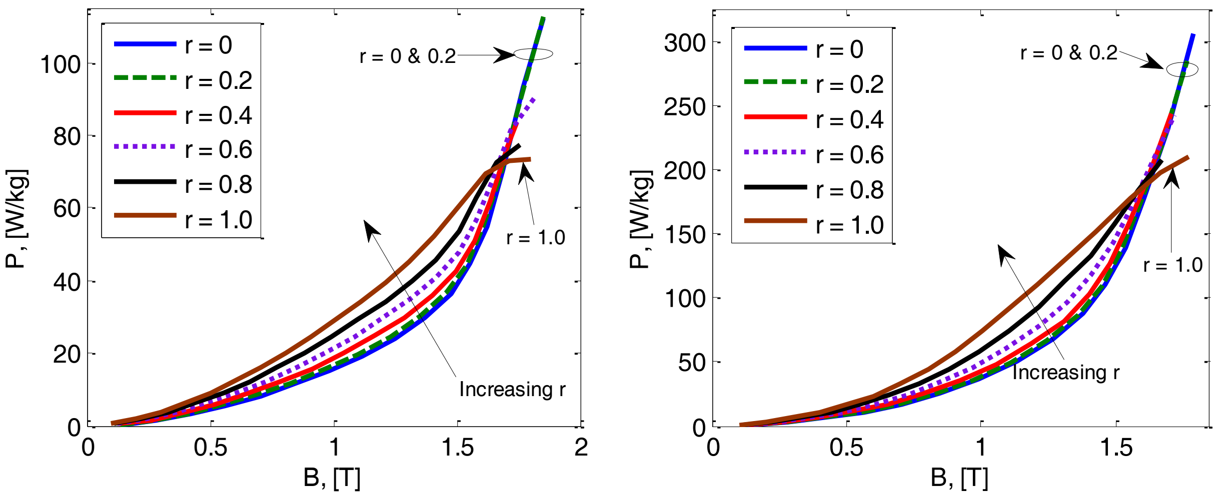

(a) M19G29 **(b) M19G24**

Fig. 5.4 Measured core losses at 400 Hz

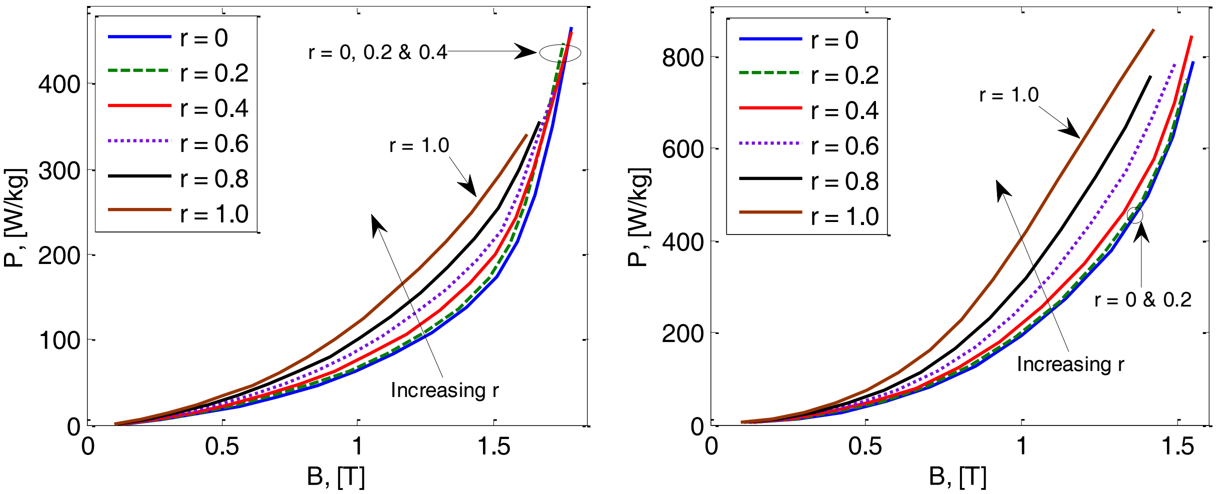

(a) M19G29 **(b) M19G24**

Fig. 5.5 Measured core losses at 1 kHz

The rotational core loss ratios with respect to pulsating core losses are shown in Fig. 5.6 for the two samples, at 1.0 T. The ratios are derived from Table 5.2. The ratios seem to be independent of frequency and sample gauge. At this flux density for rotating flux ($r = 1$), the loss is twice the pulsating core loss, and for a more realistic aspect-ratio of 0.7, it is 1.5 times the pulsating core loss. This is significant considering the localised distribution of the aspect-ratio in a stator core. Consequently, it will result to local heating of the stator and hence the need to consider the distribution of rotational core losses in the design and increasing the rating of machines [8].

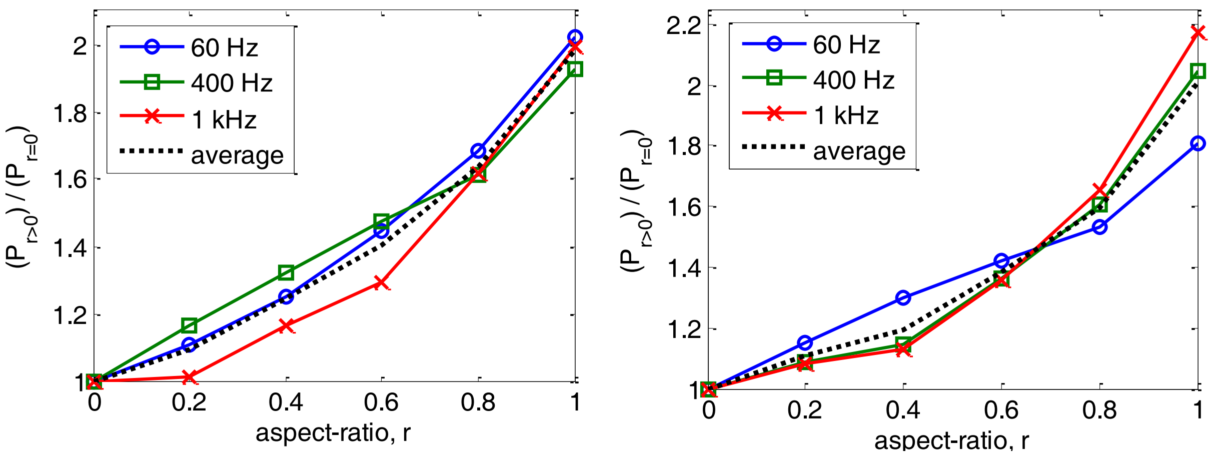

(a) M19G29 **(b) M19G24**

Fig. 5.6 Core loss ratios with respect to the pulsating core loss, at 1.0 T

Table 5.2 Measured core losses, at 1.0 T

(a) M19G29

Aspect-ratio, *r*	**0**	**0.2**	**0.4**	**0.6**	**0.8**	**1**
$P_{60\ \mathrm{Hz}}$, (W/kg)	0.96	1.06	1.20	1.38	1.61	1.94
$P_{400\ \mathrm{Hz}}$, (W/kg)	15.16	17.66	20.02	22.37	24.45	29.19
$P_{1\ \mathrm{kHz}}$, (W/kg)	63.02	63.64	73.41	81.43	101.87	125.68

(b) M19G24

Aspect-ratio, *r*	**0**	**0.2**	**0.4**	**0.6**	**0.8**	**1**
$P_{60\ \mathrm{Hz}}$, (W/kg)	1.66	1.91	2.16	2.36	2.55	3
$P_{400\ \mathrm{Hz}}$, (W/kg)	36.17	39.42	41.44	49.38	58.08	74
$P_{1\ \mathrm{kHz}}$, (W/kg)	192.77	208.63	217.92	261.95	318.66	418.85

The impact of rotational core losses in the distribution of core losses is significant in high-speed machines that operate at higher frequencies, such as 400 Hz or 1.5 kHz [4]. As previously mentioned, rotational core loss ratios with respect to pulsating core losses are independent of frequency. Hence, it is by direct comparison of the core losses at a given flux density operating point and frequency, that the significance of rotational core losses is appreciated. For example, consider the M19G29 material of thinner gauge and lower loss, which is fit for high frequency applications as opposed to the M19G24. At 1.0 T and 60 Hz, the core loss difference between an aspect-ratio of 0.8 and zero (pulsating) is 0.65 W/kg, 7.21 W/kg and 39 W/kg, at 60 Hz, 400 Hz and 1 kHz, respectively, as determined from Table 5.2. However, the core loss ratios for each aspect-ratio to pulsating, are the same irrespective of the frequency, but the magnitudes are different, besides the under estimation of core losses by using only pulsating data.

It is important to note that the core losses for the M19G29 sample at the three test frequencies, and 60 Hz for the M19G24 sample, were done within 5 ºC (ΔT) from the room temperature according to ASTM standards [72]. For the M19G24 sample at 400 Hz, $\Delta T \geq 5$ ºC for $B > 1.0$ T, and $\Delta T \geq 10$ ºC for $B > 1.5$ T. At 1 kHz, $\Delta T \geq 5$ ºC for $B > 0.5$ T, and $\Delta T \geq 10$ ºC for $B > 1.0$ T. This implies the challenges of measuring core losses at higher frequencies for thicker samples, which requires cooling of both the sample and the yoke.

Besides that, it was difficult to control the elliptical aspect-ratios (0.2 to 0.8), for flux densities greater than 1.5 T, for all the test frequencies, in both samples. For example, Fig. 5.7 (a) shows the aspect-ratios of the M19G29 sample at 60 Hz. This is because the B-locus was controlled using the fundamental components of B and their phases. This can be corrected by designing a waveform controller (which is beyond the scope of this thesis) to make the B-coil voltages sinusoidal. This will result to better control of the aspect-ratio and keep the B-coil voltage signal form-factors within 1.1107 ± 1 % according to ASTM standards [73].

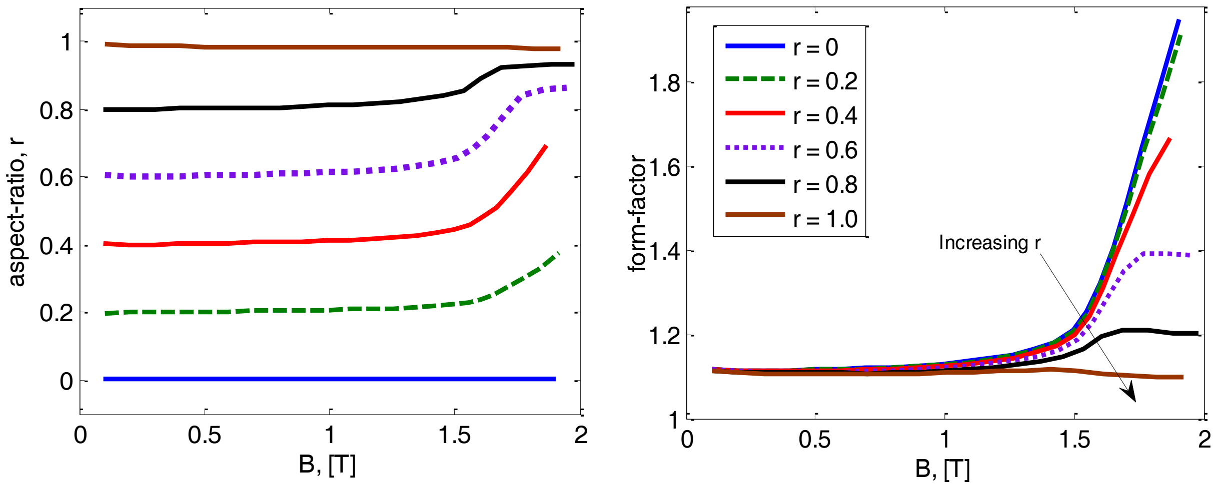

(a) Aspect-ratio, r **(b) Form-factor of $e_{Bx}(t)$**

Fig. 5.7 Measured aspect-ratios and form-factors of the M19G29 sample, at 60 Hz

The form-factors were similarly affected as seen in Fig. 5.7 (b) for the M19G29 sample at 60 Hz for the B_x-coil. This factor was determined as a ratio of the B-coils' rms voltage to its absolute mean voltage. The form-factor for B_x-coil was higher since the sample saturate earlier along the rolling direction (x-axis), than on the transverse direction (y-axis).

5.3 Core Losses under Non-sinusoidal Excitation

The B-loci at the tooth-root of the stator core of the hydro generator shown in Fig. 1.4, at different field currents, were used to evaluate the effectiveness of the proposed magnetizer to reproduce non-sinusoidal flux density waveforms obtained from FEA. The analysis was done at 60 Hz using the M19G29 sample. The loci are shown in Fig. 5.8 (a) to (c) for a field current (I_f) of 560 A and 1090 A at no load, and 1055 A at full load.

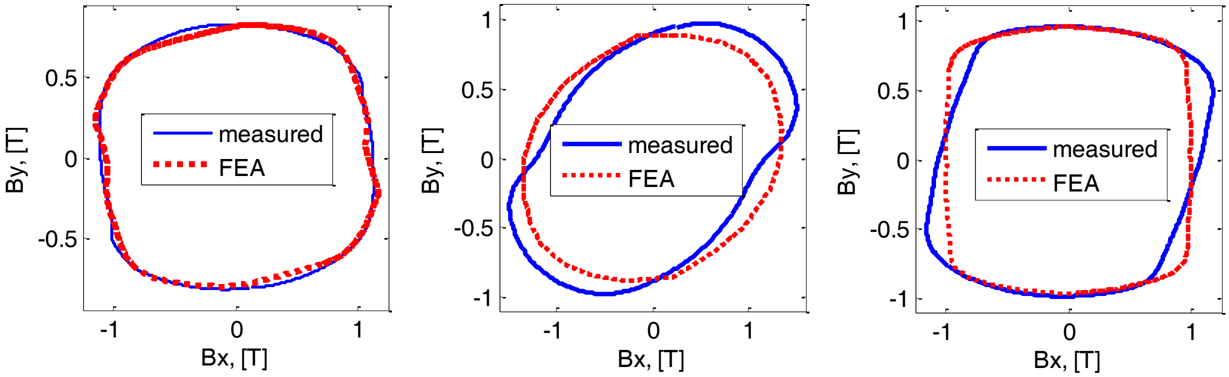

(a) $I_f = 560$ A; no load **(b) $I_f = 1090$ A; no load** **(c) $I_f = 1055$ A; full load**

Fig. 5.8 Measured and numerical B-loci, at 60 Hz

There is good agreement of the loci in Fig. 5.8 (a), but there is some differences in Fig. 5.8 (b) and (c), which is because of the open loop control of the flux density magnitudes and their phase difference, but not their waveforms. However, for flux densities equal or greater than 1.0 T, the magnetizer can still reproduce the waveforms as demonstrated by Fig. 5.8 (a).

These results are tabulated in Table 5.3, which shows a difference between the loss obtained using rotational magnetization ($r > 0$), and that of pulsating magnetization ($r = 0$). In the latter

Table 5.3 Non-sinusoidal measured core losses, at 60 Hz

I_f, (A)	Aspect-ratio, r	B_x, (T)	B_y, (T)	P, (W/kg)
560	0.7	1.12	0.82	1.87
	0	1.11	0.81	1.18
1090	0.5	1.50	0.98	2.83
	0	1.51	0.91	3.78
1055	0.7	1.17	0.97	2.24
	0	1.17	0.94	2.83

case, the *x* and *y* core losses were measured independently along the corresponding axes of the sample, and then summed to get the final core loss value.

As noted earlier, the shortcomings of evaluating core losses from pulsating data will be more significant at higher flux densities and frequencies.

5.4 Conclusion

The capability of the proposed magnetizer in the measurement of core losses was demonstrated using two samples (M19G29 and M19G24), at 60 Hz, 400 Hz and 1 kHz. The magnetizer can achieve very high flux densities in the range of 2 T at 60 Hz for both G29 (0.35 mm) and G24 (0.65 mm) samples. For G29 samples, flux densities of 1.8 T and 1.6 T can be measured at 400 Hz and 1 kHz, respectively. For the thicker G24 samples, the flux density measurement range reduces to 1.7 T and 1.4 T, for 400 Hz and 1 kHz, respectively.

Analysis of core losses at 400 Hz and 1 kHz showed that rotational measurements are invaluable in the analysis and design of high-speed machines, as they result to local heating. For a flux density of 1.0 T using the M19G29 sample, the core loss difference between an aspect-ratio of 0.8 and zero (pulsating) was 0.65 W/kg, 7 W/kg and 39 W/kg, at 60 Hz, 400 Hz and 1 kHz, respectively. At higher frequencies the difference will even be higher, which will result to local degradation of the lamination stack insulation, and eventual failure of the machine, if they are not considered in the design.

The magnetizer can also reproduce numerical waveforms for flux densities equal or less than 1.0 T, without any waveform control. The future implementation of a feedback controller will improve the performance of the magnetizer in terms of meeting the measurement standards (form-factor and aspect-ratio), and in expanding the measurement range of non-sinusoidal waveforms.

It is important to identify the sources of errors of the proposed measurement setup, as discussed next.

Chapter 6. Measurement Errors and Uncertainty Analysis

A procedure for estimating the uncertainty of the fieldmetric measurement of core losses is described. It can be generalised to any measurement setup, as it is derived from elementary errors, which are estimated over the entire flux density measurement range. This permits cost effective correction by neglecting insignificant sources. Moreover, it is shown that the fieldmetric measurement of core losses is predisposed to the *H*-coil airflux leakage field and correlational errors. In particular, the *H*-coil airflux leakage field systematic error, which contributes about 70 % to the total uncertainty. The latter is caused by the control of the flux density waveforms that influence the measurement of the magnetic field more than the flux density. The contribution of the sampling frequency to the intertwining of *B*-*H* loops for flux densities beyond the knee point, which results in the drooping of the measured pulsating core losses; a characteristic of rotating core losses, will be discussed.

6.1 Classification of Measurement Errors

The true value of a physical quantity is unknown, and is therefore estimated by measurements. Consequently, the uncertainty of a measurement cannot be derived from the measured quantity, but has to be similarly estimated. Uncertainty is the interval where the true value of a physical quantity lies with a given probability [74]. Its components are measurement errors, which are derived from the input arguments of the measurement system.

In fieldmetric measurement of two-dimensional rotational core losses, the input arguments are the tangential components of the flux density and magnetic and fields, as expressed in equation (36). The smallest errors that contribute to these argument errors, are elementary errors, which are dependent on the measurement system.

Measurement errors are usually classified into systematic, random and unknown errors, [74], [75]. *Systematic errors* remain after repeated measurements, under the same measurement conditions. Hence, they cannot be directly determined from measurements, but have to be estimated from fundamentally different measurement methods, instruments and measurement conditions, and minimized by corrections [74]. In this work, they are estimated from analytical models and special experiments, due to a lack of alternative measurement methods. They should be corrected such that only random errors remain. However, correction is dependent on the cost and the accuracy of measurements [76], [77], [78]. *Random errors* vary within limits with repeated measurements, under the same measurement conditions [74]. They include variations caused by temperature, electromagnetic noise, some instrument and personnel errors, and other sources of measurement noise. Random errors are reduced by carrying out measurements under the same standardized conditions, instruments and measurement methods. The *unaccounted errors* are *unknown* owing to limitations of the measurement and uncertainty procedures, and the experience of the personnel. For example, unaccounted installation, operation and time dependent factors, will influence the field uncertainty [78].

It is important to reduce errors individually to the target uncertainty, as it results in the acceptance or rejection of a product or process, with an associated cost. For example, the type of an instrument may improve uncertainty [78], [79], while the interpretation and the commitment of the personnel will influence the results [80].

In core losses, systematic errors are classified into methodological, instrumentation and human errors [74], [81], with respect to a certain flux density and frequency. The elementary components of these classes of systematic errors are either absolute or conditionally constant. *Absolute constant systematic errors* remain constant, while *conditionally constant systematic errors* vary within limits with repeated measurements, under the same measurement conditions [74].

Methodological errors arise from the limitations of the fieldmetric model of equation (36) in representing the actual core loss. These includes the negation of the z-loss, CW-CCW core loss asymmetry, the inclusion of airflux leakage fields in the measurement of B and H, and the acquisition and processing of core losses (sampling frequency, averaging, integration etc.).

Instrumentation errors are caused by the inaccuracy of the measuring instruments. Examples are offset and gain errors of signal acquisition and conditioning circuits, phase shifting of waveforms caused by filters and multiplexed data acquisition systems, location, sizing, waveform control, calibration and misalignment of sensors.

Human errors are associated with the personnel performing the measurement. For instance, in the control of the magnitudes and the phase angle between B_x and B_y waveforms, and in the assembly and alignment of sensors and samples.

6.2 Review of Uncertainty Estimation Methods

Different methods have been proposed to estimate uncertainty. They include the Guide to the Expression of Uncertainty in Measurement (GUM) [82], the Monte Carlo method (MCM) [83], [84], fuzzy based methods [84], the polynomial chaos methods (PCM) [85], the generalized lambda distribution [86], the unscented transform method [87], the numerical integration [88] and other methods reviewed in [89]. The first four methods are described further.

The GUM is widely used due to its ease of implementation [89]. It is based on the first-order Taylor series, which linearizes the measurement function, allowing separate estimation of its input uncertainties [77]. The negation of higher-orders introduces additional errors [90], but permits individual analysis of the inputs to the total uncertainty. The GUM assumes systematic errors have been corrected, which biases the uncertainty if the systematic errors are improperly corrected, or are unknown. This method requires the determination of the influence and correlational coefficients. Hence, it is limited to measurements with linear models, whose coefficients can be determined [77], [89], [90], [91]. The estimation of these coefficients and combining the uncertainties, will also introduce additional errors. Therefore, the GUM is supplemented by a Monte Carlo based method [83] to account for uncorrelated input variables, as the MCM is not dependent on coefficients, while in [74], systematic errors are considered.

The Monte Carlo method requires the emulation of random data from the probability density function (PDF) of each input, to generate the output PDF [88], [92]. The random values should be within the error limits of each input (e.g. provided by the manufacturer [93]). Hence, the application of the MCM to fieldmetric measurement of core losses is challenging due to the non-linear correlation of the input quantities, whose error limits are unknown, and the limitation of measured data. However, the MCM method is applicable to uncorrelated cases [94], and complex valued quantities [95]. Similarly, the assumption is that all the errors are random, besides being computationally intensive [84], [92].

The random fuzzy variables (RFVs) method proposed in [91], does not require a derivable model [84]. In addition, assumptions are not necessary in assigning the confidence and PDFs over an interval [91]. Hence, it accounts for random, systematic, and unknown errors. The resultant uncertainty is then obtained from the combination of input RFVs [75]. A method similar to RFV that accounts for the correlation between the inputs in the evaluation of systematic uncertainty is described in [96]. Nevertheless, it requires a linear model; else, numerical methods such as the MCM are used to get the output PDF. Additionally, it requires the determination of the correlation coefficient.

In the polynomial chaos approach, the PDFs of the inputs are generated using polynomials. The PDFs are then added resulting to an output polynomial, from which the uncertainty is determined [85], [97]. This method assumes all source of errors are random, and the use of polynomials complicates its application. However, it can be used to evaluate the uncertainty, and its worst case [97].

The procedure for uncertainty management (PUMA) proposed in [90] is very practical. It is based on iterating uncertainty, starting with rough but fast estimations, followed by costly, intensive, and time consuming, but accurate iterations [90]. If the first iteration meets the threshold of the target uncertainty with a good margin, further iteration are not necessary, saving time and cost of measurements.

Most of the previously reviewed methods are focused on accuracy and mathematical modeling, but lack on the ease of implementation [98]. Therefore, it is challenging for non-metrology and/or non-statistical personnel, to estimate the uncertainty of a process or product. Implementation is important, as the personnel is required to identify, correct, make necessary assumptions, model, and process the elementary errors. Therefore, the GUM is popular due to its ease of its implementation, despite its shortcomings. Moreover, the GUM allows the tracking of the elementary errors, which lowers the cost of measurements by identifying and correcting the most dominant sources of errors. In this study, the method proposed in [74] that improves the GUM by considering systematic errors, and does not require correlational coefficients, is used.

Most of the studies done in core loss measurement error analyses is comparative in nature. It involves comparing the thermometric and fieldmetric methods in the same or in different laboratories [28], [32], [54], [55], [56]. Reference [56] further evaluates the uncertainty of samples cut from the same parent material under rotating flux in six laboratories. The reported uncertainties varied from 3.6 % to 12 %, which can be attributed to different measurement methods, sample and magnetizer errors, sensors errors, wave form control, sources of errors considered in each case, and the error estimation methods. It fails to standardize some of these parameters such as the sample, measurement area sizes, sensor sizes etc., which can effectively reduce some errors.

In [99], uncertainty is estimated for pulsating core losses. It was determined from the partial derivatives of the arguments of a compensated core loss model. It however lacks in the estimation of elementary errors, which are usually dependent on the measurement system, and hence difficult to generalize.

Therefore, this chapter estimates elementary errors in the fieldmetric measurement of core losses. These errors are then used to derive the *B* and *H* argument errors, from which the total uncertainty is estimated over a range of 0.1 T to 1.9 T, at 60 Hz. This is important in tracking the contribution of each elementary error to the total uncertainty. Hence, the cost of measurements can be lowered by minimizing only the most dominant sources of errors. Moreover, some of the systematic errors, such as the sampling frequency, and misalignment of *H*-coils, are corrected. Furthermore, the airflux leakage field is shown to contribute to 70 % to the total uncertainty. This field was shown to modify the shape, amplitude and phase of the measured field in Chapter 3. This procedure can be generalized to any core loss measurement system, allowing the comparison of different measurement methods and setups, as it is dependent on elementary sources of errors. However, its accuracy is prone to the bias of estimating and correcting elementary errors.

6.3 Quantifying Measurement Errors and Uncertainty

Recall that rotational core losses are determined from indirect measurements of *B* and *H* tangential input arguments, using the fieldmetric function as:

$$P = \frac{1}{T\rho}\int\left(H_x\frac{dB_x}{dt} + H_y\frac{dB_y}{dt}\right)dt = f(B_x, H_x, B_y, H_y), \tag{36}$$

where ρ is the mass density of the sample and $T = 1/f_{test}$ is the periodic time and f_{test} is the test frequency. In this study, ρ and f_{test} are assumed constant; hence, their errors are neglected.

The input arguments of fieldmetric equation (36) are simultaneously measured; which is defined as dependency in [74]. In addition, they are non-linearly correlated since the variation of one of the argument results to a non-linear variation of one or more arguments.

The true core loss value *P* is estimated as $\widetilde{P}$ by the measurement equation (36), such that the absolute error is:

$$\mathit{\Delta} P = \widetilde{P} - P = f(\widetilde{B}_x, \widetilde{H}_x, \widetilde{B}_y, \widetilde{H}_y) - f(B_x, H_x, B_y, H_y)\,, \tag{37}$$

which is expressed by the first-term of the Taylor series by neglecting the higher order terms as:

$$\mathit{\Delta} P = \left(\frac{\partial}{\partial B_x} \mathit{\Delta} B_x + \frac{\partial}{\partial H_x} \mathit{\Delta} H_x + \frac{\partial}{\partial B_y} \mathit{\Delta} B_y + \frac{\partial}{\partial H_y} \mathit{\Delta} H_y \right) f(B_x, H_x, B_y, H_y)\,, \tag{38}$$

where $\mathit{\Delta} B_{x,y}$ and $\mathit{\Delta} H_{x,y}$ are the errors of estimating the arguments $B_{x,y}$ and $H_{x,y}$. The error is expressed in relative form to make it independent of units as:

$$\varepsilon_P = I_{B_x} \varepsilon_{B_x} + I_{H_x} \varepsilon_{H_x} + I_{B_y} \varepsilon_{B_y} + I_{H_y} \varepsilon_{H_y}\,, \tag{39}$$

where $\varepsilon_P = \mathit{\Delta} P / P$. $\varepsilon_{B_{x,y}}$ and $\varepsilon_{H_{x,y}}$ can similarly be expressed as relative errors of the arguments.

The products of the partial derivatives and the ratio of the arguments to the core loss, results to influence coefficients given by:

$$\left. \begin{aligned} I_{B_{x,y}} &= \frac{B_{x,y}}{P} \frac{\partial P}{\partial B_{x,y}} = \frac{B_{x1,y1}}{P} \cdot \frac{\pi f}{\rho} H_{x1,y1} \sin \phi_{x1,y1} \\ I_{H_{x,y}} &= \frac{H_{x,y}}{P} \frac{\partial P}{\partial H_{x,y}} = \frac{H_{x1,y1}}{P} \cdot \frac{\pi f}{\rho} B_{x1,y1} \sin \phi_{x1,y1} \end{aligned} \right\} . \tag{40}$$

The partial derivatives are estimated from equation (36), which is rewritten as:

$$P \approx \frac{\pi f}{\rho} \left(B_{x1} H_{x1} \sin \phi_{x1} + B_{y1} H_{y1} \sin \phi_{y1} \right), \tag{41}$$

by assuming sinusoidal fields whose loss angle is $\phi_{x1,y1}$ between $B_{x1,y1}$ and $H_{x1,y1}$ phasors. This assumption holds for rotating core loss measurements of non-oriented samples, where H and B are more sinusoidal. In cases where they are non-sinusoidal, it still holds to a great extent since the fundamental components contribute most to the core loss, although the influence coefficients will be biased, resulting in uncertainty estimation errors.

The total measurement error is then estimated from the argument errors, whose contribution to the overall error is weighted by the influence coefficients, which are dependent on other variables of the measurement equation.

The relative error expression in equation (39) is expressed in general form for *N* input arguments as [74]:

$$\varepsilon_P = \sum_{j=1}^{N} I_j \varepsilon_j = \sum_{j=1}^{N} I_j L_j + \sum_{j=1}^{N} I_j \upsilon_j + \sum_{j=1}^{N} I_j \psi_j \ . \tag{42}$$

Hence, the resultant measurement error is the sum of the absolute constant systematic errors (L_j), conditionally constant systematic errors (υ_j) and random errors (ψ_j), respectively. It also shows that systematic and random errors are associated with each input argument error.

6.3.1 Absolute Constant Systematic Errors

The identification of systematic errors requires the use of fundamentally different measurement methods, and comparing the same results from different laboratories and setups [74]. In this study, systematic errors are estimated from analytical models and special experiments, owing to a lack of comparative measurement methods.

Absolute constant systematic errors are constant with repeated measurements. They bias the measured core loss. Their overall limits, L_{ac} can expressed in general form from equation (42) as [74]:

$$L_{ac} = L_{eqn} + \sum_{j=1}^{N} I_j L_j \ . \tag{43}$$

L_{eqn} is the error limit of the measurement equation that is obtained by using a fundamentally different measurement method (thermometric or torquemetric), while L_j is the limit of the absolute constant systematic error of the j^{th} argument.

6.3.2 Conditionally Constant Systematic Errors

Conditionally constant systematic errors vary within limits under repeated measurements, and are similarly expressed in general form from equation (42) as [74]:

$$\upsilon_{cc} = \sum_{j=1}^{N} I_j \upsilon_j = \sum_{j=1}^{N} \sum_{i=1}^{k_j} I_j \upsilon_{j,i} \ , \tag{44}$$

where k_j is the number of conditionally constant elementary errors in the measurement of the j^{th} argument.

Some of the elementary errors in the measurement of B and H are caused by the same influence quantity. Core loss measurements require the control of the aspect-ratio (r), via the fundamental B components (B_{px} and B_{py}) and their phase shifts such that:

$$r = \frac{B_{px} < 0°}{B_{py} < \pm 90°} = 1 . \tag{45}$$

The variation of B peaks and their phase shifts will result in linear and non-linear variations in B and H arguments, depending on the magnetic loading of the sample. The elementary errors caused by the control of the aspect-ratio are treated as additional conditionally constant systematic errors as:

$$\upsilon_{add} = \sum_{j=1}^{N} I_j \upsilon_{jBpk} + \sum_{j=1}^{N} I_j \upsilon_{j\phi} , \tag{46}$$

where υ_{jBpk} and $\upsilon_{j\phi}$ are additional errors caused by the control of the peak flux densities and their phase shifts, respectively. They are summed to the rest of the conditional systematic errors while retaining their signs [74], [98]. This also accounts for the correlation of the inputs, negating the need for their evaluation. Correlational coefficients are difficult to formulate for dependent indirect non-linear measurements like core losses [74]. The sum of the conditionally constant systematic errors is therefore [74]:

$$\left.\begin{aligned} \upsilon_{cc} &= \sum_{j=1}^{N} I_j \upsilon_{jBpk} + \sum_{j=1}^{N} I_j \upsilon_{j\phi} + \sum_{j=1}^{N} \sum_{i=1}^{k_j-2} I_j \upsilon_{j,i} \\ &= \upsilon_{add} + I_1 \sum_{i=1}^{k_1-2} \upsilon_{1,i} + I_2 \sum_{i=1}^{k_2-2} \upsilon_{2,i} + \ldots + I_N \sum_{i=1}^{k_N-2} \upsilon_{N,i} \end{aligned}\right\} , \tag{47}$$

where I_N is the influence coefficient of the N^{th} argument.

The probability density distributions of conditionally constant errors should then be constructed to determine their limits (θ) with a given confidence (α), such that $|\upsilon_{cc}| \leq \pm\theta_{\alpha}$ [74]. To simplify the analysis, elementary conditional errors are assumed to vary randomly with a uniform distribution within a probability confidence, α such that their limit is [74]:

$$\left.\begin{aligned} \theta_\alpha &= k\sqrt{\theta_{add}^2 + \sum_{j=1}^{N} I_j^2 \theta_{0,j}^2 + \sum_{j=1}^{N} \sum_{i=1}^{k_j-2} I_j^2 \theta_{j,i}^2} \\ &= k\sqrt{\theta_{add}^2 + \sum_{j=1}^{N} I_j^2 \theta_{0,j}^2 + I_1^2 \sum_{i=1}^{k_1-2} \theta_{1,i}^2 + I_2^2 \sum_{i=1}^{k_2-2} \theta_{2,i}^2 + \ldots + I_N^2 \sum_{i=1}^{k_N-1} \theta_{N,i}^2} \end{aligned}\right\}, \tag{48}$$

where θ_{add} is from the correlational additional errors (υ_{add}), and:

$$\left.\begin{aligned} &\theta_{0,j} = \frac{\theta_{j,\alpha}}{\alpha} \text{ and } \theta_{j,\alpha} = u_{j,\alpha} \\ &u_{j,\alpha} = k\sqrt{\sum_{i}^{k_j} \theta_i^2} \end{aligned}\right\}, \tag{49}$$

where $u_{j,\alpha}$ is the uncertainty of the j^{th} argument. In practice, a 0.95 confidence probability (α) is often assumed. k is a correction factor based on the number of component errors and the confidence probability, α. Hence, for an α of 0.95, k is 1.13 for an infinite number of error components, and 1.10 for two error components [74].

The standard deviation of the overall conditionally constant systematic error is then determined from the limit as [74]:

$$S_\upsilon = \frac{\theta_\alpha}{z_{\frac{1+\alpha}{2}}}, \tag{50}$$

where $z_{\frac{1-\alpha}{2}}$ is the quantile of the normalized normal distribution of the assumed confidence probability of 0.95, found using the normalized Gaussian and distribution functions as 1.96. Usually, elementary conditionally constant errors are assumed to be uniformly distributed, while their sum is normal distributed [74].

6.3.3 Overall Random Error

Random errors vary within limits with repeated measurements, under the same conditions. The method of reduction proposed in [74] is used to quantize the overall random error of the measurement because it negates the need for correlational coefficients used in the GUM [82]. This is because correlational coefficients are difficult to estimate for dependent indirect non-linear measurements, such as core losses [74]. To avoid overestimating the final uncertainty, the elementary random error components are neglected during the estimation of the argument errors, since they contribute to the overall random error [74].

Let the input arguments from a measurement vector *i* be represented by a set:

$$\{B_{xi}, H_{xi}, B_{yi}, H_{yi}\}, i = 1,\dots,n,$$

where *n* is the number of repeated measurements. The vectors are measured simultaneously under the same conditions over a time interval *t*. The *i*th value of the measured core loss, P_i is obtained by substituting the *i*th vector into the core loss equation (36), giving a set of *n* core loss values as:

$$\{P_1, P_2,\dots,P_n\}, i = 1,\dots,n.$$

Therefore, the measured core loss is estimated from the mean as:

$$\tilde{P} = \overline{P} = \frac{1}{n}\sum_{i=1}^{n} P_i. \tag{51}$$

Its variance is the square of its standard deviation as [74]:

$$S_r^2 = \frac{1}{n(n-1)}\sum_{i=1}^{n}\left(P_i - \overline{P}\right)^2. \tag{52}$$

6.3.4 Total Uncertainty

The total uncertainty is then derived from the limits of the absolute constant systematic error and the standard deviations of the conditionally systematic constant and random errors.

The combined standard deviation S_c is [74]:

$$S_c = \sqrt{S_\upsilon^2 + S_r^2}, \tag{53}$$

which gives the combined uncertainty as [74]:

$$u_c = t_c S_c, \tag{54}$$

where [74]:

$$t_c = \frac{\theta_\alpha + t_q S_r}{S_\upsilon + S_r}.$$

t_q is from the Student's distribution for the selected confidence probability of the exact number of degrees of freedom, $v = (n-1)$. For $\alpha = 0.95$ and $v = 9$, and n = 10 (number of repeated measurements), t_q = 2.26 [74]. The total uncertainty is then:

$$u_t = L_{ac} + u_c. \qquad (55)$$

6.4 Estimation and Correction of Elementary Errors

This section analyses the different sources of core loss elementary errors, and where possible the systematic errors are corrected. The resultant systematic errors are estimated from the residues of the corrected and uncorrected systematic errors, which are combined with random errors to approximate the total uncertainty.

The sources of errors for the measurement system shown in Fig. 5.2 include the data acquisition errors, power amplifier distortions, magnetizer induced errors, sensor misalignments, sensor calibration, and electromagnetic interference, among others. It is therefore necessary to make simplifying assumptions, in estimating the system uncertainty. Therefore, the linear power amplifiers were considered ideal, and the traceability of the entire system components was neglected.

6.4.1 Sampling Frequency Error

The sampling frequency (F_s) affects the width and the shape of the *B-H* loop at high flux densities beyond the knee, resulting in core loss errors. At these flux densities, the loop increases in size along the *H*-axis because of the higher magnetic fields.

To investigate this error, pulsating measurements were done on an M19G29 sample at 60 Hz at 1.9 T, where the loops were expected to be wide. As depicted in Fig. 6.1 (a), at a sampling frequency of 21.6 kHz (~46 μs; 360 samples/cycle), the loop was intertwined and narrow.

According to Madelung rules, *B-H* loops should not intertwine, and the inner loops should be contained within the major loop, under pulsating conditions [100]. Doubling the sampling frequency untangled the loop, and at 86.4 kHz (~12 μs; 1,440 samples/cycle), the loop was even wider than at twice the sampling frequency of 43.2 kHz (~23 μs; 720 samples/cycle). The effect of sampling frequency on the measured pulsating core losses is seen in Fig. 6.1 (b). For 21.6 kHz, the core loss peaks, droops and even goes negative; a characteristic observed in rotating ($r = 1$) core losses. This was caused by the intertwining of the *B-H* loops at high flux densities, where the core loss became negative. In addition, intertwining results in the inner loops laying outside the major loop. This effect of sampling frequency contributes to CW-CCW loss asymmetry, under rotating fields, and underestimation of core losses.

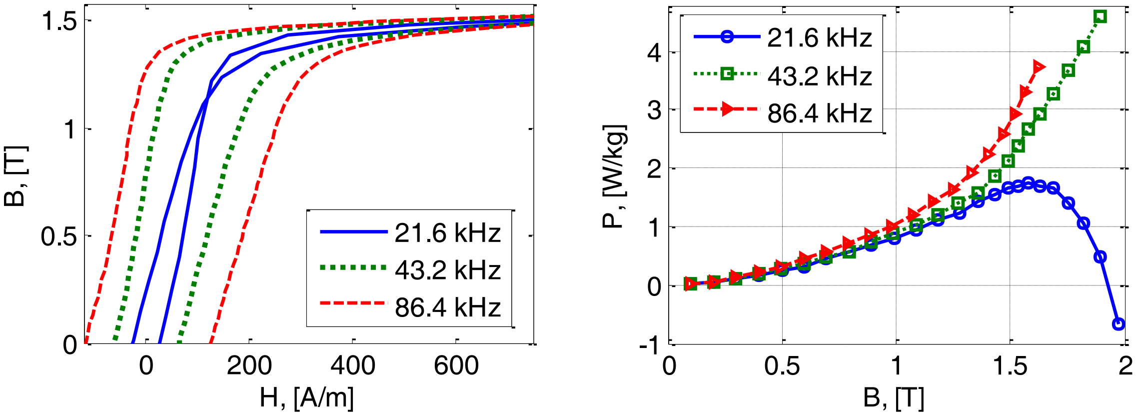

(a) *B-H* curves at 1.9 T and 60 Hz **(b) Pulsating core losses at 60 Hz**

Fig. 6.1 Effect of sampling frequency on *B-H* curves and pulsating losses, at 60 Hz

The sampling frequency error is a typical absolute systematic error that was corrected by increasing the sampling frequency. As seen in Fig. 6.2, the loss will tend to a value with increasing sampling frequency.

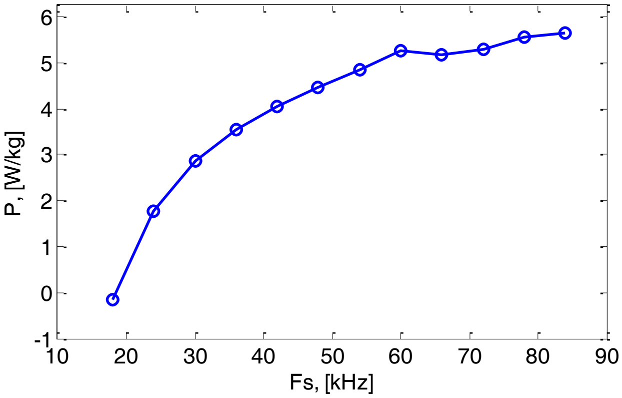

Fig. 6.2 Effect of sampling frequency on pulsating core losses, at 1.8 T and 60 Hz

However, the sampling frequency is dependent on the execution time of the program, the test frequency and the properties of the data acquisition system. Therefore, the flux density range should be limited to a flux density where the loops obey Madelung's rules. Corrections can also be made using a different measurement method, such as thermometric or torquemetric.

6.4.2 Number of Averaging Cycles Error

Fieldmetric core loss measurements requires the number of cycles (m) to be greater than one to reduce random errors by averaging. The total time of the captured waveform is mT of period T. The fieldmetric equation (36) is rewritten in summation form as:

$$P = \frac{1}{N_s \rho} \frac{1}{N_B A_B} \sum_{k=1}^{N_s} \left(H_x(k) e_{Bx}(k) + H_y(k) e_{By}(k) \right), \tag{56}$$

where N_s is the number of samples per cycle.

The influence of the number of averaging cycles and sampling frequency on the measured core losses was analysed at 1.0 T under rotating magnetization, at 60 Hz. The tests were repeated n times. Core losses were then determined over the entire length of the waveforms, i.e. over mT. The waveforms were then averaged over a period T, and the core loss evaluated for a cycle. As seen in Table 6.1, there is no significant difference in the values determined over mT ($m > 1$) or averaged over one cycle, T ($m = 1$). However, if only one cycle was captured, then higher differences would have been reported, since averaging reduces random errors.

The sampling frequency has a higher influence on the measured core loss, $\overline{P}$ as discussed previously, and as seen in the core loss values of Table 6.1. As it increases, the core loss also increases, while the random error decreases as indicated by the standard deviation, σ. Increasing the number of cycles m, also decreases the random error, as indicated by the decrease in the standard deviation at 84 kHz, for 5, 10 and 20 cycles, in Table 6.1. This improves repeatability and reduces scatter [101]. The only setback is the need for fast acquisition and processing, which would make the measurement system expensive. Therefore, 5 cycles and 84 kHz (1400 samples/cycle) are used for subsequent error analysis at 60 Hz. The resulting core loss scatter given by the standard deviation, is associated with the number of cycles, and is part of the overall random error.

Table 6.1 The impact of averaging and sampling frequency on the core losses, at 60 Hz

F_s, (kHz)	***n***	***m***	$\overline{P}$ **, (W/kg)**	**σ, (W/kg)**	$\overline{B}$ **, (T)**	$\bar{r}$
21.6	20	1	1.4943	0.021642	1.0072	0.9857
		10	1.4944	0.021642		
43.2	20	1	1.7009	0.013139	1.0076	0.9833
		10	1.7009	0.013154		
84	15	1	1.8968	0.012875	1.0048	0.9832
		5	1.8992	0.015699		
	16	1	1.8904	0.015199	1.0060	0.9829
		10	1.8904	0.015201		
	15	1	1.8926	0.008489	1.0055	0.9833
		20	1.8912	0.009504		

F_s = sampling frequency; n = number of repeated measurements; $\overline{P}$ = average core loss; m = number of core loss averaging cycles; σ = standard deviation of n core losses; $\overline{B}$ = average B; $\bar{r}$ = average aspect-ratio

6.4.3 Analogue to Digital Converter (ADC) Error

Four simultaneously sampled 16 bit ADCs of dSPACE® DS 1103 controller board [102], were used in the acquisition of the voltage signals of B and H coils. Their full-scale input voltage range, FSV was ±10 V, with a resolution of $2^{16\text{ bits}}$. A lower FSV would increase the acquisition sensitivity. Multiplexed ADCs induce a phase shift between the B and H waveforms; affecting the loss angle and contributing to CW-CCW loss asymmetry if not compensated [68]. The error limits of the ADCs are given in Table 6.2.

Table 6.2 The error limits of dSPACE ADCs used in data acquisition [102]

Errors	**Value**
Offset error	± 5 mV
Offset drift	40 µV/K (ΔT = 5 ° K; 200 µV)
**Total offset error*, Δ_{offset}	± 5.2 mV (± 0.052 %)
Gain error	± 25 mV (± 0.250 %)
Gain drift	50 ppm/K (ΔT = 5 ° K; $250\times FSV/10^6$)
**Total gain error*, Δ_{gain}	± 27.5 mV (± 0.275 %)
SNR > 83 dB	$P_{noise} = P_{signal}/10^{8.3} = FSV/10^{8.3} \rightarrow 0$

*Calculated using reference [103]; FSV = full scale voltage (±10 V); SNR = signal to noise ratio

The total offset, Δ_{offset} and gain, Δ_{gain} errors were calculated according to [103], by assuming 5 º K (5 º C) temperature deviation from room temperature according to ASTM standard [104].The total ADC error is therefore [103]:

$$\Delta_{ADC} = \sqrt{\Delta_{offset}^2 + \Delta_{gain}^2}\,. \tag{57}$$

To avoid error duplication, the ADC error is treated as part of the *B* and *H* conditionally constant systematic errors. In relative form the ADC error is:

$$\left.\begin{aligned} \varepsilon_{B_{ADC}} &= \frac{\Delta_{ADC}}{FSV} I_{B_{ADC}} = \frac{\Delta_{ADC}}{FSV}\cdot\frac{|e_B|}{B_{pk}}\frac{\partial B}{\partial e_B} \\ \varepsilon_{H_{ADC}} &= \frac{\Delta_{ADC}}{FSV} I_{H_{ADC}} = \frac{\Delta_{ADC}}{FSV}\cdot\frac{|e_H|}{H_{pk}}\frac{\partial H}{\partial e_H} \end{aligned}\right\}, \tag{58}$$

where $I_{B,H_{ADC}}$ are the influence coefficients of the output voltages, $e_{B,H}$ with respect to *B* and *H*.

6.4.4 Magnetic Field Measurement Errors

H-coils are prone to an absolute constant systematic error from the inaccurate determination of the actual enclosed area and the non-uniform winding of the turns. This error was corrected by calibration using a known magnetic field *H* (*t*) generated by a Helmholtz coils setup as described in section 3.2.1 such that:

$$H(t) = \frac{k_{cal}}{\mu_0 N_H A_H}\int e_H(t)dt = K_H \int e_H(t)dt\,, \tag{59}$$

where k_{cal} is the calibration constant.

After calibrating, the remaining *H*-coil errors are the calibration residue; which is assumed negligible, the airflux leakage error, angular misalignment error, and the integration noise error.

A. Airflux leakage field error

In section 3.2, it was shown that the measured field is the superposition of the airflux and demagnetizing fields of the sample. The relative proportions of these two fields in the measured field, directly affects the core loss and the sample information embedded on the magnetic field waveforms. It is therefore important to analyse the airflux error, which is constant at each flux density measurement point, but changes with magnetic loading, frequency, magnetizer size and sample. Hence, it is an absolute constant systematic error, relative to each flux density measurement point, as well as a progressive error within the flux density range.

The fields at the sample surface (z = 0 mm) and the H-coil location (z = 1.5 mm) were extrapolated from Hall sensor measurements as described in section 3.2.3, and their amplitudes and phase shift difference tabulated in Table 3.3 and Table 3.4, respectively. From these tables, the peaks of the sample (H_s), and H-coil (H_c) fields and their phase shift difference, $\Delta\phi_{Hc}$, are tabulated in Table 6.3 at different flux densities.

Table 6.3 Sample, *H*-coil and airflux peak fields, under pulsating measurements, at 60 Hz

	z, (mm)	0.2 T	0.5 T	0.8 T	0.9 T	1 T	1.2 T	1.4 T	1.5 T	1.6 T	1.8 T	2 T
H_s, (A/m)	0	31	32	54	82	84	142	325	560	996	2,534	5,773
H_c, (A/m)	1.5	43	61	98	137	139	207	391	612	1,019	2,532	5,715
H_{af}, (A/m)	1.5	12	29	44	56	55	65	66	52	22	-2	-58
$\Delta\phi_{Hc}$°	1.5	-3.26	-5.77	-4.99	-4.58	-3.60	-3.56	-2.84	-1.70	-1.00	-0.23	-0.03

H_s = Peak sample field; H_c = Peak H-coil field; H_{af} = Peak airflux field at the H-coil location ($H_{af} \approx H_c - H_s$)
$\Delta\phi_{Hc}$ = fundamental phase shift difference between the sample and H-coil fields (ϕ_{Hc}- ϕ_s)°

From Fig. 3.18, the H-coil field, H_{coil} can be expressed as:

$$\left.\begin{aligned} H_{coil}(t) &= H_{sample}(t) + H_{airflux}(t) \\ H_{sample}(t) &= H_a(t) - H_{demag}(t) \end{aligned}\right\}, \tag{60}$$

where H_a is the applied field and H_{demag} is the total demagnetizing field of the sample, which is dependent on the sample geometry, eddy-currents, grain boundaries and other internal microstructural factors [10], and is analogous to internal resistance. Let:

$$\left.\begin{aligned} H_{sample} &= H_s \sin(\omega t) \\ H_{airflux} &= H_{af} \sin(\omega t + \Delta\phi_{af}) \end{aligned}\right\}. \tag{61}$$

Equation (60) is rewritten using trigonometry as:

$$\left.\begin{aligned} H_{coil}(t) &= H_s \sin(\omega t) + H_{af} \sin(\omega t + \Delta\phi_{af}) \\ &= H_c \sin(\omega t + \phi) \end{aligned}\right\}, \tag{62}$$

by neglecting H_{demag}. The peaks H_c and H_s and $\Delta\phi_{af} \approx \Delta\phi_{Hc}$, are known from Table 6.3. Hence, the peak H_{af} of equation (62), which simplifies to:

$$H_{af} \approx H_c - H_s, \tag{63}$$

can be calculated.

As the samples goes into saturation ($\mu_r \to 1$), the field decreases away from the sample surface, as discussed in section 3.2.3. Therefore, for equation (62) to hold mathematically, H_{af} has to be negative as seen in the case of flux densities greater than 1.8 T, in Table 6.3. Practically, H_{af} is positive, that is, it is in the direction of the applied field. It is now possible to reconstruct the magnetic fields at each flux density loading as shown in Fig. 6.3 for 0.2 T, at 60 Hz.

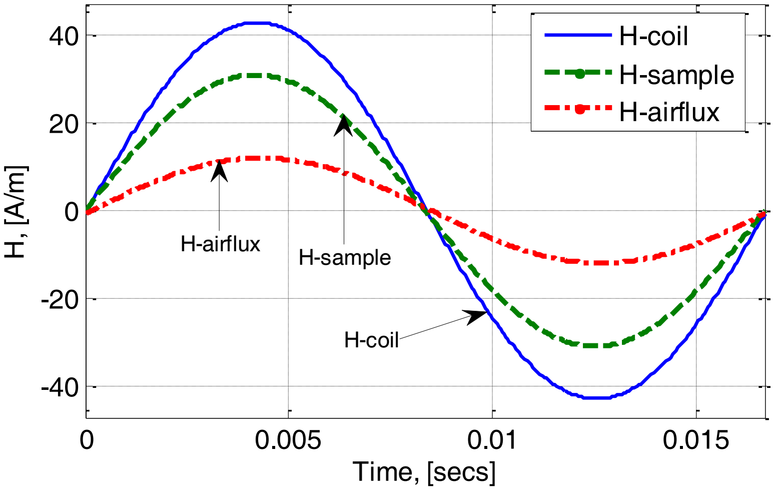

Fig. 6.3 Reconstructed magnetic fields at 0.2 T and 60 Hz

The airflux absolute constant systematic error, which is the difference of the measured and sample fields, is determined from equation (60), and Table 6.3 as:

$$\left.\begin{aligned} \Delta H &= H_{coil}(t) - H_{sample}(t) \\ &= H_{af} \sin\left(\frac{\pi}{2} + \Delta\phi_{Hc}\right) \end{aligned}\right\}. \tag{64}$$

Its relative error is:

$$\varepsilon_{H_{af}} = \frac{H_{af}}{H_{pk}}. \tag{65}$$

B. Angular misalignment error

The *H* and *B* coil sensor pairs should be orthogonal for accurate measurement of 2-D core losses. In addition, each tangential *H* and *B* coil should be aligned with the *x* and *y* axes. The fabrication and assembly of the measurement setup and its components results in angular misalignment in *H* and *B* coils, as illustrated in Fig. 6.4 for misalignments in *H*-coils.

H-coils can be misaligned with respect to each other, and/or with respect to *B*-coils. The following assumptions are necessary in analysing *H*-coil angular misalignments. *B*-coils are orthogonal and equal in magnitude. The misalignment angles $\delta_{x,y}$ in Fig. 6.4 include the misalignments within *H*-coils and with respect to *B*-coils. Additionally, the fundamental orthogonal components of both *B* and *H* are used in this analysis. These orthogonal components are:

$$\left.\begin{aligned} B_{xCW,CCW} &= B_{x1}\sin\omega t, \quad B_{yCW,CCW} = \pm B_{y1}\cos\omega t \\ H_{xCW,CCW} &= H_{x1}\sin(\omega t+\phi_x), \quad H_{yCW,CCW} = \pm H_{y1}\cos(\omega t+\phi_y) \end{aligned}\right\}, \qquad (66)$$

where $\phi_{x,y}$ is the loss angle between *B* and *H*. The plus and minus signs indicate CW and CCW directions respectively.

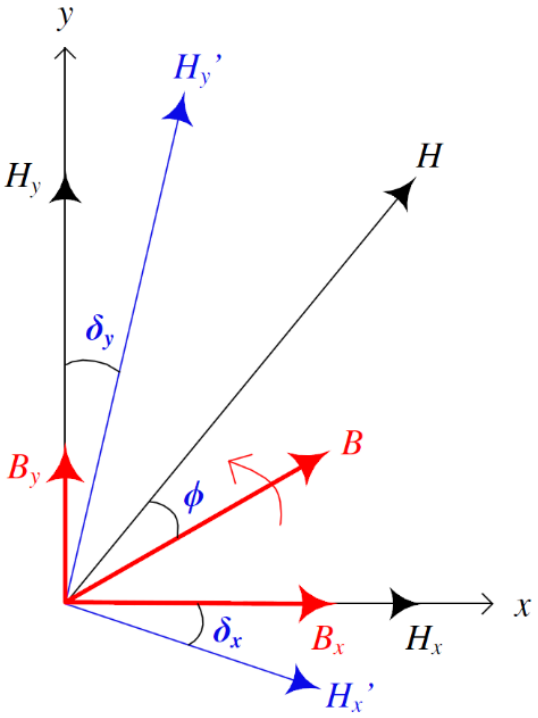

Fig. 6.4 Decomposition of *H* and *B* vectors, with angular misalignment in *H*-coils

Consider Fig. 6.4 where the *H*-coils are rotated CW with respect to the *B*-coils at arbitrary angles δ_x and δ_y. The measured components $H_x^{'}$ and $H_y^{'}$ are expressed as:

$$\left.\begin{aligned} H_x^{'} &= H_x \cos\delta_x - H_y \sin\delta_x \\ H_y^{'} &= H_x \sin\delta_y + H_y \cos\delta_y \end{aligned}\right\}. \tag{67}$$

Substituting the fundamental components into the measured components results in:

$$\left.\begin{aligned} H_{xCW,CCW}^{'} &= H_{x1} \sin(\omega t + \phi_x)\cos\delta_x \mp H_{y1} \cos(\omega t + \phi_y)\sin\delta_x \\ H_{yCW,CCW}^{'} &= H_{x1} \sin(\omega t + \phi_x)\sin\delta_y \pm H_{y1} \cos(\omega t + \phi_y)\cos\delta_y \end{aligned}\right\}. \tag{68}$$

The measured core loss in any direction is therefore:

$$P_{CW,CCW}^{'} = \frac{f}{\rho}\int_0^{1/f}\left(H_{xCW,CCW}^{'}\left(\frac{dB_{yCW,CCW}}{dt}\right) + H_{yCW,CCW}^{'}\left(\frac{dB_{yCW,CCW}}{dt}\right)\right)dt. \tag{69}$$

After some manipulations and substituting the derivatives of $B_{x,yCW,CCW}$ from equation (66) and of $H_{x,yCW,CCW}^{'}$ from equation (68), $P_{x,yCW,CCW}^{'}$ reduces to:

$$\left.\begin{aligned} P_{xCW,CCW}^{'} &= \frac{\pi f B_{x1}}{\rho}\left(H_{x1}\cos\delta_x \sin\phi_x \mp H_{y1}\sin\delta_x \cos\phi_y\right) \\ P_{yCW,CCW}^{'} &= \frac{\pi f B_{y1}}{\rho}\left(H_{y1}\cos\delta_y \sin\phi_y \mp H_{x1}\sin\delta_y \cos\phi_x\right) \end{aligned}\right\}. \tag{70}$$

This shows the inclusion of one direction component, i.e. $\delta_{x,y}$ into the other. Averaging the losses in the two directions eliminates the second term by angular error compensation as:

$$\left.\begin{aligned} \overline{P}_x^{'} &= \frac{P_{xCW}^{'} + P_{xCCW}^{'}}{2} = \frac{\pi f B_{x1} H_{x1}}{\rho}\cos\delta_x \sin\phi_x \\ \overline{P}_y^{'} &= \frac{P_{yCW}^{'} + P_{yCCW}^{'}}{2} = \frac{\pi f B_{y1} H_{y1}}{\rho}\cos\delta_y \sin\phi_y \end{aligned}\right\}. \tag{71}$$

As $\delta_{x,y}$ tends to unity, the average core loss approaches the ideal loss, and the difference between CW and CCW losses becomes negligible. As the sample saturates, $\phi_{x,y}$ tends to zero and the second terms of equations in (70) increase in magnitude, resulting in the divergence of CW-CCW core loss plots, as shown in Fig. 6.8 (a) and (b).

Averaging significantly reduces this error as shown in Fig. 6.9, but it cannot fully eliminate the effect of the angular error [39], [68], [105], since cos $\delta_{x,y}$ is part of equation (71). These residues are part of the absolute constant systematic errors that are difficult to correct.

The accurate estimation of $\delta_{x,y}$ requires complete saturation of the sample in the measurement region, such that the remaining core loss is attributed to misalignments. In this condition, the loss angle $\phi_{x,y}$ equates to zero, hence sin $\phi_{x,y} = 0$, and cos $\phi_{x,y} = 1$, which when substituted in equation (68), and letting $H_{x1} \approx H_{y1} \approx H_1$, the measured components become:

$$\left.\begin{aligned} H'_{xCW,CCW} &= H_1 \sin(\omega t \mp \delta_x) \\ H'_{yCW,CCW} &= H_1 \sin(\omega t \pm \delta_y) \end{aligned}\right\}, \tag{72}$$

which proves the shifting of the measured H waveforms [106]. For example, for CW measurements and + $\delta_{x,y}$, the measured H_x components in both CW and CCW become:

$$\left.\begin{aligned} H'_{xCW} &= H_1 \sin(\omega t - \delta_x) \\ H'_{xCCW} &= H_1 \sin(\omega t + \delta_x) \end{aligned}\right\}. \tag{73}$$

The H'_{xCW} waveform is shifted backwards, while the H'_{xCCW} is advanced in time. Therefore, any error that introduces a phase shift in the H waveforms, will result to CW-CCW core loss asymmetry.

The estimation of $\delta_{x,y}$ is prone to inaccuracies arising from the assumptions and misalignments within the B-coils. Therefore, averaging usually mitigates part of it, and the remaining components given in equation (71), forms part of the residues of the methodological errors that are difficult to correct. Therefore, the misalignment angles, $\delta_{x,y}$ were determined by iterating equation (70), until:

$$\overline{P}'_{x,y} = \frac{P'_{x,yCW} + P'_{x,yCCW}}{2} . \tag{74}$$

This absolute constant systematic angular error is approximated from the difference between the measured field $H'_{x,y}$ and the corrected field, $H_{x,y}$ as:

$$\varepsilon_{H_{\delta x,y}} = \frac{\Delta H_{\delta x,y}}{H_{pk}} = \frac{(H'_{x,y} - H_{x,y})}{H_{pk}}. \tag{75}$$

C. Integration noise error

Sources of integration noise error include data acquisition noise, and electromagnetic noise picked by sensor leads. It contributes to CW-CCW loss asymmetry [68], and affects *H* values more than the *B* values based on their transduction constants, i.e. K_H (~10^7) > K_B (~10^3). It is reduced by averaging of CW-CCW core losses, but increases with frequency and flux density, and poorly twisted sensor leads [68].

In the analysed measurement system, the integration noise error was 0.7 % of the core loss at 1.9 T, and 60 Hz (Fig. 6.5 (b) vis-á-vis Fig. 6.9). Hence, it was assumed negligible, though it is accounted for in the overall random error.

The error was analysed by replacing the *H*-coils with shorted sensor leads shown in Fig. 6.5 (a). Rotating core loss measurements were then done at 60 Hz, in both CW and CCW directions for two runs. In the second run, the setup was disassembled, and then reassembled. The initial position of the leads were also randomly changed. The average of the two runs with accompanying error bars, show an increase in noise with flux density in Fig. 6.5 (b).

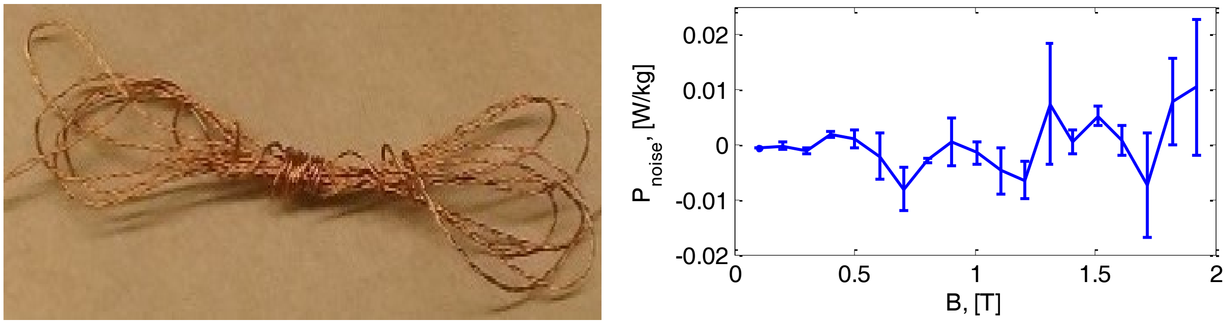

(a) Shorted sensor leads **(b) Measured noise**

Fig. 6.5 Measured noise under rotating fields, at 60 Hz

6.4.5 Flux Density Measurement Errors

The induced B-coil voltage is expressed as:

$$e_B(t) = N_B A_B \frac{dB}{dt} = K_B \frac{dB}{dt} . \tag{76}$$

Each B-coil has 10 turns, N_B wound through 1 mm diameter holes, 60 mm apart. It is difficult to correct the B-coil output by calibration, as is in the case of H-coils. The associated constant systematic error can only be corrected by estimating the enclosed sample area as $A_B \approx g_t l_B$. A set of sample thicknesses were measured and averaged to estimate g_t. The length of the B-coils, l_B is the distance between the B-holes, and is assumed constant. Therefore, elementary errors affecting B-coils are the thickness, airflux, angular misalignment, aspect-ratio and voltage distortion errors.

A. Thickness error

The thickness (g_t) of the M19G29 sample is gauge 29, which is 0.36 ± 0.05 mm thick. The tolerance is from an ASTM tolerance table [107], and the consideration of two decimal points of the an available Vernier calliper. The sample thickness is usually fixed, and only changes with a new sample. Hence, it is an absolute constant systematic error that affects the comparison of core losses of the same gauge material from different parent sheets, and in the estimation of the sample thickness in different laboratories. It is expressed in relative form as:

$$\varepsilon_{Bg_t} = \frac{\Delta g_t}{g_t} I_{B_{gt}} = \frac{\Delta g_t}{g_t} \frac{g_t}{B_{pk}} \frac{\partial B}{\partial g_t} , \tag{77}$$

where $\Delta g_t = 0.05$ mm, $g_t = 0.36$ mm and $I_{B_{gt}}$ is the influence coefficient of g_t with respect to B.

The thickness error will result in differences in core losses especially at high frequencies since eddy-current core losses are proportional to the square of the sample thickness. Its partial derivative can be approximated by using more than one sample, whose gauge variations fall within ± Δg_t, at the same frequency. In this case it is estimated as:

$$I_{B_{gt}} = \frac{\partial B}{\partial g_t} = \frac{\partial}{\partial g_t}\left(\frac{e_B(t)}{\omega N_B l_B g_t \cos(\omega t)} \right) = \frac{|e_B(t)|}{\omega N_B l_B g_t^2 \cos(\omega t)} . \tag{78}$$

It was reduced by averaging a set of thickness readings of the same sample.

B. Aspect-ratio error

The aspect-ratio, a ratio of the maximum to minimum radii of a B-locus, is derived from the amplitudes and phase-shifts of the B waveforms. In this study, the peaks and the phase shifts were controlled by the user, hence, it is a personnel error. In the case of waveform control, the error is dependent on the controller tolerance.

This error is composed of the control error of the flux density peaks and their phase, airflux error and misalignment error. In the ensuing analysis, the measured B_{px} phasor is assumed ideal in terms of magnitude and/or phase angle.

1) Control error of the flux density peaks and phase shift

The flux density peaks and phases are controlled within limits dependent on the accuracy of the personnel or feedback controller. Let the limits of the B peaks be ± $\varDelta B_{pr}$, while that of the phase shift difference be $\pm\varDelta\phi_r$. These limits were determined experimentally from rotating measurements, as the maximum deviations of 40 combined x and y flux density peaks, and 20 phase shift differences as 0.023 T and 0.622 °. The measured $B'_{px,py}$ phasors are therefore:

$$\left.\begin{aligned} B'_{px} &= \left(B_{px} \pm \varDelta B_{pr}\right) < 0^\circ \\ B'_{py} &= \left(B_{py} \pm \varDelta B_{pr}\right) < \left(90 \pm \varDelta\phi_r\right)^\circ \end{aligned}\right\}. \tag{79}$$

These errors are conditionally constant systematic error, whose relative forms are:

$$\left.\begin{aligned} \varepsilon_{B_{rx}} &= \frac{\varDelta B_{pr}}{B_{px}} \\ \varepsilon_{B_{ry}} &= \sqrt{\left(\frac{\varDelta B_{pr}}{B_{py}}\right)^2 + \left(\frac{\varDelta\phi_r}{\phi_r} I_{B_{\phi r}}\right)^2} \end{aligned}\right\}. \tag{80}$$

The influence coefficient, $I_{B_{\phi r}}$ is expressed as:

$$I_{B_{\phi r}} = \frac{\phi_r}{B_{py}} \cdot \frac{\partial B_y}{\partial \phi_r}, \tag{81}$$

and was approximated using measurements by varying ϕ_r in steps of 0.5 °, 1 °, 1.5 ° and 2 °.

2) *Airflux error*

B-coils enclose some leakage fields similar to *H*-coils, resulting to:

$$\left.\begin{aligned} B_{coil}(t) &= B_{airflux}(t) + B_{sample}(t) \\ B_{airflux}(t) &= \mu_0 H_{airflux}(t) \\ B_{sample}(t) &= \mu_0 M(t) \end{aligned}\right\}, \tag{82}$$

where M is the intrinsic magnetization of the material, and $H_{airflux}$ is the airflux leakage field, which is approximately equal to the applied field, H_a. In this case $\Delta\phi_{af} \approx 0$, since the enclosed air is close to the sample surface, i.e. it is one turn thick.

There is asymmetry in relation to the amount of air enclosed by the *B*-coils, as shown in Fig. 6.6, where the B_y-coil encloses more air than the B_x-coil. It results to an absolute constant systematic error, where the B_y–coil underestimates the flux density, as the peaks are controlled to be equal.

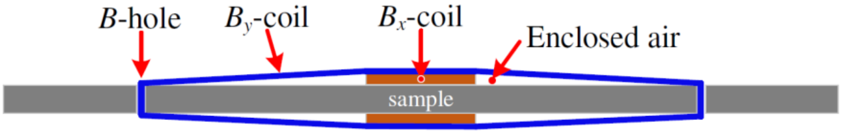

Fig. 6.6 *B*-coil arrangement showing the enclosed air by the B_y-coil (not drawn to scale)

The *B*-coil airflux error is only significant at very high flux densities where H_a is in the order of 10^4 A/m. The maximum $\Delta B_{airflux}$ was estimated at 19 kA/m as 0.024 T. The measured phasors in this case are:

$$\left.\begin{aligned} B'_{px} &= B_{px} < 0° \\ B'_{py} &= \left(B_{py} + \Delta B_{airflux}\right) < 90° \end{aligned}\right\}, \tag{83}$$

Hence, the relative error for the B_y-coil is:

$$\varepsilon_{Byaf} = \frac{\Delta B_{airflux}}{B_{py}} = \frac{\mu_0 H_a}{B_{py}} . \tag{84}$$

3) *Angular misalignment error*

Any angular misalignment in the winding of *B*-coils makes the *B*-locus to deviate from circular to elliptical. This will result to *H*-locus asymmetry; contributing to CW-CCW core loss asymmetry [68]. If the misalignment angle is known, it should be compensated before measurements [106]. In most cases, it is unknown, and difficult to estimate. Hence, it is mitigated by winding the *B*-coils through small diameter holes, and having more number of turns.

The misalignment angle δ_h caused by the positioning of *B*-coils via *B*-holes can be derived from Fig. 6.7 and the length of the *B*-coils, l_B as:

$$\delta_h = \tan^{-1}\left(\frac{d_h}{l_B}\right), \tag{85}$$

where the *B*-holes diameter is d_h. This shows that it can be minimized by decreasing d_h, increasing l_B, or increasing the number of turns to average the misalignments of individual turns. The latter may increase the airflux error.

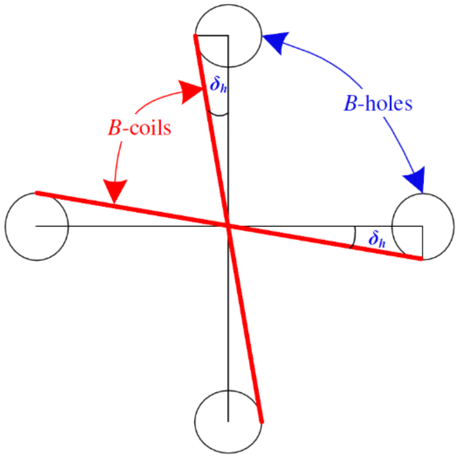

Fig. 6.7 Angular misalignment of *B*-coils caused by *B*-holes (not drawn to scale)

The maximum misalignment occurs for one turn *B*-coil. Hence, for a hole diameter of 1 mm, a *B*-coil length of 59 mm, δ_h is 0.97 °. From Fig. 6.7, the misalignment angle is twice δ_h. Therefore, the measured phasors in this case are:

$$\left.\begin{aligned} B'_{px} &= B_{px} < 0° \\ B'_{py} &= B_{py}\cos(2\delta_h) < (90 + 2\delta_h)° \end{aligned}\right\}, \tag{86}$$

by applying the misalignment to the B_y-coil. Similarly, the relative error for the B_y-coil is:

$$\varepsilon_{By\delta h} = \sqrt{\left(\frac{\Delta B_{py}}{B_{py}}\right)^2 + \left(\frac{2\delta_h}{\phi_r} I_{B\phi r}\right)^2} \,. \tag{87}$$

The influence coefficient $I_{B\phi r}$ is given in equation (81), and:

$$\Delta B_{py} = B'_{py}\left(1 - \frac{1}{\cos 2\delta_h}\right) . \tag{88}$$

This is also an absolute constant systematic error, arising from the winding of B-coils, as they are fixed on the sample.

4) Correlational additional aspect-ratio errors

The variation of one of the peaks, and/or phase angles causes variations in the B and H arguments, resulting to additional conditionally constant systematic errors. This is because of the correlation between the input arguments. These additional conditionally constant systematic errors were determined using two experiments.

In the first experiment, B_{py} was varied in step of 1, 2 and 3 %, and in the second experiment ϕ_r was varied in steps of 0.5 °, 1 °, 1.5 ° and 2 °. The additional errors were then determined as $\Delta H_{x,y}$ and $\Delta B_{x,y}$. A 2 % variation in B_{py} was used to determine the additional errors. Its associated errors are:

$$\left.\begin{aligned} \varepsilon_{Hx,ypk_{add}} &= \frac{\Delta H_{px,y}}{H_{px,y}} \\ \varepsilon_{Bx,ypk_{add}} &= \frac{\Delta B_{px,y}}{B_{px,y}} \end{aligned}\right\} . \tag{89}$$

For the ϕ_r, a variation of 1.5 ° was used in the computation of the additional errors. It only influenced the magnetic fields, whose relative errors are:

$$\varepsilon_{Hx,y\phi_{add}} = \frac{\Delta H_{px,y}}{H_{px,y}} . \tag{90}$$

C. *Voltage distortion error*

The distortion error of the induced voltages of the B-coils is analysed using the form-factor (F_F). The form-factor should be within 1.1107 ± 1 % according to ASTM standards [73]. In [56], the form-factor is modelled as part of the eddy-current core loss equation, while in [99] it is modelled as part of the overall uncertainty equation for pulsating core loss measurements.

This error is important in the comparison of core loses obtained using measurement systems with and without control of the B-coil voltages, to ensure measurement consistency.

It is an absolute constant systematic error that should be estimated using the uncontrolled and controlled B-coil voltages. In this study, the controlled voltages were approximated by the fundamental components. Hence, the error is estimated as:

$$\varepsilon_{e_B F_F} = \frac{\Delta F_{F_B}}{F_{F_B}} I_{e_B F_F} = \frac{(F_{F_B} - F_{F_{B1}})}{F_{F_B}} \frac{|e_B|}{B_{pk}} \frac{\partial B}{\partial e_B}, \tag{91}$$

where F_{F_B} and $F_{F_{B1}}$ are the form-factors for the uncontrolled and fundamental B-coil voltages. $I_{e_B F_F}$ is the influence coefficient of e_B with respect to B.

6.4.6 Overall Random Error

Ten ($n = 10$) repeated rotating core loss measurements were used to evaluate the overall random error. CW and CCW measurements were done in each run in the range of 0.1 T to 1.9 T, at 60 Hz. The H-coils and the sample were disassembled, and then reassembled after each run. The sensor lead locations were also changed. This was done to excite the sources of random errors. The tests were done within 5 º K (5 º C) from room temperature.

It was also possible to analyse the effectiveness of averaging in the reduction of CW-CCW core loss asymmetry. For the first five runs, CW measurements preceded CCW, and for the rest, the order was reversed. The first five runs are continuous plots, while the rest are dotted as shown in Fig. 6.8 (a) and (b), for CW and CCW core losses, respectively.

There is scatter in core losses at high flux densities in both CW and CCW directions, as shown in Fig. 6.8 (a) and (b). In addition, changing the preceding direction after the first five runs does not influence the plots in either direction. This is because the sample was demagnetized from a flux density that was higher than 1.9 T, before each CW and CCW set of measurements. This eliminated any remnant magnetization.

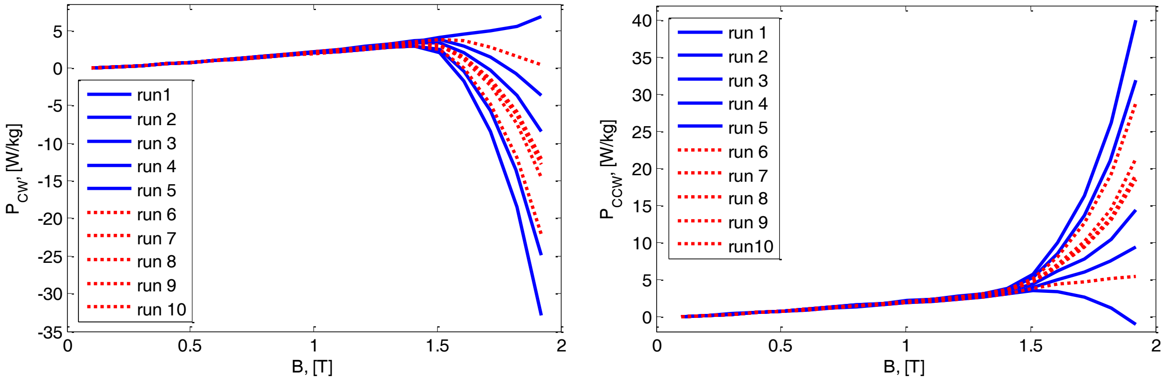

(a) CW core loss measurements **(b) CCW core loss measurements**

Fig. 6.8 CW and CCW rotating core losses for 10 runs, at 60 Hz

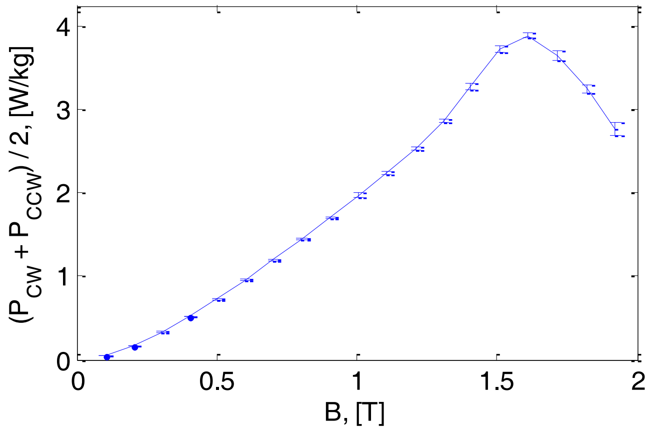

Fig. 6.9 Averaging of CW and CCW core losses with error bars for 10 runs, at 60 Hz

Averaging significantly reduced the divergence in the CW-CCW core loss plots, as shown by the standard deviation error bars in Fig. 6.9. It proves that this asymmetry is mainly caused by *H*-coil angular misalignments, as described previously in section 6.4.4 B.

6.5 Measurement Error Results Analysis

After quantitatively estimating the elementary errors, the *B* and *H* argument errors were then determined. The total uncertainty was then estimated at each *B* measurement point.

6.5.1 Absolute Constant Systematic Errors

Core losses are predisposed to absolute constant systematic errors, especially in the measurement of *H*. That of *H* (L_H) is about 78 % of the total absolute error (L_{ac}), as shown in Fig.

6.10, while that of the measurement of B (L_B) is about 25 %. These errors were determined from $B_{x,y}$ and $H_{x,y}$, which were weighted by their respective influence coefficients as:

$$\left.\begin{aligned} L_B &= I_{B_x}\varepsilon_{B_x} + I_{B_y}\varepsilon_{B_y} \\ L_H &= I_{H_x}\varepsilon_{H_x} + I_{H_y}\varepsilon_{H_y} \end{aligned}\right\}. \qquad (92)$$

The thickness error ($\approx L_B$) contributed significantly to the absolute B error, while the airflux, L_{Haf} dominated the absolute H error, as seen in Fig. 6.10.

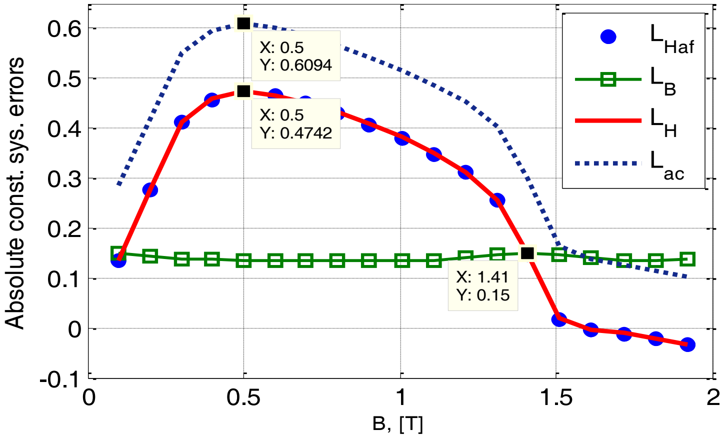

Fig. 6.10 Absolute constant systematic errors for *B* and *H* arguments, at 60 Hz

The estimation of the airflux error was prone to errors arising from their measurements, i.e., they should be estimated as close as possible to the sample surface (within less than 5 mm). In addition, they were determined from pulsating measurements, which required extrapolation for higher rotating magnetic fields. Its influence coefficient was also based on fundamental components that resulted in their overestimation beyond the knee point.

The thickness error was corrected by averaging over a number of sample thicknesses. It is difficult to correct the airflux leakage field error because it depends on the location of H-coils, relative to the sample surface, frequency and flux density. Ideally, double H-coils can be used to extrapolate the sample field and correct for the angular phase-shift. Alternatively, a different measurement method such as thermometric or torquemetric can be used to correct the measurements for the entire flux density range, at a given frequency.

6.5.2 Conditionally Constant Systematic Errors

Additional errors caused by the correlation in B and H significantly influenced conditionally constant systematic errors. The additional errors mainly affected the H arguments ($\upsilon_{H(add)}$) more than the B arguments ($\upsilon_{B(add)}$), as shown in Fig. 6.11 (a), where υ_{add} is their total. The rapid increase in the H error, $\upsilon_{H(add)}$ (hence υ_{add}) after 1.0 T was caused by the increase in H_y as a result of a 2 % increase in B_y. The sudden drop of the $\upsilon_{H(add)}$ (hence υ_{add}) curve after 1.4 T was caused by the increase in H with B, which decreases the relative error. That is, the error become insignificant in comparison to the very high H fields towards 2 T.

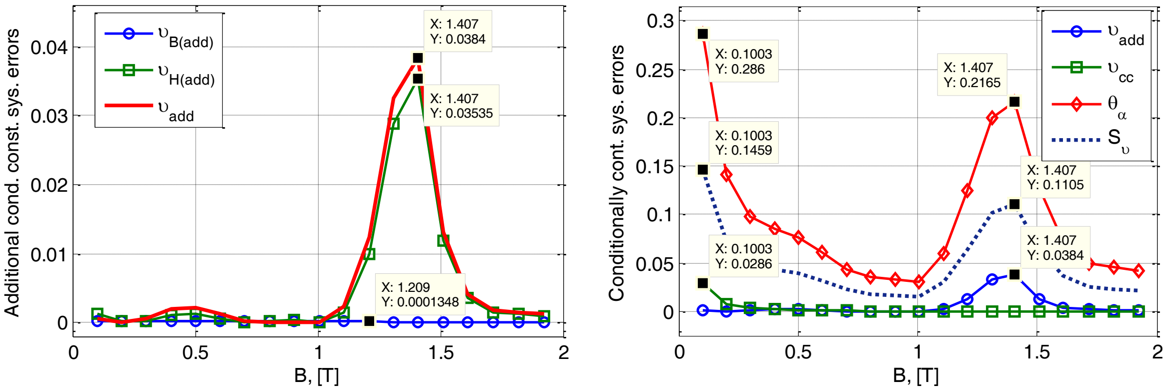

(a) Additional conditional constant errors **(b) Conditionally constant errors**

Fig. 6.11 Conditionally constant systematic errors for *B* and *H* arguments, at 60 Hz

It is important to note that a 2 % variation in B_{py}, at 1.8 T and 1.9 T, resulted in a ΔH of 880 A/m and 1,222 A/m, respectively. The highest ΔH caused by the phase-shift variations was not as significant (42 A/m).

The conditionally constant limit, θ_α, were then determined using equation (48), and its profile has signatures from the additional, υ_{add} and the rest of the conditionally constant errors, υ_{cc} as seen in Fig. 6.11 (b). The high value of θ_α at 0.1 T was due to the control error of the flux density peaks and their phase shifts. The same error limits ($\pm \Delta B_{pr} = 0.023$ T and $\pm \Delta\phi_r = 0.622$ º) were used for the entire flux density range. Hence, at low flux densities, the associated error was higher (23 % at 0.1 T), as compared to high flux densities (1.2 % at 1.9 T). The standard deviation, S_υ which is an indicator of conditionally systematic errors, was then determined from equation (50), and has a similar profile as θ_α as shown in Fig. 6.11 (b).

6.5.3 Overall Random Error

The overall Random error of the core losses at each flux density *B* measurement point was derived as standard deviation of the ten repeated measurements, using equation (52). The random error increases with flux density loading as shown in Fig. 6.12. Additionally, Fig. 6.9 showed that averaging of CW and CCW core losses significantly reduced systematic errors associated with *H*-coil angular misalignment. This will also reduce some random errors, such as integration noise by averaging.

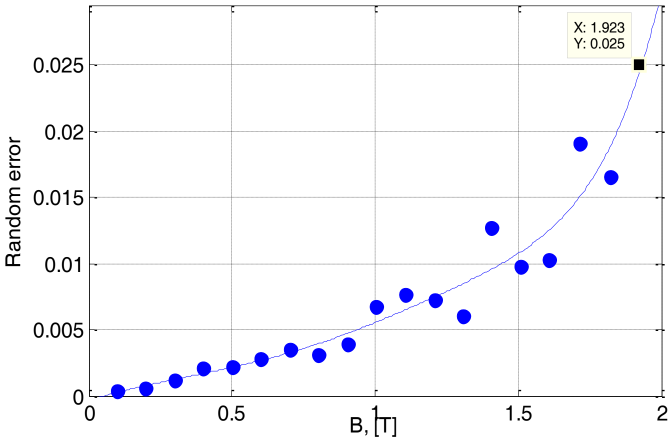

Fig. 6.12 Overall random error, at 60 Hz

6.5.4 Total Uncertainty

It is now possible to express the total uncertainty in terms of absolute, conditionally and random errors. Equation (54) gives the combined uncertainty (u_c) of conditionally systematic and random errors, which are all random in nature. The sum of the combined uncertainty and the absolute systematic errors, gives the total uncertainty, u_t as given in equation (55). The total uncertainty is significantly biased by the absolute constant systematic error, L_{ac} that is 89 % of u_t as shown in Fig. 6.13.

The absolute systematic error largely depends on the *H*-coil airflux leakage error (78 % of L_{ac}, and 70% of u_t), and the thickness error (25 % of L_{ac}, and 22 % of u_t). Subtracting the absolute systematic errors from the total uncertainty, results to the combined uncertainty, u_c of the conditionally systematic and random errors shown in Fig. 6.13.

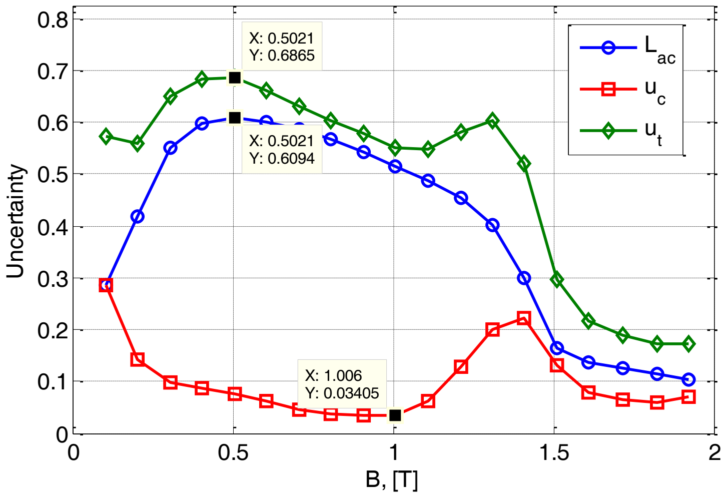

Fig. 6.13 Absolute, combined and total uncertainty for rotational core losses, at 60 Hz

This shows the importance of correcting absolute systematic errors since they will result in the overestimation of core losses, for a fieldmetric measurement system. After corrections, the uncertainty is largely dependent on conditionally systematic and random errors. Moreover, the peaks of the combined uncertainty (u_c) curve at around 1.4 T, are attributed to the correlational additional control errors of the aspect-ratio. Hence, the control limits for ± ΔB_{pr} and ± $\Delta \phi_r$, should be less than 2 % and 1 % (< 1 °), respectively. Within these limits, and correcting for absolute constant systematic errors, the total uncertainty falls within 3 to 10 %, in the entire flux density range.

6.6 Conclusion

The total uncertainty of core losses was determined from *B* and *H* elementary errors, for a flux density range of 0.1 T to 1.9 T, at 60 Hz. The uncertainty results showed that core losses are predisposed to absolute constant systematic errors, especially in the measurement of *H*. Sampling frequencies less than 21.6 kHz at 60 Hz should be avoided for flux densities beyond the knee point. They result in the intertwining of *B-H* loops, underestimation of core losses, and contribute to CW-CCW core loss asymmetry.

Averaging of CW and CCW core losses significantly reduced the rotating core loss asymmetry, which is mainly caused by *H*-coil angular misalignments. In addition, the errors due to tolerances in aspect-ratio control were sensitive to *B* peak variations, as opposed to phase shift variations. A 2 % variation in B_y at 1.9 T, resulted in a ΔH_y of 1.2 kA/m, while a 1.5 ° variations in the 90 ° phase shift between the *B* components was not as significant (42 A/m).

The *H*-coil airflux leakage field error dominated the total uncertainty by about 70 %, although it was prone to estimation errors.

Correcting absolute constant systematic errors, and operating within less than 2 % and less than 1 % (< 1 º) tolerances for the control of the *B* peaks and the phase shift, will reduce the total uncertainty to less than 10 %, in the entire flux density range.

A summary of the findings of this study are presented next.

Chapter 7. Conclusion and Future Work

The study presented the need for a solution to the inadequacy of pulsating core loss measurements, and the limited range of 1.4 T at 60 Hz of the benchmark Halbach tester, for high flux density rotational core loss measurements. The proposed tester met the main objective of extending the flux density measurement range to 2 T at 60 Hz, and maintaining the frequency range of 60 Hz to 1 kHz. The contributions of this thesis to the design of high flux density rotational core loss magnetizers are:

i. Long effective axial length (deep yoke) of greater than 60 mm for compact magnetizers (sample diameter $\leq$ 100 mm, and airgap $\leq$ 2 mm), to minimize the variation and improve the homogeneity of the flux density in the measurement area, increase the sample magnetic loading and lower the yoke losses.

ii. B-coil lengths should be greater than 40 mm in core loss measurement of unannealed samples, to minimize the effect of local degradation caused by holes used to locate B-coils, and other inhomogeneities. Hence, unannealed square samples whose B-coil lengths are about 10 – 20 mm are predisposed to this error.

iii. The effectiveness of shielding depends on the distance of the shield from the sample surface, and magnetic loading of the sample. Hence, shielding at 9 - 10 mm is recommended for flux densities below 1.0 T, and 18 - 20 mm, for flux densities above 1.0 T. Shielding at less than 9 mm should be avoided as it increases the magnetic field z-component because of the interaction of the sample and the shields.

iv. The airflux leakage field close to the sample surface influences the shape, magnitude and phase of the measured magnetic field, and is one of the most dominant sources of measurement error. Hence, double H-coils are suggested to minimize it, and reduce the total uncertainty to less than 10 %.

The application of the proposed setup was validated by core loss measurements under sinusoidal pulsating, elliptical and rotating magnetizations at 60 Hz, 400 Hz and 1 kHz. Moreover, elliptical non-sinusoidal excitation at 60 Hz, were demonstrated using the flux density loci of a hydro synchronous generator. This is in addition to rotational ($r > 0$) to pulsating ($r = 0$) core loss ratios, which showed significant increase in the core loss magnitudes with increasing frequency. Hence, the setup is important in the generation of both sinusoidal and non-sinusoidal rotational core loss data in the analysis of the increased rating of large machines, and in the design of cored electric machines.

Core loss data is invaluable in the accurate estimation of the temperature distribution in a machine. This is particularly important in increasing the rating of vintage MW rated hydro generators, and other large machines on the implications of increasing the load. This increase in capacity is cost effective at a higher efficiency and reliability, at a fraction (10 to 12.5 % [108]) of new hydro stations and/or machines. These machines were oversized based on standards and tools available at the time. They were designed based on pulsating core loss data and higher loss core materials. Hence, their rating can be increased by better characterization of core losses using non-sinusoidal rotational core loss data that reflects machine operation, and retrofitting them with lower loss core material with better insulation for the same footprint.

In general, the use of non-sinusoidal rotational core loss data is more accurate in the prediction of hotspots, and in thermal circuit design. Increasing machine rating requires the consideration of the temperature distribution of the machine, hence the need for more accurate core loss data. The predisposition of large machines to very high magnetic and mechanical forces results in vibrations, which translates to rubbing of the stator laminations. If the lamination insulation is poor, based on the predicted highest temperature of the hotspots, then it can break down resulting in short-circuiting of the laminations, and eventual failure of the machine. Large MW rated machines are not only expensive, but their downtime is costly to utilities, mining and other energy intensive processes, such as in cement production. Therefore, the non-sinusoidal rotational core loss data generated using the proposed setup will allow more precise prediction of hotspots temperature, than traditional sinusoidal pulsating data.

Operating at higher frequencies can result in a reduction of the machine size. Hence, the aerospace industry and other industries with operating frequencies greater than 200 Hz will benefit greatly from rotational core loss data. At these frequencies, core losses become one of the dominant losses, and pulsating estimation significantly underestimates the core loss with significant rotational flux. This can result in underestimation of local heating, which can reduce the service life of the machine. Moreover, the use of wide gap switching devices (SiC and GaN), which are not yet main stream, will allow even higher operating frequencies, that can be limited by the thermal circuit. Therefore, the accurate estimation and distribution of core losses with the consideration of other losses, is important in the mapping of hot spots, sizing and analysis of the thermal circuit. The setup can also be used to characterize high frequency core materials of thinner gauges (≤ 0.36 mm), which are of lower loss than conventional silicon steels with no cooling up to 1 kHz. This frequency range can be extended with minimal modifications.

The following specific conclusions are drawn from the presented design methodology of high flux density rotational core loss magnetizers:

i. The flux density variation and its non-uniform distribution in the sample were minimized by sinusoidally distributing the windings of a round tester, and equalization of the reluctance with magnetization direction. The proposed sinusoidally wound round tester had the least flux density variation, of the highest magnitude in comparison to a square tester, Halbach tester and conventionally wound machine stator based tester.

ii. A longer stack length (deep yoke) was shown to minimize the variation and non-uniformity of the flux density. It also increases the sample magnetic loading, and lowers that of the yoke; minimizing yoke effects.

iii. Center-threaded B-coils were more accurate than wrapped or side-threaded B-coils, although B-holes increase non-uniformity and magnetic field noise. The effect of magnetic degradation owing to B-holes was minimized by averaging over longer B-coil lengths greater than 40 mm, and having an allowance in the placement of H-coils.

iv. The airflux leakage field above the sample was shown to influence the shape, magnitude and phase of the measured field. The latter reduced the loss angle between B and H; reducing the measured core loss. Its impact on the measured magnetic field increased with a reduction of the magnetizer diametrical size. Furthermore, the airflux leakage field error dominated the total uncertainty by about 70 %. Hence the need to extrapolate the measured field on the sample surface by using double or multi H-coils.

v. A diametrically large magnetizer is the only way to significantly reduce the magnetic field z-component (H_z), at the expense of the attainable flux density. Shielding at 18 mm to 22.5 mm was recommended, although for a measurement range of less than 1.0 T, shielding at 9 mm to 10 mm was as effective as a large magnetizer. Beyond 1.0 T, using a shielding distance of less than 10 mm increased H_z because of magnetic interaction between the shields and the sample.

vi. The proposed numerical methodology was validated experimentally. The magnetizer achieved very high flux densities in the range of 2 T at 60 Hz for both G29 (0.35 mm) and G24 (0.65 mm) samples. For G29 samples, flux density loadings of 1.8 T and 1.6 T were measured at 400 Hz and 1 kHz, respectively. For the thicker G24 samples, the range reduced to 1.7 T and 1.4 T, 400 Hz and 1 kHz, respectively. The magnetizer also reproduced numerical non-sinusoidal waveforms for flux densities less than or equal to 1.0 T, without any waveform control.

vii. Low sampling frequencies, such as 21.6 kHz at 60 Hz should be avoided at flux densities beyond the knee point. They result in the intertwining of *B*-*H* loops, underestimation of core losses and contribute to CW-CCW core loss asymmetry.

viii. Fieldmetric core loss measurements are predisposed to systematic errors, especially in the measurement of the magnetic field. Correcting for these errors, and operating within less than 2 % and 1 % (< 1 º) tolerances by controlling the waveforms, will reduce the total uncertainty to less than 10 % in the entire flux density range.

The following recommendations are necessary to improve the performance of the developed rotational core loss measurement test bench:

i. The implementation of double *H*-coils to improve the accuracy in the measurement of the magnetic field.

ii. Development of a waveform controller and signal acquisition system that will allow better control of the aspect-ratio, form-factor and non-sinusoidal flux densities, without introducing measurement errors as a result of sampling. This will reduce measurement errors, and improve their estimation.

iii. More accurate alignment of *B* and *H* sensors relative to each other, and with the sample, to improve the accuracy of measuring pulsating core losses, since they cannot be corrected by averaging.

iv. More accurate estimation of the airflux measurement error to reduce the bias in the estimation of uncertainty.

v. Provision for cooling the sample to allow for higher frequency measurements beyond 1 kHz.

These measures will improve the confidence of the measured core losses for any aspect-ratio, allowing for further research in rotational core loss modelling and generation of core loss data under both sinusoidal and non-sinusoidal excitations. This will allow more accurate estimation of core losses compared to the current methods and models utilising pulsating data.

References

[1] G. McCoy, T. Litman and J. Douglass, "Energy-Efficient Motor Selection Handbook," Pullman, 1993.

[2] M. M. Znidarich, "Hydro Generator Stator Cores Part 1 - Construction Features and Core Losses," in *2008 Australasian Universities Power Engineering Conference (AUPEC '08)*.

[3] G. Seggewiss, J. Dai and M. Fanslow, "Synchronous Motors on Grinding Mills: The Different Excitation Types and Resulting Performance Characteristics with VFD Control for New or Retrofit Installations," *IEEE Industry Applications Magazine,* vol. 21, pp. 60-67, Nov-Dec 2015.

[4] J. Gieras, "New Applications of Synchronous Generators," *Przeglad Elektrotechniczny (Electrical Review),* no. 09a/2012, pp. 150-157.

[5] M. A. Plonus, Applied Electromagnetics, McGraw-Hill, Inc., 1978.

[6] Y. Zhang, "Expermental, Theoretical and Numerical Invesitgation of Core Losses in Laminated Magnetic Materials," PhD Thesis, Clarkson University, Potsdam, 2008.

[7] G. Bertotti, Hysteresis in Magnetism, Academic Press, 1998.

[8] J. Akiror, A. Merkhouf, C. Hudon and P. Pillay, "Consideration of Design and Operation on Rotational Flux Density Distribution in Hydrogenerator Stators," *IEEE Trans. Energy Conver.,* 2015.

[9] J. W. Macki, P. Nistri and P. Zecca, "Mathematical Models for Hysteresis," *Soc. Indu. Appl. Mathe.,* vol. 35, no. 1, pp. 94-123, 1993.

[10] H. Hauser, "Energetic Model of Ferromagnetic Hysteresis: Isotropic Magnetization," *J. Appl. Phys.,* vol. 96, no. 5, pp. 2753-2767, 2004.

[11] L. Dupré and J. Melkebeek, "Electromagnetic hysteresis modelling: from material science to finite element analysis of devices," *International Compumag Society Newsletter,* pp. 4-15, 2003.

[12] R. Szewczyk, "Application of Jiles-Atherton Model for Modelling Magnetization Characteristics of Textured Electrical Steel Magnetized in Easy or Hard Axis," *Progress in Automation Robotics and Measuring Techniques,* pp. 293-302, 2015.

[13] K.-J. Ko, S.-K. Jang, J.-Y. Choi, S.-H. Lee and Y.-B. Lee, "A core loss calculation based on magnetic field analysis considering the time harmonics of high-speed permanent magnet machine according to driving method," in *IEEE International Conference on Electrical Machines and Systems (ICEMS)*, 2010.

[14] L. Ma, M. Sanada, S. Morimoto and Y. Takeda, "Prediction of iron loss in rotating machines with rotational loss included," *IEEE Transactions on Magnetics,* vol. 39, no. 4, pp. 2036-2041, July 2003.

[15] H. Domeki, Y. Ishihara, C. Kaido, Y. Kawase, S. Kitamura, T. Shimomura, N. Takahashi, T. Yamada and K. Yamazaki, "Investigation of benchmark model for estimating iron loss in rotating machine," *IEEE Transactions on Magnetics,* vol. 40, no. 2, pp. 794-797, March 2004.

[16] J. Zhu and V. Ramsden, "Improved formulations for rotational core losses in rotating electrical machines," *IEEE Transactions on Magnetics,* vol. 34, no. 4, pp. 2234-2242, July 1998.

[17] C. Appino, O. de la Barriere, C. Beatrice, F. Fiorillo and C. Ragusa, "Rotational Magnetic Losses in Nonoriented Fe–Si and Fe–Co Laminations up to the kilohertz Range," *IEEE Trans. Magn.,* vol. 50, no. 11, pp. 1-4, 2014.

[18] VACUUMSCHMELZE GMBH & CO. KG , "Soft Magentic Cobalt-Iron-Alloys," 2001.

[19] Aperam Alloys Imphy, "Nickel Iron and Cobalt Iron Cold Rolled Strips," 2013.

[20] H. Pfutzner et al, "Rotational Magnetization in Transformer Cores - A Review," *IEEE Trans. Magn.,* vol. 47, no. 11, pp. 4523-4533, November 2011.

[21] C. Kittel, "Physical Theory of Ferromagnetic Domains," *Reviews of Modern Physics,* vol. 21, no. 4, pp. 541-583, October 1949.

[22] A. Hubert and R. Schafer, Magnetic Domains: The Analysis of Magnetic Microstructures, 3rd Printing ed., Springer, 2008.

[23] F. Baily, "The Hysteresis of Iron and Steel in a Rotating Magnetic Field," *Phil. Trans. of the R. Soc. Lond.,* vol. 187, pp. 715-746, January 1896.

[24] B. Zawilski, D. Maillard, O. Geoffroy and D. Dufeu, "Rotating Sample Magnetometer for Precise, Real Time Differential Measurements," *Rev. Sci. Intrum.,* vol. 77, 2006.

[25] R. Gimaev, Y. Spichkin, M. Plyashkevich and A. Tishin, "Rotating-Sample Magnetometer for Measuring Crystal Field Parameters," *Solid State Phenomena,* vol. 190, pp. 175-178, June 2012.

[26] J. Rigue, D. Chrischon, A. H de Andrade and M. Carara, "A Torque Magnetometer for Thin Films Applications," *J. Magn. Magn. Mater,* vol. 324, no. 8, pp. 1561-1564, April 2012.

[27] J. Sievert, H. Ahlers, M. Enokizono, S. Kauke, L. Rahf and J. Xu, "The Measurement of Rotational Power Loss in Electrical Sheet Steel Using a Vertical Yoke System," *J. Magn. Magn. Mater.,* vol. 112, pp. 91-94, 1992.

[28] C. Ragusa, S. Zurek, C. Appino and A. Moses, "An Intercomparison of Rotational Loss Measurements in Non-Oriented Fe-Si Alloys," *J. Magn. Magn. Mater.,* vol. 320, no. 20, pp. e623-e626, October 2004.

[29] H. Hamzehbahmani, A. Moses and F. Anayi, "Opportunities and Precautions in Measurements of Power Loss in Electrical Steel Laminations Using Initial Rate of Rise of Temperature Method," *IEEE Trans. Magn.,* vol. 49, no. 3, March 2013.

[30] K. Atallah and D. Howe, "Calculation of the Rotational Power Loss in Electrical Steel Laminations from the Measured H and B," *IEEE Trans. on Magn.,* vol. 29, no. 6, pp. 3547-3549, November 1993.

[31] S. Zurek and T. Meydan, "Errors in the power loss measured in CW and ACW rotational magnetisation. Part 1: Mathematical study," *IEE Proc.-Sci. Meas. Technol.,* vol. 153, no. 4, pp. 147-151, July 2006.

[32] C. Appino, F. Fiorillo and C. Ragusa, "One-Dimension/Two-Dimension Loss Measurements up to High Inductions," *J. Appl. Phys.,* vol. 105, no. 07E718, 2009.

[33] M. Enokizono and H. Matsuo, "A Measurement System for Two-Dimensional DC Biased Properties of Magnetic Materials," *J. Magn. Magn. Mater.,* Vols. 254-255, pp. 39-42, January 2003.

[34] A. Basak and A. Moses, "Influence of Stress on Rotational Loss in Silicon Iron," *Proc. IEE,* vol. 125, no. 2, pp. 165-168, February 1978.

[35] T. Sasaki, M. Imamura, S. Takada and Y. Suzuki, "Measurement of Rotational Power Losses in Silicon-Iron Sheets Using Wattmeter Method," *IEEE Trans. Magn.,* vol. 21, no. 5, pp. 1918-1920, September 1985.

[36] S. Yanase, M. Uchiyama, S. Ishikawa and Y. Okazaki, "AC Magnetic Properties of Electrical Steel Sheet Under DC-Biased Magnetization," *Przeglad Elektrotechniczny (Electrical Review),* vol. R. 87, no. 9b, pp. 52-56, 2011.

[37] M. Jesenik, V. Gorican, M. Trlep, A. Hamler and B. Stumberger, "Eddy Current Effects in the Sample of 2D RRSST and in the Sample of 2D SRSST," in *11th Intern. Symp. on Electromag. Fields in Elect. Eng. (ISEF 2003)*, Slovenia, 2003.

[38] Y. Li, Y. Qingxin, J. G. Zhu, Z. Zhigang, L. Xiaojing and Z. Changgeng, "Design and Analysis of a Novel 3-D Magnetization Structure for Laminated Silicon Steel," *IEEE Trans. Magn.,* vol. 50, no. 2, pp. 389-392, 2014.

[39] K. Mori, S. Yanase, Y. Okazaki and S. Hashi, "2-D Magnetic Rotational Loss of Electrical Steel at High Magnetic Flux Density," *IEEE Tran. Magn.,* vol. 41, no. 10, pp. 3310-3312, October 2005.

[40] Y. Maeda, S. Urata, Y. Kano, T. Arakawa, S. Yanase, Y. Okazaki and S. Watanabe, "Examination of Measurement Apparatus for 2D Magnetic Properties," *Elect. Comm. Japan,* vol. 96, no. 2, pp. 57-64, 2013.

[41] J. Zhu, J. Zhong, Z. Lin and J. Sievert, "Measurement of Magnetic Properties Under 3-D Magnetic Excitations," *IEEE Trans. Magn.,* vol. 39, no. 5, pp. 3429-3431, September 2003.

[42] H. Shokrollahi and K. Janghorban, "Soft magnetic composite materials (SMCs)," *Mater. Proc. Tech.,* vol. 189, no. 1, pp. 1-12, 2007.

[43] V. Gorican, A. Hamler, B. Hribernik, M. Jesenik and M. Trlep, "2-D Measurements of Magnetic Properties Using a Round RSST," in *1&2-D Magn. Meas. & Test.*, Bad Gastein, 2000.

[44] A. Hasenzagl, B. Weiser and H. Pfutzner, "Novel 3-Phase Excited Single Sheet Tester for Rotational Magnetization," *J. Magn. Magn. Mater.,* vol. 160, pp. 180-182, 1996.

[45] N. Alatawneh and P. Pillay, "Design of a Novel Test Fixture to Measure Rotational Core losses in Machine Laminations," *IEEE Trans. Indu. Applicat.,* vol. 48, no. 5, pp. 1467-1477, 2012.

[46] O. de la Barriere, C. Appino, F. Fiorillo, C. Ragusa, M. Lecrivain, L. Rocchino, H. B. Ahmed, M. Gabsi, F. Mazaleyrat and M. LoBue, "Extended frequency analysis of magnetic losses under rotating induction in soft magnetic composites," *J. Appl. Physics,* vol. 111, no. 07e325, 2012.

[47] J. Zhu, "Numerical Modelling of Magnetic Materials for Computer Aided Design of Electromagnetic Devices," PhD Thesis, University of Technology , Sydney, 1994.

[48] A. Jander, C. Smith and R. Schneider, "Magnetoresistive Sensors for Nondestructive Evaluation," in *International Symp. Conf. on Nondestructive Evaluation for Health Monitoring and Diaganostics*, 2005.

[49] B. Fryskowski, "Experimental Evaluation of Magnetic Anisotropy in Electrical Steel Sheets," *J. Magn. Magn. Mater.,* vol. 320, pp. 515-522, 2008.

[50] H. Mason, "Basic Introduction to the Use of Magentoresisitve Sensors," Application Note 37, ZETEX Semiconductor, 2003.

[51] A.-. E. Abdallh and L. Dupre, "A Rogowski-Chattock Coil for Local Magnetic Field Measurements: Sources of Error," *Meas. Sci. Technol.,* vol. 21, no. 10, October 2010.

[52] S. Tumanski, "Induction Coil Sensors - A Review," *Meas. Sci. Technol.,* vol. 18, pp. R31-R46, 2007.

[53] Y. Li, Q. Yang, Y. Liu, Z. Zhao, C. Zhang and D. Li, "A Novel Combined B−H Sensing Coil in Three-Dimensional Magnetic Properties Testing System," *IEEE trans. Applied Supercond.,* vol. 24, no. 3, 2014.

[54] F. Fiorillo and A. Rietto, "Extended Induction Range Analysis of Rotational Losses in Soft Magnetic Materials," *IEEE Trans. Magn.,* vol. 24, no. 2, pp. 1960-1962, March 1988.

[55] A. M. Gumaidh, T. Meydan and A. Moses, "Characterisation of Magnetic Materials Under Two-dimensional Excitation," in *IEEE Digest of International Magnetics Conference 1993 (INTERMAG 93)*, 1993.

[56] J. Sievert et al, "Intercomparison of Measurements of Magnetic Losses in Electrical Sheet Steel Under Rotating Flux Conditions," Director General XII Science, Research and Development, EC Brussels, 1995.

[57] A. Moses, "Possible Future Trends and Research Challenges Realted to 1 & 2D Magentic Properties of Soft Magentic Matarials," *Przeglad Elecktrotechniczny (Electrical Review),* vol. R.87, no. 9b, pp. 11-16, 2011.

[58] G. Krismanic, "Recent Developments and Trends in Measurements of Two-Dimensional Magentic Properties," *J. Elect. Eng.,* vol. 55, no. 10, pp. 45-48, 2004.

[59] JSOL Corporation, "Techical Support & User's Manual Solver for JMAG Designer Version 12," 2013.

[60] H. Soltner and P. Blumer, "Dipolar Halbach Magnet Stacks Made from Identically Shaped Permanent Magnets for Magnetic Resonance," *Concepts Magn. Reson. Part A,* vol. 36A, no. 4, pp. 211-222, 2010.

[61] V. Gorican, A. Hamler, M. Jesenik, B. Stumberger and M. Trlep, "Unrealiable Determination of Vector B in 2-D SST," *J. Magn. Magn. Mater.,* Vols. 254-255, pp. 130-132, January 2003.

[62] J. Zhong and J. Zhu, "Improved Measurement With 2-D Rotating Fluxes Considering the Effect of Internal Field," *IEEE Trans. Magn.,* vol. 41, no. 10, pp. 3709-3711, 2005.

[63] Asahi Kasei Microdevices, "EQ-730L data sheet," [Online]. Available: http://www.akm.com/akm/en/file/datasheet/EQ-730L.pdf. [Accessed 19 Dec 2014].

[64] J. E. Parks, "Helmholtz Coils-Uniform Magnetic Fields," Department of Phyics and Astronomy, The University of Tennessee, Knoxville, 2013.

[65] M. Enokizono and J. Sievert, "Numerical Analysis of Accuracy of rotational Magnetic Loss Measurement Apparatus," *IEEE Trans. Magn. Japan,* vol. 5, no. 9, pp. 742-748, September 1990.

[66] J. Wanjiku and P. Pillay, "Design Considerations of 2-D Magnetizers for High Flux Density Measurements," *IEEE Trans. Indu. Applicat.,* vol. 51, no. 5, pp. 3629-3638, 2015.

[67] Y. Li, Q. Yang, J. G. Zhu and Y. Guo, "Magnetic Properties Measurement of Soft Magnetic Composite Materials Over Wide Range of Excitation Frequency," *IEEE Trans. Indu. Applicat.,* vol. 48, no. 1, pp. 88-97, 2012.

[68] S. Zurek and T. Meydan, "Errors in the Power Loss Measured in CW and ACW Rotational Magnetisation. Part 2: Physical Phenomena," *IEE Proc.-Sci. Meas. Technol.,* vol. 153, no. 4, pp. 152-157, 2006.

[69] M. Dimitre, M. Rauch, M. D. Wulf and J. Melkebeek, "Accurate Field Strength Measurement in Rotational Single Sheet Testers," *J. Magn. Magn. Mater.,* pp. 673-676, 2000.

[70] M. Jesenik, V. Gorican, M. Trlep, A. Hamler and B. Stumberger, "Field Homogeneity in a Two-phase Round Rotational Single Sheet Tester With One and Both Side Sheilds," *J. Magn. Magn. Mater.,* Vols. 254-255, pp. 247-249, 2003.

[71] V. Gorican, A. Hamler, M. Jesenik, B. Stumberger and M. Trlep, "Interaction of z component of magnetic field between two samples of GO material in the round rotational single sheet tester," *J. Magn. Magn. Mater.,* vol. 304, pp. 558-560, 2006.

[72] ASTM Committee on Magnetic Properties, "Standard Practice for Sampling and Procurement Testing of Magnetic Materials," ASTM International, 2001.

[73] ASTM Committee on Magnetic Properties, "Standard Test Method for Alternating-Current Magnetic Properties of Toroidal Core Specimens Using the Voltmeter-Ammeter-Wattmeter Method," ASTM International, 1999.

[74] S. G. Rabinovich, Measurement Errors and Uncertainties: Theory and Practice, Springer, 2005.

[75] A. Ferrero and S. Salicone, "Modeling and Processing Measurement Uncertainty Within the Theory of Evidence: Mathematics of Random-Fuzzy Variables," *IEEE trans. Instrumentation and Measurement,* vol. 56, no. 3, pp. 704-716, 2007.

[76] N. Ridler, B. Lee, J. Martens and K. Wong, "Measurement Uncertainty, Traceability, and the GUM," *IEEE Microwave Magazine,* vol. 8, no. 4, pp. 44-53, 2007.

[77] A. Giordani and L. Mari, "Measurement, models, and uncertainty," *IEEE trans. Instrumentation and Measurement,* vol. 61, no. 8, pp. 2144-2152, 2012.

[78] R. Furness, "The cost of measurement uncertainty," in *IEEE Petroleum and Chemical Industry Conference Europe (PCIC Europe)*, 2008.

[79] G. Beges, J. Drnovsek, I. Pusnik and J. Bojkovski, "Calculation and proper presentation of the measurement uncertainty in testing," in *19th IEEE Instrumentation and Measurement Technology Conference (IMTC)*, 2002.

[80] J. Wirandi, W. Kulesza and A. Lauber, "Modeling of Industrial Measurement Systems Considering the Human Factor," in *IEEE Instrumentation and Measurement Technology Conference (IMTC)*, 2006.

[81] B. Lu, W. Cao and T. Habetler, "Error Analysis of Motor-Efficiency Estimation and Measurement," in *IEEE Power Electronics Specialists Conference*, 2007.

[82] Joint Committee for Guides in Metrology, "Evaluation of measurement data — Guide to the expression of uncertainty in measurement," JCGM, 2008.

[83] Joint Committee for Guides in Metrology, "Evaluation of measurement data - Supplement 1 to the GUM - Propagation of distributions using a Monte Carlo method," JCGM, 2008.

[84] A. Ferrero and S. Salicone, "A Comparative Analysis of the Statistical and Random-Fuzzy Approaches in the Expression of Uncertainty in Measurement," *IEEE trans. Intrumentation and Measurement,* vol. 54, no. 4, pp. 1475-1481, 2005.

[85] T. Lovett, F. Ponci and A. Monti, "A polynomial chaos approach to measurement uncertainty," *IEEE trans. Instrumentation and Measurement,* vol. 55, no. 3, pp. 729-736, 2006.

[86] D. Lampasi, F. Nicola and L. Podesta, "Generalized lambda distribution for the expression of measurement uncertainty," *IEEE trans. Instrumentation and Measurement,* vol. 55, no. 4, pp. 1281-1287, 2006.

[87] L. Angrisani, R. Moriello and M. D'Apuzzo, "New proposal for uncertainty evaluation in indirect measurements," *IEEE trans. Instrumentation and Measurement,* vol. 55, no. 4, pp. 1059-1064, 2006.

[88] P. Memmolo, L. Moriello, R. Schiano and P. Pinto, "On the Use of Numeric Integration for Uncertainty Evaluation in Indirect Measurements," in *IEEE International Workshop on Advanced Methods for Uncertainty Estimation in Measurement*, 2007.

[89] P. Hack, T. Caten and C. Schwengber, "Measurement uncertainty: Literature review and research trends," *IEEE trans. Instrumentation and Measurement ,* vol. 61, no. 8, pp. 2116-2124, 2012.

[90] G. Cipriani, D. La Cascia, R. Miceli and C. Spataro, "Uncertainty management in the measurements for the electric power quality analysis," in *IEEE International Energy Conference (ENERGYCON)*, 2014.

[91] A. Ferrero and S. Salicone, "The Random-Fuzzy Variables: A New Approach to the Expression of Uncertainty in Measurement," *IEEE trans. Instrumentation and Measurement,* vol. 53, no. 5, pp. 1370-1377, 2004.

[92] S. Sona and M. Havlikova, "Comparison of GUM and Monte Carlo method for evaluation measurement uncertainty of indirect measurements," in *14th IEEE International Carpathian Control Conference,* 2013.

[93] S. Nuccio and C. Spataro, "A Monte Carlo method for the auto-evaluation of the uncertainties in the analog-to-digital conversion-based measurements," *The international journal for computation and mathematics in electrical and electronic engineering,* vol. 23, no. 1, pp. 148-158, 2004.

[94] K. Barbé, L. Gonzales Fuentes, O. Olarte and L. Lauwers, "Monte-Carlo parameter uncertainty analysis under dynamical and operational measurement conditions," in *IEEE International Instrumentation and Measurement Technology Conference (I2MTC)*, 2014.

[95] B. Hall, "Calculations of measurement uncertainty in complex-valued quantities involving'uncertainty in the uncertainty'," in *IEEE ARFTG Microwave Measurements Conference*, 2004.

[96] A. Ferrero, M. Prioli and S. Salicone, "Processing dependent systematic contributions to measurement uncertainty," *IEEE trans. Instrumentation and Measurement,* vol. 62, no. 4, pp. 720-731, 2013.

[97] A. Smith, A. Monti and F. Ponci, "Uncertainty and worst-case analysis in electrical measurements using polynomial chaos theory," *IEEE trans. Instrumentation and Measurement,* vol. 58, no. 1, pp. 58-67, 2009.

[98] J. Kohler and L. Gradin, "Test laboratory position for expression of uncertainty and confidence in measurement," in *IEEE International Symposium on Electromagnetic Compatibility*, 2003.

[99] H. Ahlers and J. Ludke, "The uncertainties of magnetic properties measurements of electrical sheet steel," *J. Magn. Magn. Mater.,* vol. 215, pp. 711-713, 2000.

[100] M. S. Pierce and et al, "Disorder-induced magnetic memory: Experiments and theories," *Physical Review,* vol. B, no. 75, 2007.

[101] Y. Ishihara, A. Isozumi, T. Todaka and T. Nakata, "Comparison of two averaging methods for improving the measurement accuracy of power loss," *J. Magn. Magn. Mater.,* vol. 215, pp. 696-699, 2000.

[102] dSPACE GmbH, "DS1103 PPC Controller Board," in *dSPACE Catalog 2015*, pp. 334-338.

[103] S. A. More, "ADC Performance Parameters," Texas Instruments , 2013.

[104] N. Alatawneh and P. Pillay, "Design of a Novel Test Fixture to Measure Rotational Core losses in Machine Laminations," *IEEE Trans. on Industrial Applications,* vol. 48, no. 5, 2012.

[105] V. Gorican, M. Jesenik, A. Hamler, B. Stumberger and M. Trlep, "Measurement of 2-D Magnetic Properties of Grain Oriented Silicon Steel Sheet Using RRSST," in *11th International Symposium on Electromagnetic Fields in Electrical Engineering (ISEF 2003)*, Maribor, Slovenia, September, 2003.

[106] Y. Maeda, H. Shimoji, T. Todaka and M. Enokizono, "Study of the Counterclockwise/Clockwise (CCW/CW) Rotational Losses Measured with a Two-Dimensional Vector Magnetic Property Mesurement System," *IEEJ Trans. Elect. Elect. Eng.,* vol. 3, pp. 222-228, 2008.

[107] Coyote Steel & Co., "Resources: ASTM/AISI Thickness Tolerance Ranges," [Online]. Available: http://www.coyotesteel.com/resources_toleranceranges.shtml. [Accessed 29 July 2015].

[108] M. M. Znidarich, "Upgrading and Uprating of Hydro Generators: An Australian Perspective," *Australian Journal of Electrical and Electronics Engineering,* vol. 10, no. 1, pp. 75-84, 2015.